# A DESIGN PARADIGM FOR DC GENERATION SYSTEM

by

**Bo Zhang**

**A Dissertation**

*Submitted to the Faculty of Purdue University*

*In Partial Fulfillment of the Requirements for the degree of*

**Doctor of Philosophy**


School of Electrical & Computer Engineering

West Lafayette, Indiana

August 2019

# THE PURDUE UNIVERSITY GRADUATE SCHOOL
# STATEMENT OF COMMITTEE APPROVAL

Dr. Scott D. Sudhoff, Chair
School of Electrical & Computer Engineering
Dr. Dionysios C. Aliprantis
School of Electrical & Computer Engineering
Dr. Oleg Wasynczuk
School of Electrical & Computer Engineering
Dr. Steven D. Pekarek
School of Electrical & Computer Engineering

**Approved by:**

Dr. Dimitrios Peroulis

Head of the Graduate Program

*I dedicate this work to my parents, Zhandong Zhang and Yanling Li. Thank you for always supporting me.*

# ACKNOWLEDGMENTS

I would like to thank Professor Sudhoff for his guidance and support during my Ph.D. I could not have finished it without his advice and knowledge. I would also like to thank Professor Aliprantis, Professor Pekarek, and Professor Wasynczuk for being my advisory committee.

I would like to thank Rob Swanson. Without him, the system prototype would not have been built. I am grateful to my colleagues for their assistance.

I would like to thank Sandia National Laboratories for partially funding this work through Contract Agreement 1701331.

Finally, I would like to thank Mian Yang for being there with me all the time.

# TABLE OF CONTENTS

# LIST OF TABLES

# LIST OF FIGURES

# ABSTRACT

Author: Zhang, Bo. PhD
Institution: Purdue University
Degree Received: August 2019
Title: A Design Paradigm for DC Generation System.
Committee Chair: Scott Sudhoff

The design of a dc generation system is posed as a multi-objective optimization problem which simultaneously designs the generator and the power converter. The proposed design methodology captures the interaction between various system component models and utilizes the system steady state analysis, stability analysis, and disturbance rejection analysis. System mass and power loss are considered as the optimization metrics and minimized. The methodology is demonstrated through the design of a notional dc generation system which contains a Permanent Magnet Synchronous Machine (PMSM), passive rectifier, and a dc-dc converter. To this end, a high fidelity PMSM model, passive rectifier model, semiconductor model and passive component model are developed. The output of optimization is a set of designs forming a Pareto-optimal front. Based on the requirements and the application, a design can be chosen from this set of designs. The methodology is applied to SiC based dc generation system and Si based dc generation system to quantify the advantage of Wide Bandgap (WBG) devices. A prototype SiC based dc generation system is constructed and tested at steady state. Finally a thermal equivalent circuit (TEC) based PMSM thermal model is included in the design paradigm to quantify the impact of the PMSM's thermal performance to the system design.

# 1. INTRODUCTION

## 1.1 Introduction

Compared to ac generation systems, dc generation systems have several advantages which make them appealing for a variety of applications. For example, dc generation systems don't need synchronization of different generators which make it possible to operate each generator/prime-mover at the most beneficial speed. DC generation system applications include shipboard power generation systems [1] [2], more electric aircraft power generation systems [3], and some wind farms [4]. In this work, a new dc generation system design methodology is set forth.

A dc generation system includes a generator and a power converter. The generator converts mechanical energy to electricity. The power converter is used to convert ac voltage to dc voltage and to regulate the dc bus voltage level. Usually, the two components are designed separately and then integrated. This approach cannot guarantee an optimal design from the system point of view. It is necessary to formulate a design approach which designs the generator and power converter simultaneously. To achieve this, a dc generation system topology is chosen. Then the generator model and converter model are developed and various system specifications are imposed as the design constraints. A case study is then carried out to demonstrate the proposed design approach.

## 1.2 DC Generation System

Different electric machines can be used in dc generation system. In [1], a Wound Rotor Synchronous Machine (WRSM) based dc generation system and a Permanent Magnet Synchronous Machine (PMSM) based dc generation system are prototyped and compared. The PMSM based system has higher efficiency and higher power density since the rotor is self-

magnetized [1]. In [3], an induction machine is applied to a hybrid ac/dc aircraft generation system because of its fault tolerance performance and robustness. In [5], a hybrid machine containing a field winding and PMs is considered to leverage the advantages of the WRSM's field winding control and the PMSM's efficiency.

For the power converters, a rectifier is necessary to convert generator ac voltage to dc voltage. For rectifier options, a passive rectifier has the advantages of robustness and cost. For PMSM based generation systems, it decouples the generator from the dc bus control. A dc-dc converter is used to control the dc bus voltage. For WRSM based generation systems, the dc bus voltage can be controlled by adjusting the field excitation voltage. Semi-active rectifiers such as thyristor rectifiers are available at almost all power levels. The drawback of the thyristor rectifier is its limited control bandwidth and the need for reactive power to support the required firing angle. The reactive power will lead to increased generator mass which lowers the system's power density. The active rectifier can regulate the dc bus voltage more quickly and have lower harmonic currents compared to the passive rectifier, and thus a smaller filter can be applied. A drawback of the active rectifier is its robustness since there are six active switches and rotor position feedback is typically required.

Among the dc generation system topologies, a PMSM feeding passive rectifier and dc-dc converter system is of particular interest due to its simplicity. In this arrangement, the dc bus voltage is regulated by the dc-dc converter. In [6], such system is used for wind power generation. During a change of wind speed, the dc-dc converter is used to hold the dc bus voltage constant. A drawback of such system pointed out in [6] is that the passive rectifier will cause harmonics in the generator current which lead to torque ripple and lower efficiency.

Herein, a notional dc generation system is selected to investigate the dc generation system design methodology. The system topology is shown in Fig. 1.1. A PMSM is selected as the generator which is operating at a fixed speed. A three-phase passive rectifier is used because of its robustness. The output voltage is regulated by a two quadrant dc-dc buck converter. The dc-dc converter consists of an input inductor $L_{in}$, output inductor $L_{out}$, input capacitor $C_{in}$, output capacitors $C_{outp}$, $C_{oute}$, transistors $T_1$, $T_2$ and diodes $D_1$, $D_2$. Permanent Magnet Inductors (PMIs) [7] are used for input inductor $L_{in}$ and output inductor $L_{out}$ to reduce size. Since $L_{in}$ sees a low frequency current ripple, silicon steel is used as the core material to reduce mass. Since $L_{out}$ sees the switching frequency, ferrite is used as the core material to reduce high-frequency loss. Polypropylene capacitors are used for $C_{in}$ and $C_{outp}$ because of their bandwidth and lifetime. The additional output electrolytic capacitor $C_{oute}$ is used because of its high capacitance over mass ratio. It is mainly used to stabilize the dc bus voltage during transient disturbances.

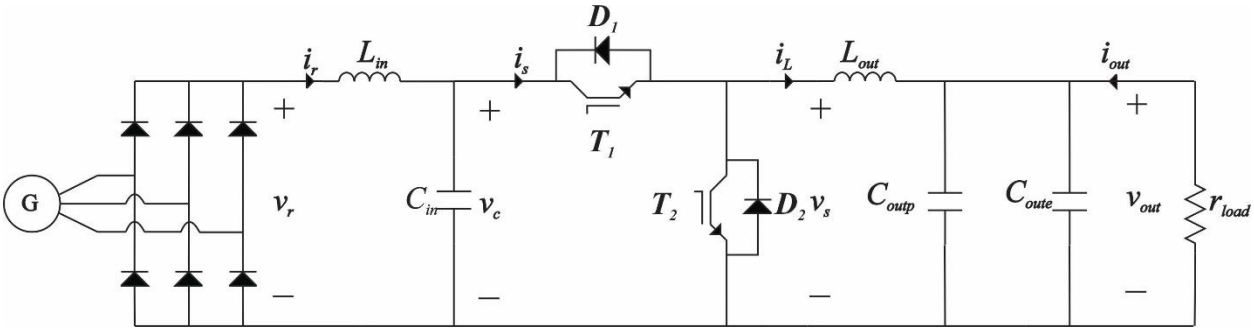


Fig. 1.1 DC Generation System Topology

## 1.3 DC Generation System Design Methods

In this section, dc generation system design methods appearing in the literatures are reviewed. In [1], a dc generation system is designed empirically and the generator design is validated using a 2D time-stepping Finite Element Analysis (FEA). This approach is informal and not likely to achieve a design on the boundary of achievable performance. To achieve high efficiency and high power density, a multi-objective optimization based design approach is beneficial. A reliable optimization requires a high fidelity system model and an appropriate optimization algorithm. Population based algorithms are effective since they are less likely to be trapped by a local extrema and can be used with a large design space. Among the population based algorithms, Genetic Algorithm (GA) and Particle Swarm Optimization (PSO) are commonly used. In [8], a Hybrid-Excited Flux-Switching (HEFS) machine feeding a passive rectifier generation system is developed for aircraft application. A static finite element model is developed and used with PSO to maximize the output power and efficiency under the remnant voltage constraint and weight constraint. In [5], a hybrid machine feeding a passive rectifier system is proposed. An analytical model is developed and used with GA based optimization engine to minimize the system mass and loss. In [9], a wound rotor synchronous machine with a passive rectifier system is considered. Compared to [5], a dynamic magnetic equivalent circuit (MEC) model is used with a GA optimization engine. Since the generation system considered in [5] and [9] has a field winding, a passive rectifier is utilized, the dc output voltage is regulated by adjusting the field excitation. Compared to other works, [5] and [9] include the passive rectifier loss and dc filter loss and mass in the system optimization.

Through all the aforementioned works, designers focused on the generator design and neglected the converter design. The dc bus voltage is fixed at several known operating points and

the system control strategy and disturbance rejection capability are neglected. There are numerous dc generation control strategies found in the literature but they usually only focus on the control strategy for an already designed dc generation system. For example, in [10], an adaptive state feedback control is proposed to stabilize the dc bus in a Medium Voltage dc (MVdc) application from the generation side instead of the load side. In [11], an active fault-current foldback control is implemented in a thyristor rectifier based dc generation system to protect the MVdc system from short-circuit fault which can help eliminate the need for a dc circuit breaker.

When considering the system control strategy, the system stability and disturbance rejection capability, which are crucial to dc generation systems, must be evaluated. Time domain simulation is used widely to evaluate the system's disturbance rejection capability [12] [13]. Compared to time domain analysis, frequency domain impedance analysis is computationally efficient and thus is an attractive approach for disturbance rejection analysis in optimization based design. One example using impedance analysis to design a control strategy is found in [14]. A Maximum Power Point Tracker (MPPT) controller is proposed for a photovoltaic (PV) system which contains PV panel, Cuk converter, and motor load. The system dynamic model is established and the linearized system model is used to establish a fitness function for a GA in order to establish the parameters of the MPPT controller.

In [15], a dc distribution system design problem is formulated as a multi-objective optimization problem to minimize the system mass and loss. The controller gains and the passive components are designed at the same time. One of the limitations of [15] is that the switching frequency is fixed at the highest allowed frequency of the semiconductors which make the semiconductor loss irrelevant to the system design thus the semiconductor loss and the heatsink design is not included. Further [15] only specifies the system design in terms of passive element

values. Another limitation of [15] is that the time domain simulation is performed to ensure each design's disturbance rejection capability. The method is very computationally expensive. In this work, a detailed design of a generation system is considered including the generator, passive components, and control parameters. The method will include the steady-state and transient aspect of performance in a computationally expedient way.

## 1.4 Objectives and Design Considerations

As pointed out in Section 1.3, a design methodology that integrates the generator design and power converter design is required to obtain an optimal system design. The proposed design methodology in this work includes three aspects: the generator design, converter passive components selection, and converter switching frequency selection. The generator design includes the PMSM geometry selection, the magnetic field analysis and calculation of the lumped parameter model. For the converter design, since the converter topology is fixed as in Fig 1.1, the converter parameters that need to be selected are the passive components and the transistor switching frequency. The passive components selection is based on the voltage or current ripple specifications and the disturbance rejection requirement. The switching frequency selection will impact the system loss performance, the passive components size, and the system disturbance rejection capability since the controller gains are tied to the switching frequency.

There are various design requirements for a dc generation system design. The generator design has to meet a series of geometry constraints and magnetic field constraints. For the converter design, besides the ripple requirements, the thermal requirement have to be met to ensure the converter's lifetime. The system has to be stable and has a strong disturbance rejection capability. With all the requirements satisfied, the system's loss and mass need to be minimized.

A typical design process to satisfy all the requirements is to design a generator and converter separately and ensure they satisfy their own design requirements. The two components are grouped as a generation system at a later stage. Then a control strategy is developed based on the system disturbance rejection requirement and modified based on the disturbance rejection test results. Due to the highly coupled nature between the generator and the converter, this process may be iterative and time consuming and cannot guarantee an optimal system design.

In this work, the generator design and converter design are integrated into a multi-objective optimization problem. The candidate solution to the optimization problem contains the generator geometry, passive components parameters, and the switching frequency. All the requirements mentioned above are cast as constraints and evaluated in a fitness function to determine if a candidate solution satisfy the design requirements. If a candidate solution satisfies all the requirements, the optimization metrics such as system mass and system loss can be evaluated. If not, the fitness function will evaluate how close the candidate comes to satisfy the requirements.

Numerous design considerations are addended in this work. With regard to the generator, the use of a passive rectifier will introduce large harmonic components to the generator phase current. A new PMSM design model is developed in this work to account for the temporal current harmonics and spatial winding harmonics. With respect to the converter, to accommodate the optimization based design algorithm, a frequency domain disturbance rejection analysis is developed to guarantee the system disturbance rejection capability. To further reduce the computational time and more importantly, reduce the design space, a metamodel based permanent magnet inductor (PMI) model is applied in this work. On the converter output stage, to facilitate high semiconductor switching frequencies, polypropylene capacitors are used as filter capacitors considering its bandwidth and lifetime. However, since electrolytic capacitors have higher

capacitance mass ratio, they are placed in parallel with the polypropylene capacitor and used to stabilize dc bus voltage during low-frequency disturbances.

## 1.5 Impact of Wide Bandgap Devices

Another trend of the power conversion system design is the application of Wide Bandgap (WBG) devices. According to [16], WBG denotes any semiconductors with bandgaps significantly larger than one electron volt (eV). The larger bandgap property of WBG semiconductors provide a higher critical breakdown field compared to silicon (Si) semiconductors, thus a thinner drift layer can be used, yielding a lower on-resistance to reduce conduction loss. The higher critical breakdown field can also contribute to a smaller die size thus reducing the junction capacitance and resulting in lower switching loss. The low switching loss allows WBG semiconductors switching at a much higher frequency than Si devices. This will reduce the required filter inductor and capacitor size. Another advantage of WBG devices over Si devices is thermal performance. WBG devices have higher thermal conductivity and higher junction temperature rating which allows devices to utilize a smaller heatsink. In summary, WBG devices have high breakdown voltage rating, extremely low switching loss, and high junction temperature rating compared to traditional Si devices, all of which can facilitate increased power density. These properties are well explored in the literature. In [17], a 6 kV, 10 kW, 40 kHz isolated dc-dc converter was designed based on a 15-kV SiC MOSFET module to demonstrate WBG semiconductors' high voltage blocking capability. In [18], a 4.5 kW, 1.2 MHz LLC resonant converter was designed based on silicon carbide (SiC) MOSFETs to demonstrate the fast switching capability of WBG semiconductors. In [19], a 10 kW three-phase ac-dc-ac converter was designed with the SiC JFETs'

junction temperature operated at 250 ℃ to demonstrate WBG devices' excellent thermal performance.

Other WBG materials such as Gallium Nitride (GaN) and ultra-wide bandgap (UWBG) materials such as Aluminum Gallium Nitride (AlGaN) are explored in [20]. Compared to Si's critical breakdown field (0.3 MV/cm), SiC's critical breakdown field is 2.2-2.5 MV/cm, GaN's critical breakdown field is 4 MV/cm, and AlGaN's critical breakdown field can reach to 16.6MV/cm. Although the GaN material and AlGaN material have excellent critical breakdown field property which means much higher blocking voltage can be achieved, due to the wafer fabrication difficulty, the GaN devices and AlGaN devices are still under development. In this work, SiC devices are selected to represent the WBG's devices since SiC MOSFETs and SiC Schottky barrier diodes are commercially available.

To better demonstrate the advantage of WBG device over Si devices, several Size, Weight, and Power (SWaP) comparisons between SiC based power converter system and Si based power converter system have been reported in the literature. In [21], two 10-kVA three-phase inverters were built using Si Insulated-Gate Bipolar Transistors (IGBTs) and SiC Junction Field-Effect Transistors (JFETs), respectively. The inverter using SiC JFETs achieved a 67% reduction in the inductor and capacitor volume and a 92% reduction in the heatsink volume. In [22], two 100 W dc-dc flyback converters, one based on GaN High Electron Mobility Transistors (HEMTs), and one based on Si MOSFETs are compared. The GaN based flyback converter achieved a 1.04 $W/cm^3$ power density whereas the Si based flyback converter achieved a 0.54 $W/cm^3$ power density.

In this work, the impact to dc generation systems SWaP due to the application of WBG semiconductors is quantified using the proposed dc generation system design methodology.

## 1.6 Contribution

A summary of the main contributions of this work is given below:

(i) A dc generation system design methodology which integrate generator design, converter design, and control design, into one multi-objective optimization problem is proposed to minimize the system mass and system loss. The optimization results are presented as a Pareto-optimal front of mass versus loss.

(ii) A high-fidelity PMSM model is established which takes the spatial winding harmonics and temporal current harmonics into consideration.

(iii) Average-value modeling of the dc generation system is used to enable the utilization of frequency domain analysis to guarantee the system stability and disturbance rejection capability.

(iv) The WBG (SiC) devices' loss performance are characterized and are integrated into the generation system design to quantify WBG's advantage over Si in system power density and system efficiency perspectives.

## 1.7 Organization

This dissertation is organized as follows. Chapter 1 has introduced a dc generation system topology and given a brief introduction to the proposed design methodology. A literature review of dc generation system design methods and WBG semiconductor research has also been set forth. Chapter 2 introduces the semiconductor loss model and thermal model. The PMI metamodels and capacitor models are developed in Chapter 3. The PMSM, passive rectifier, input inductor, and input capacitor formulate an uncontrolled generation subsystem. The subsystem models are

developed in Chapter 4. In Chapter 5, the system steady state analysis, control strategy, stability, and disturbance rejection analysis are introduced. Based on the developed models in Chapter 1 – Chapter 5, the dc generation system design problem is cast as a multi-objective optimization problem in Chapter 6. A case study is performed in Chapter 6 to demonstrate the proposed design methodology. The impact of SiC semiconductors to the dc generation system is quantified in the last part of Chapter 6. A SiC based dc generation system design is built and tested. The comparison between the measurement and prediction from analytical model is performed in Chapter 7. In Chapter 8, a thermal equivalent circuit (TEC) based PMSM thermal model is included in the design paradigm to quantify the impact of PMSM's thermal performance to the system design. Conclusions and directions of future work are discussed in Chapter 9.

# 2. SEMICONDUCTOR MODELS

A switch mode power converter is used in the notional dc generation system. Power loss produced by semiconductor switches will contribute to system loss. To accurately predict the system performance, it is necessary to establish the semiconductor loss model. The semiconductor loss has two components which are conduction loss and switching loss. When the semiconductor conducts, there is a small voltage drop applied to the semiconductor which will cause the conduction loss. When the semiconductor switches, both the voltage and the current are nonzero which will cause the switching loss. In this chapter, a generic semiconductor loss model is established and the loss model is applied to the notional system to achieve the Si semiconductors loss and SiC semiconductors loss. The power loss produced by semiconductor switches will contribute to device heating. A heat sink is required to dissipate the heat. Semiconductor thermal models are developed in the last section to calculate heat sink mass.

## 2.1 Semiconductor Loss Model

The transistor exhibits conduction loss and switching loss. When the transistor is conducting, it can be modeled as an on-state resistor [23] so the power loss can be modeled as $i_{t,cd}^2 R_{on}$, where $i_{t,cd}$ is the conducting current and $R_{on}$ is the on-state resistance. However it is demonstrated in [7] that following polynomial function better represents the instantaneous conduction loss

$$p_{t,cd}\left(i_{t,cd}\right) = \alpha_{t,cd} i_{t,cd} + \beta_{t,cd} (i_{t,cd} / i_b)^{\gamma_{t,cd}} \tag{2.1}$$

where $\alpha_{t,cd}$, $\beta_{t,cd}$, and $\gamma_{t,cd}$ are model parameters. The base current $i_b$ =1 A is used to make the units consistent.

When the transistor turns on, the conducting current will increase while the transistor voltage drop holds at the off-state voltage ($v_{t,off}$). For a MOSFET, the transistor voltage drop is the drain-to-source voltage. For an IGBT, the transistor voltage drop is the collector-to-emitter voltage. After the conducting current reaches the on-state current ($i_{t,on}$), the voltage drop starts decreasing until it reaches to the on-state voltage ($v_{t,on}$). When the transistor turns off, the voltage drop will increase while the conducting current stays at $i_{t,off}$. After the voltage drop reaches $v_{t,on}$, the conducting current start decreasing to zero [23]. The following behavioral polynomial function is used to model the energy loss associated with transistor switching [7]

$$E_{t,y}(i_{t,sw}, v_t) = (\alpha_{t,y} {i_{t,sw}}^2 + \beta_{t,y} i_{t,sw} + \gamma_{t,y}) v_t / v_{t,b} \tag{2.2}$$

where $v_{t,b}$ is the base voltage, $\alpha_{t,y}$, $\beta_{t,y}$ and $\gamma_{t,y}$ are model parameters, and the subscript y is either “on” or “off” to designate turn on or turn off energy loss, respectively.

The diode loss model contains the conduction loss and the reverse recovery loss. The diode instantaneous conduction loss is modeled as [7]

$$p_{d,cd}(i_f) = \alpha_{d,cd} i_f + \beta_{d,cd} (i_f / i_b)^{\gamma_{d,cd}} \tag{2.3}$$

where the $i_f$ is the forward conduction current and $\alpha_{d,cd}$, $\beta_{d,cd}$ and $\gamma_{d,cd}$ are model parameters.

The diode switching loss is dominated by the reverse recovery loss. When the diode turns off, the diode conducting current will drop to a negative value to sweep out the excessive carriers stored in the drift region which causes the reverse recovery loss. The diode reverse recovery loss is established in [7] which can be approximated using the sequence

$$I_{rr}(i_{off}) = \alpha_{irr} i_{off} + \beta_{irr} (i_{off}/i_b)^{\gamma_{irr}} \tag{2.4}$$

$$t_{rr}(i_{off}) = \alpha_{trr} i_{off} + \beta_{trr} (i_{off}/i_b)^{\gamma_{trr}} \tag{2.5}$$

$$P_{d,rr} = v_R^2 I_{rr}(i_{off}) t_{rr}(i_{off}) / (4 v_{d,b} T_{sw}) \tag{2.6}$$

where $I_{rr}$ is the peak reverse recovery current, $i_{off}$ is the forward conducting current at turn-off event, $t_{rr}$ is the reverse recovery time, $v_R$ is the reverse biased voltage, $v_{d,b}$ is the diode base voltage, and $\alpha_{trr}$, $\beta_{trr}$, $\gamma_{trr}$, $\alpha_{irr}$, $\beta_{irr}$ and $\gamma_{irr}$ are model parameters.

## 2.2 Semiconductor Loss in Notional System

In this section, the model established in Section 2.1 is applied to the notional system to predict the semiconductor loss.

For the notional system shown in Fig. 1.1, one of the assumptions is that the system is operated at full load. At full load, the output inductor waveform is assumed to be as in Fig. 2.1. Because the output inductor current is always positive, only transistor $T_1$ and diode $D_2$ conduct under full load condition. The function of $D_1$ and $T_2$ is to avoid the discontinuous conduction mode [23] under light load. In Fig. 2.1, $d$ is the duty cycle, $i_{mn}$ and $i_{mx}$ are the minimum and maximum output inductor current, $T_{sw}$ is the switching period, $\overline{i_l}$ is the average output inductor current, $\Delta i_l$ is the output inductor current ripple. The current extrema $i_{mn}$ and $i_{mx}$ may be expressed as $i_{mn} = \overline{i_l} - \Delta i_l / 2$, $i_{mx} = \overline{i_l} + \Delta i_l / 2$.

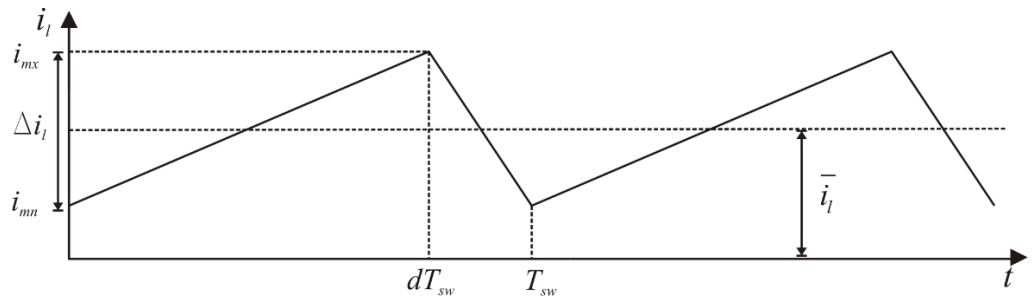


Fig. 2.1 Output Inductor Current Waveform

With the loss model set forth in Section 2.1 and the current waveform shown in Fig. 2.1, the dc-dc converter semiconductor loss can be calculated [7]. The average transistor conduction loss $P_{t,cd}$ is expressed as

$$P_{t,cd} = d\left(\frac{\alpha_{t,cd}(i_{mx}+i_{mn})}{2} + \frac{\beta_{t,cd}(i_{mx}^{\gamma_{t,cd}+1} - i_{mn}^{\gamma_{t,cd}+1})}{(\gamma_{t,cd}+1)(i_{mx}-i_{mn})i_b^{\gamma_{t,cd}}}\right) \tag{2.7}$$

The transistor switching loss is given by

$$P_{t,sw} = f_{sw}E_{t,on}(i_{mn}, v_t) + f_{sw}E_{t,off}(i_{mx}, v_t) \tag{2.8}$$

where $f_{sw}$ is the switching frequency.

The average diode conduction loss $P_{d,cd}$ may be expressed

$$P_{d,cd} = (1-d)\left(\frac{\alpha_{d,cd}(i_{mx}+i_{mn})}{2} + \frac{\beta_{d,cd}(i_{mx}^{\gamma_{t,cd}+1} - i_{mn}^{\gamma_{t,cd}+1})}{(\gamma_{d,cd}+1)(i_{mx}-i_{mn})i_b^{\gamma_{t,cd}}}\right) \tag{2.9}$$

The diode reverse recovery loss is expressed

$$P_{d,rr} = v_c^2 I_{rr}(i_{mn}) t_{rr}(i_{mn}) / (4v_{d,b}T_{sw}) \tag{2.10}$$

where $v_c$ is the input capacitor voltage.

For the rectifier loss analysis, since the switching frequency of the rectifier diode is low, the reverse recovery loss is neglected. The rectifier operation is divided into a commutation interval and conduction interval. During the commutation interval, the dc link current $i_r(t)$ is shared between two diodes and a third one completes the return path. During the conduction interval, $i_r(t)$ travels through two diodes. To find the rectifier loss, the commutation period is neglected and the rectifier loss is approximated as

$$P_{rec,cd}(i_r(t)) = 2\left(\frac{1}{T_f}\int_0^{T_f} p_{d,cd}(i_r(t))dt\right) \tag{2.11}$$

where $T_f$ is the period of the fundamental frequency of the generator and $i_r(t)$ can be achieved based on the waveform reconstruction algorithm [24]. In (2.11), the integration is evaluated numerically.

To quantify the advantage of WBG devices over Si devices for the case study of Section 6.3, appropriate Si and SiC semiconductors are selected based on the notional system voltage and current ratings. Loss model parameters of the selected devices are given in Section 2.3 and Section 2.4, respectively.

## 2.3 Si Semiconductor Loss

For the Si semiconductor devices, an IGBT and a fast switching PN junction diode are selected. The Si IGBT conduction loss and switching loss can be calculated based on (2.7) and (2.8), respectively. The Si PN junction diode conduction loss and reverse recovery loss can be

calculated based on (2.9) and (2.10), respectively. The Si rectifier loss can be calculated based on (2.11). Thus the total Si semiconductor loss is expressed as

$$P_{Si,semi} = P_{t,cd} + P_{t,sw} + P_d + P_{rec,cd} \tag{2.12}$$

where $P_d$ is the summation of $P_{d,cd}$ and $P_{d,rr}$.

The model parameters used in (2.7)-(2.11) are obtained by fitting the Microsemi APT13GP120B IGBT datasheet [25] and Powerex CS241250D diode datasheet [26] to (2.1)-(2.6). The datasheet and fitted IGBT characteristics are shown in Fig. 2.2-Fig. 2.4 where $T_j$ denotes the junction temperature and $V_{CE}$ denotes the collector-to-emitter voltage. Similar results for the diode can be found in [7]. The model parameters are listed in Table 2.1 and Table 2.2.

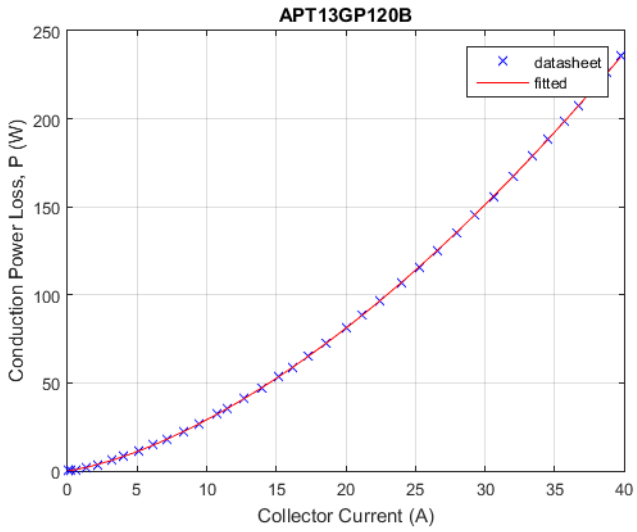


Fig. 2.2 Fitted IGBT Conduction Power Loss at $T_j = 125°C$

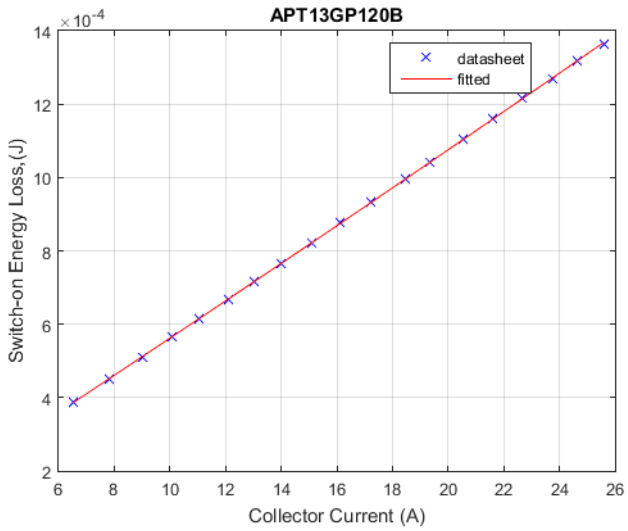


Fig. 2.3 Fitted IGBT Switch-On Energy Loss at $T_j = 125°C$ , $V_{CE} = 600V$

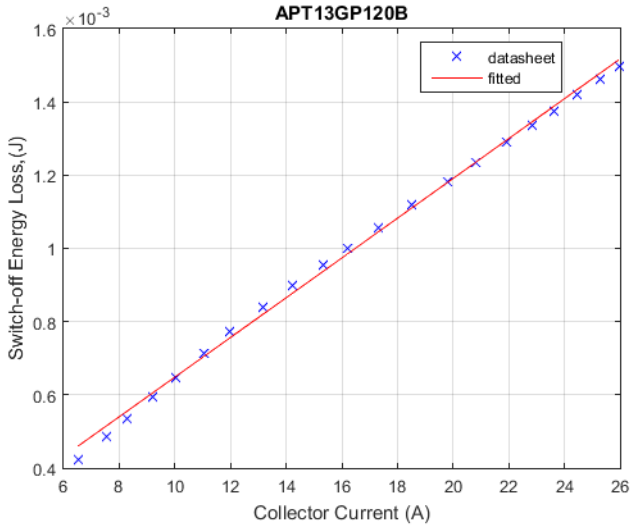


Fig. 2.4 Fitted IGBT Switch-Off Energy Loss at $T_j = 125°C$ , $V_{CE} = 600V$

Table 2.1 APT13GP120B Loss Model

| | |
|---|---|
| $\alpha_{t,cd}$ = 1.1119 V | $\gamma_{t,on} = 6.1034 \cdot 10^{-5}$ J |
| $\beta_{t,cd}$ = 0.3468 V | $\alpha_{t,off} = 1 \cdot 10^{-8}$ J/A$^2$ |
| $\gamma_{t,cd}$ = 1.7135 | $\beta_{t,off} = 5.396 \cdot 10^{-5}$ J/A |
| $\alpha_{t,on} = 6.337 \cdot 10^{-8}$ J/A$^2$ | $\gamma_{t,off} = 1.0779 \cdot 10^{-4}$ J |
| $\beta_{t,on} = 4.945 \cdot 10^{-5}$ J/A | $v_{t,b}$ = 600V |

Table 2.2 CS241250D Loss Model

| | |
|---|---|
| $\alpha_{d,cd}$ = 0.4131 V | $\gamma_{trr}$ = 0.1275 |
| $\beta_{d,cd}$ =0.2799 V | $\alpha_{irr} = 1.7636 \cdot 10^{-6}$ |
| $\gamma_{d,cd}$ = 1.3553 | $\beta_{irr}$ = 4.1159 |
| $\alpha_{trr} = 3.1 \cdot 10^{-9}$ s/A | $\gamma_{irr}$ = 0.6493 |
| $\beta_{trr} = 2.609 \cdot 10^{-7}$ s | $v_{d,b}$ = 600V |

## 2.4 SiC Semiconductor Loss

The SiC MOSFET conduction loss and switching loss can be calculated based on (2.7) and (2.8), respectively. Since the SiC Schottky diode is a majority-carrier device, there are no minority carriers stored during forward conduction. Thus, the dc-dc converter diode reverse recovery loss is neglected. The diode conduction loss can be calculated from (2.9). The rectifier loss can be calculated from (2.11). Thus the SiC semiconductor loss is expressed as

$$P_{SiC,semi} = P_{t,cd} + P_{t,sw} + P_d + P_{rec,cd} \tag{2.13}$$

where $P_d$ equals to $P_{d,cd}$ .The model parameters used in (2.7)-(2.9) and (2.11) are obtained by curve fitting to the Cree C2M0080120D MOSFET datasheet [27] and the Cree C4D20120A diode datasheet [28]. The results for the SiC MOSFET are shown in Fig. 2.5-Fig. 2.7 where $V_{DS}$ denotes

the drain-to-source voltage. The diode result is shown in Fig. 2.8. The model parameters are listed in Table 2.3 and Table 2.4.

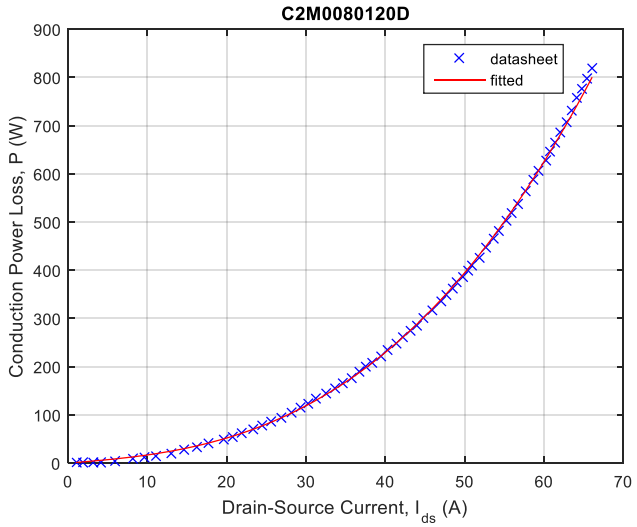


Fig. 2.5 Fitted SiC MOSFET Conduction Loss at $T_j = 150°C$

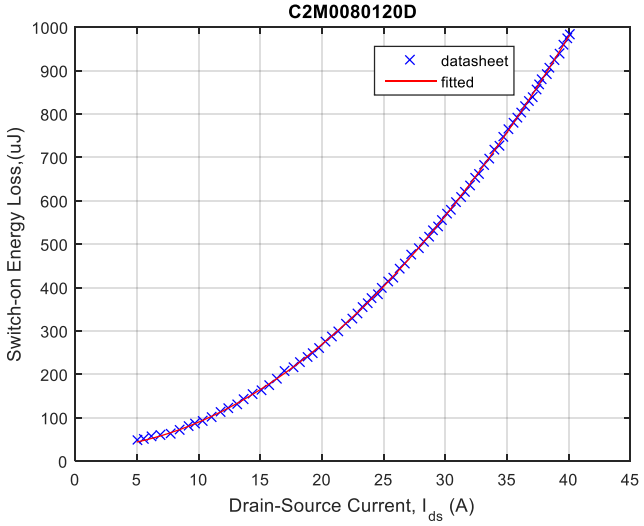


Fig. 2.6 Fitted SiC MOSFET Switch-On Energy Loss at $T_j = 25°C$, $V_{DS} = 800V$

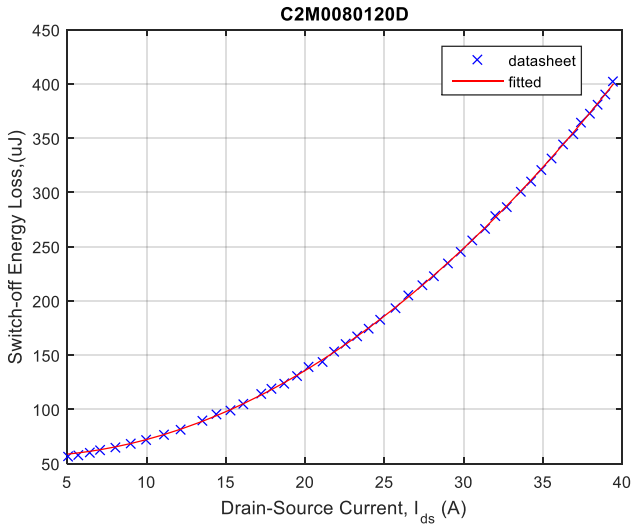


Fig. 2.7 Fitted SiC MOSFET Switch-Off Energy Loss at $T_j = 25°C$, $V_{DS} = 800V$

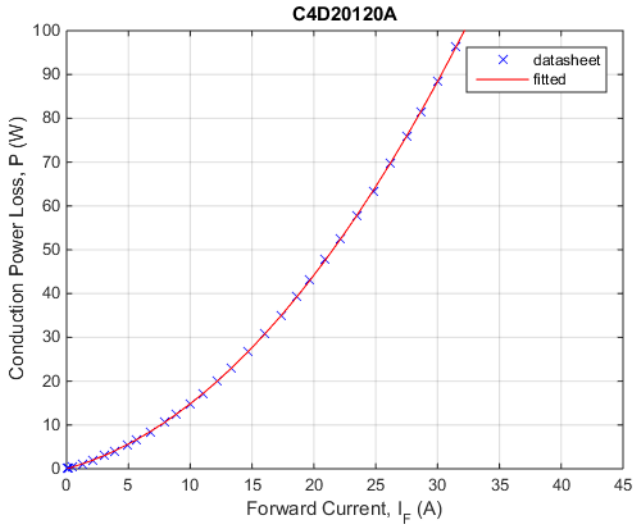


Fig. 2.8 Fitted SiC Diode Conduction Loss at $T_j = 175°C$

Table 2.3 C2M0080120D Loss Model

| | |
|---|---|
| $\alpha_{t,cd}$ = 1.3028 V | $\gamma_{t,on}$ = 2.7409·10$^{-5}$ J |
| $\beta_{t,cd}$ = 0.0064 V | $\alpha_{t,off}$ = 2.454·10$^{-7}$ J/A$^2$ |
| $\gamma_{t,cd}$ = 2.7744 | $\beta_{t,off}$ = -9.938·10$^{-7}$ J/A |
| $\alpha_{t,on}$ = 5.852·10$^{-7}$ J/A$^2$ | $\gamma_{t,off}$ = 5.7478·10$^{-5}$ J |
| $\beta_{t,on}$ = 3.752·10$^{-7}$ J/A | $v_{t,b}$ = 800V |

Table 2.4 C4D20120A Loss Model

| | | |
|---|---|---|
| $\alpha_{d,cd}$ = 0.7921 V | $\beta_{d,cd}$ = 0.0641 V | $\gamma_{d,cd}$ = 2.0335 |

## 2.5 Semiconductor Thermal Model

In this section, the semiconductor heat sink mass $M_H$ is determined. To fully utilize the WBG device's high junction temperature rating, each semiconductor is assigned its own heatsink and assumed to be operated at its highest allowed junction temperature. The thermal equivalent circuit shown in Fig. 2.9 is used here to calculate the required heat sink-to-ambient thermal resistance $R_{s,ha}$ for each semiconductor.

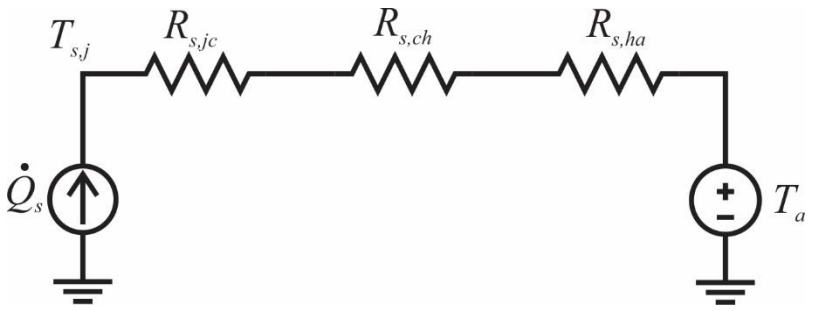


Fig. 2.9 Semiconductor Thermal Equivalent Circuit

In Fig. 2.9, $T_a$ is the ambient temperature, $\dot{Q}_s$ denotes the semiconductor power loss, $T_{s,j}$ denotes the semiconductor junction temperature, $R_{s,jc}$ denotes the semiconductor junction-to-case thermal resistance, $R_{s,ch}$ denotes the case-to-heat sink thermal resistance, and the subscript *s* is either $T_1$, $D_2$, or *rec* to designate transistor $T_1$, diode $D_2$, or rectifier diode thermal parameters, respectively. For transistor $T_1$, $R_{T_1,ha}$ is calculated as

$$R_{T_1,ha} = \frac{T_{T_1,j} - T_a - (P_{t,cd} + P_{t,sw})(R_{T_1,jc} + R_{T_1,ch})}{P_{t,cd} + P_{t,sw}} \tag{2.14}$$

For diode $D_2$, $R_{D_2,ha}$ is calculated as

$$R_{D_2,ha} = \frac{T_{D_2,j} - T_a - P_d(R_{D_2,jc} + R_{D_2,ch})}{P_d} \tag{2.15}$$

For rectifier diode, $R_{rec,ha}$ is calculated as

$$R_{rec,ha} = \frac{T_{rec,j} - T_a - P_{rec,cd}(R_{rec,jc} + R_{rec,ch})/6}{P_{rec,cd}/6} \tag{2.16}$$

where $T_{T_1,j}$, $T_{D_2,j}$, and $T_{rec,j}$ are the maximum allowed junction temperature of the respective devices.

The transistor $T_2$ and diode $D_1$ are not considered in the semiconductor thermal analysis because of the full load operation assumption mentioned in Section 2.1. The aluminum plate fin heat sink model [7] is used here to calculate the heat sink mass $M_{s,H}$ for each semiconductor

$$M_{s,H} = \frac{a_1}{(R_{s,ha}/R_b)^{n_1}} + \frac{a_2}{(R_{s,ha}/R_b)^{n_2}} \tag{2.17}$$

where $a_1, a_2, n_1, n_2, R_b$ are model parameters which are listed in Table 2.5.

The total semiconductor heat sink mass is calculated as

$$M_H = M_{T_1,H} + M_{D_2,H} + 6M_{rec,H} \tag{2.18}$$

The thermal parameters of the semiconductors applied in Section 2.3 and Section 2.4 are listed in Table 2.6-Table 2.9.

Table 2.5 Aluminum Plate Fin Heat Sink Model Parameters [7]

| | |
|---|---|
| $a_1$ = 0.1516 kg | $n_2$ = 5.5445 |
| $a_2$ = 7.5568·10$^{-5}$ kg | $R_b$ = 1 °C/W |
| $n_1$ = 1.1688 | |

Table 2.6 APT13GP120B Thermal Parameters [25]

| | |
|---|---|
| $T_j$ = 150 °C | $R_{jc}$ = 0.5 °C/W |
| $R_{ch}$ = 0.3 °C/W | $T_a$ = 25 °C |

Table 2.7 CS241250D Thermal Parameters [26]

| | |
|---|---|
| $T_j$ = 150 °C | $R_{jc}$ = 0.6 °C/W |
| $R_{ch}$ = 0.4 °C/W | $T_a$ = 25 °C |

Table 2.8 C2M0080120D Thermal Parameters [27]

| | |
|---|---|
| $T_j$ = 150 °C | $R_{jc}$ = 0.6 °C/W |
| $R_{ch}$ = 0.45 °C/W | $T_a$ = 25 °C |

Table 2.9 C4D20120A Thermal Parameters [28]

| | |
|---|---|
| $T_j$ = 175 °C | $R_{jc}$ = 0.62 °C/W |
| $R_{ch}$ = 0.45 °C/W | $T_a$ = 25 °C |

# 3. PASSIVE COMPONENT MODELS

Passive components in power conversion system are used to limit current and voltage ripple and to stabilize the system during disturbances through their inherent energy storage. However the passive components will introduce extra loss to the system and the passive component mass is a significant component of the total power converter system mass. Thus it is necessary to derive the passive component mass and loss models. For the notional dc generation system, significant current harmonics exist in the rectifier dc current $i_r$. A dc filter is connected to the rectifier to suppress this harmonic content. Since the fundamental frequency of the $i_r$ harmonic is relatively low (six times of the generator electrical frequency), a ferromagnetic core PMI is used herein to reduce the inductor size since ferromagnetic material has high saturation flux density. Since the capacitor in the dc filter sees the high frequency component from the dc-dc converter in addition to the low frequency component from the rectifier, a polypropylene capacitor is used. Due to the application of switch-mode dc-dc converter, the output current $i_{out}$ contains the switching frequency harmonic component. The ferrite magnetic material is used for the output PMI to limit the $i_{out}$ current ripple and to reduce high frequency loss. The polypropylene capacitor ($C_{outp}$) is used as the output filter capacitor to reduce the output voltage ($v_{out}$) switching frequency ripple. A large electrolytic capacitor ($C_{oute}$) is used in the dc-dc converter output stage to stabilize $v_{out}$ under disturbances since the disturbance frequency is relatively low (hundreds to few thousands Hz) and the electrolytic capacitor has high energy density.

## 3.1 Metamodeling of PMI

Due to the dc component of the current, conventional dc-link inductors need a large magnetic cross sectional area to avoid saturation which increases mass. In [7], a PMI is proposed to partially cancel the dc current flux bias. Therein, the geometry of the PMI is optimized to minimize the mass and the loss. However, the design approach proposed in [7] is computationally too intense to be conveniently imbedded in the dc generation system optimization based design. The large design space will slow the convergence.

In this section, a metamodel based approach to representing PMI at a system level is established. A metamodel is a model of a model. In [29], magnetic equivalent circuit (MEC) based scaling laws are derived and are used to develop a UI core inductor metamodel. The same approach is applied to the PMI herein. In particular, the PMI design model is normalized and made scale independent. Then a multi-objective optimization problem is formulated to minimize the normalized mass and normalized loss. Then a curve fitting technique is applied to the optimization result (a Pareto-optimal front) to achieve the metamodel parameters. With the established metamodel, given rated PMI inductance, rated PMI current, and PMI current density, the PMI mass and PMI dc loss can be estimated. In such way, the PMI design space shrinks from sixteen design parameters in [7] to only one design parameter (current density) with the metamodel.

It is important to remember that the metamodel approach is not a substitute for detailed PMI design. The detailed PMI design is conducted using a modified design approach based on [7].

### 3.1.1 PMI Geometry and MEC

The PMI geometry and the MEC are shown in Fig. 3.1 and Fig. 3.2, respectively. In Fig. 3.1, $w_i$ , $w_b$ , $w_e$ , $w_s$ and $w_c$ are the widths of the I core, base, end leg, slot and center leg, respectively, $d_s$ is the depth of the slot, $d_w$ and $w_w$ are the depth and width of the winding, respectively, $w_{ex}$ is the width of the external flux path, $g_c$ is the length of the center air gap, $g_e$ is the length of the end air gap, and $l_{pm}$ is the length of the permanent magnet. The 'N' and 'S' designate the north and south magnet poles. The circled "×" symbolizes current flowing into the page through the bundle of conductors and the circled dot symbolizes current flowing out of the page. The depth of the core into the page is denoted $d_c$ .

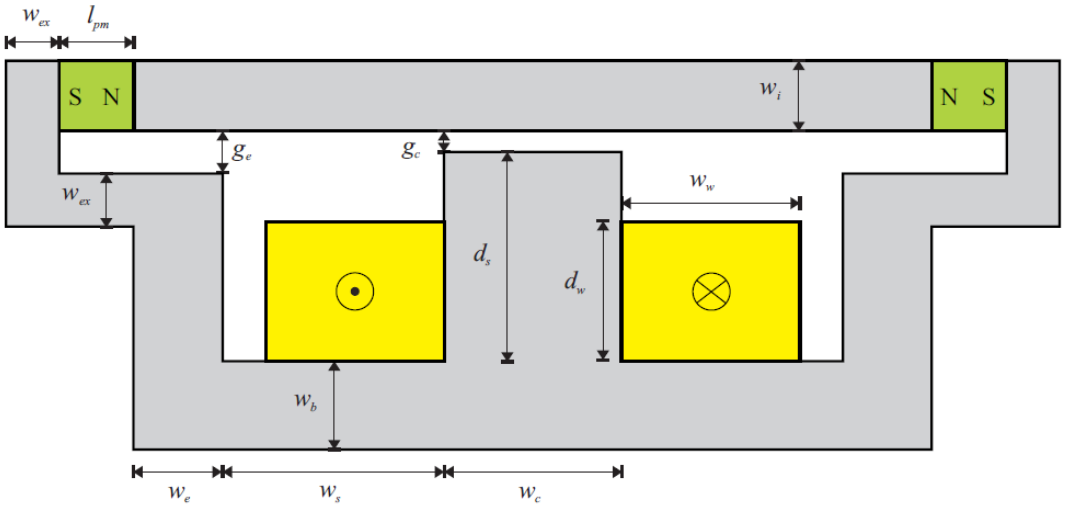


Fig. 3.1 PMI Geometry [7]

In [7], a MEC based design approach is proposed to design the PMI shown in Fig. 3.1. The definition of a standard MEC branch is given in [30] and the MEC network is shown in Fig 3.2. The parameters of this network including permeance $P_k$, flux source $\Phi_k$ and Magnetic Motive Force (MMF) source $F_k$ are derived in [7], where $k$ is the MEC branch number.

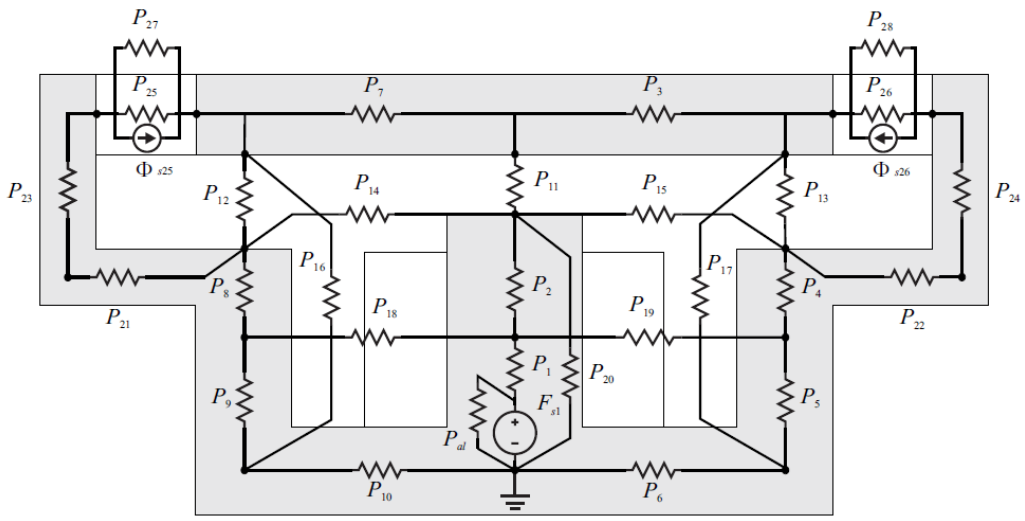


Fig. 3.2 PMI MEC [7]

### 3.1.2 PMI Parameters Normalization

To establish the PMI metamodel, a normalized PMI model is needed. The first step is to choose the normalization base. For a dc filter inductor, the normalization base $D$ can be calculated by [29]

$$E_{mi} = \frac{1}{2} L_{inc} i_{pk}^2 \tag{3.1}$$

$$D = E_{mi}^{1/3} \tag{3.2}$$

where $E_{mi}$ is the energy metric, $L_{inc}$ is the desired incremental inductance and $i_{pk}$ is the peak average current applied to the inductor over all operating points. After the base is established, all quantities except the field intensity $H$ and flux density $B$ are scaled using the following equations [29]

$$\hat{x} = x / D \tag{3.3}$$

$$\hat{a} = a / D^2 \tag{3.4}$$

$$\hat{v} = v / D^3 \tag{3.5}$$

$$\hat{M} = M / D^3 \tag{3.6}$$

$$\hat{J} = JD \tag{3.7}$$

$$\hat{P}_{dc} = P_{dc} / D \tag{3.8}$$

$$\hat{E} = E / D^3 \tag{3.9}$$

$$\hat{t} = t / D^2 \tag{3.10}$$

$$\hat{i} = i / D \tag{3.11}$$

$$\hat{\lambda} = \lambda / D^2 \tag{3.12}$$

$$\hat{F} = F / D \tag{3.13}$$

$$\hat{\Phi} = \Phi / D^2 \tag{3.14}$$

$$\hat{P} = P / D \tag{3.15}$$

where $x$ denotes the linear dimension, $a$ denotes the area, $v$ denotes the volume, $M$ denotes the mass, $J$ denotes the current density, $P_{dc}$ denotes the power, $E$ denotes the energy, $t$ denotes the time, $i$ denotes the current, $\lambda$ denotes the flux linkage, $F$ denotes the MMF, $\Phi$ denotes the flux, and $P$ denotes the permeance. In (3.3) – (3.15) and throughout this chapter, a "ˆ" denotes the normalized parameter.

### 3.1.3 PMI Magnetic Analysis

The PMI magnetic analysis is performed herein to form the normalized PMI design constraints. For the PMI considered herein, it is desired to obtain an incremental inductance $L_{inc}$ at a peak rated current $i_{pk}$. The incremental inductance $L_{inc}$ can be expressed as

$$L_{inc} = \frac{\partial \lambda}{\partial i} \tag{3.16}$$

The associated energy metric is expressed as

$$E_m = \frac{1}{2} L_{inc} i_{pk}^2 \tag{3.17}$$

In the metamodeling procedure, all quantities are scale independent. Based on (3.16) and (3.17), the normalized energy metric is expressed as

$$\hat{E}_m = \frac{1}{2} \frac{\Delta \hat{\Phi}_m}{\Delta \hat{F}} \hat{F}_{pk}^2 \tag{3.18}$$

where $\hat{F}_{pk}$ is the normalized MMF at rated current, $\Delta \hat{F}$ is an MMF change, and $\Delta \hat{\Phi}_m$ is the resulting branch 1 flux change which is the total flux change of the PMI. The MMF change is taken as

$$\Delta \hat{F} = \delta \hat{F}_{pk} \tag{3.19}$$

where $\delta$ is a design specification. Based on (3.2) and (3.9), the required normalized energy metric is $\hat{E}_{mi} = 1$. Thus the constraint $\hat{E}_m > \hat{E}_{mi}$ will ensure the PMI's incremental inductance is greater than the required incremental inductance. To solve $\hat{E}_m$, $\hat{F}_{pk}$ and $\Delta \hat{\Phi}_m$ need to be determined.

In [29], the current density is used to calculate $F_{pk}$ instead of number of turns. This approach is applied herein. The current density $J_{pk}$ is expressed as

$$J_{pk} = \frac{Ni_{pk}}{w_w d_w k_{pf}} \tag{3.20}$$

where $k_{pf}$ is the packing factor. With the current density given in (3.20), the $F_{pk}$ is expressed as

$$F_{pk} = J_{pk} d_w w_w k_{pf} \tag{3.21}$$

The normalized MMF $\hat{F}_{pk}$ is expressed as

$$\hat{F}_{pk} = \hat{J}_{pk} \hat{d}_w \hat{w}_w k_{pf} \tag{3.22}$$

To calculate the $\Delta\hat{\Phi}_m$, the MEC network shown in Fig. 3.2 need to be solved. The MEC Toolbox [30] is applied herein to solve the MEC. Detailed information is given in [7].

To insure a valid design, the MEC need to be evaluated four times with different MMF values. The first two evaluations are performed at nearly rated current condition to ensure the incremental inductance is greater than the required inductance. The third and fourth evaluation are performed at nearly zero current condition to ensure the PMs do not saturate the PMI core. Four analyses' MMF are set as $\hat{F}_{pk} + 0.5\Delta\hat{F}$, $\hat{F}_{pk} - 0.5\Delta\hat{F}$, $0.5\Delta\hat{F}$ and $-0.5\Delta\hat{F}$, respectively. The result of n$^{th}$ evaluation contains the branch $k$ flux $\hat{\Phi}_{k,n}$ and the convergence index $e_n$ [31]. If the MEC converge, $e_n$ is set as 1, otherwise $e_n$ is set as 0. Then the energy metric is evaluated by (3.18) where $m$ is either 1 or 2 and $\Delta\hat{\Phi}_1 = \hat{\Phi}_{1,1} - \hat{\Phi}_{1,2}$, $\Delta\hat{\Phi}_2 = \hat{\Phi}_{1,3} - \hat{\Phi}_{1,4}$.

It is noted that in order to insure that the MEC is accurate, the main component of flux must go through the core and the bulk of the MMF drop must occur in the air gap [29]. Thus the branch 11 flux $\hat{\Phi}_{11,2}$, branch 11 MMF drop $\mathrm{F}_{11,2}$ and branch 13 MMF drop $\mathrm{F}_{13,2}$ are also calculated at the second MMF evaluation where the MMF source is $\hat{F}-0.5\Delta\hat{F}$. Then the constraints can be expressed as $\hat{\Phi}_{11,2}>\delta_a\hat{\Phi}_{1,2}$ and $\mathrm{F}_{11,2}+\mathrm{F}_{13,2}>\delta_a(\hat{F}-0.5\Delta\hat{F})$, where $\delta_a$ is a numerical value.

Since there are two PMs in the PMI, it is necessary to add a constraint to ensure the PMs are not demagnetized at the maximum operated current which has the MMF source set as $\hat{F}+0.5\Delta\hat{F}$. The field intensity in the PM is expressed as [31]

$$H_{pm}=\frac{B_{pm}-B_r}{\mu_0(1+\chi_m)} \tag{3.23}$$

where $B_{pm}$ is the PM flux density, $B_r$ is the residual flux density, $\mu_0$ is the vacuum permeability and $\chi_m$ is the susceptibility. $B_r$ and $\chi_m$ are material properties tied to the PM type and temperature. $B_{pm}$ can be calculated from

$$B_{pm}=\frac{\hat{\Phi}_{26,1}}{\hat{w}_i\hat{d}} \tag{3.24}$$

where $\hat{\Phi}_{26,1}$ is the flux of branch 26 evaluated at maximum current condition. To ensure the PM is not demagnetized, the $H_{pm}$ must be larger than the minimum allowed field intensity which is set as $0.75\,H_{ci}$ herein where $H_{ci}$ is the intrinsic coercive force of the PM.

### 3.1.4 Normalized PMI Design Algorithm

With the information provided from Section 3.1.1 – Section 3.1.3, the normalized PMI design process is posed as a formal multi-objective optimization problem to minimize the normalized PMI mass $\hat{M}_{PMI}$ and normalized PMI dc loss $\hat{P}_{PMI}$. The PMI mass $\hat{M}_{PMI}$ can be expressed as

$$\hat{M}_{PMI} = \rho_{mc}\hat{v}_{mc} + \rho_c\hat{v}_c + \rho_{pm}\hat{v}_{pm} \tag{3.25}$$

where $\rho_{mc}$, $\rho_c$, $\rho_{pm}$ are the mass density of magnetic core material, conductor material and PM, respectively, $\hat{v}_{mc}$, $\hat{v}_c$ and $\hat{v}_{pm}$ are the normalized volume of magnetic core, conductor and PM, respectively. The expressions of $v_{mc}$, $v_c$ and $v_{pm}$ can be found in [7]. The PMI dc loss $\hat{P}_{PMI}$ is expressed as

$$\hat{P}_{PMI} = \hat{v}_c\hat{J}_{pk}^2 / \sigma_c \tag{3.26}$$

where $\sigma_c$ is the conductor conductivity and $\hat{J}_{pk}$ is the normalized current density.

The first step of the design process is to define the design space. The design vector $\hat{\theta}_{PMI}$ is selected as

$$\hat{\theta}_{PMI} = [\hat{g}_c\ \hat{g}_e\ \hat{d}_s\ \hat{w}_s\ r_{dws}\ r_{wws}\ \hat{w}_i\ \hat{d}\ r_{wei}\ r_{wci}\ r_{wbi}\ r_{wexe}\ \hat{J}_{pk}\ \hat{l}_{pm}\ t_{pm}] \tag{3.27}$$

where $\hat{g}_c$, $\hat{g}_e$, $\hat{d}_s$, $\hat{w}_s$, $\hat{w}_i$, $\hat{d}$, $\hat{l}_{pm}$ are the normalized geometry parameters, $r_{dws}$, $r_{wws}$, $r_{wei}$, $r_{wci}$, $r_{wbi}$, $r_{wexe}$ are the geometry ratios defined as $r_{dws} = \hat{d}_w / \hat{d}_s$, $r_{wws} = \hat{w}_w / \hat{w}_s$, $r_{wei} = \hat{w}_e / \hat{w}_i$, $r_{wci} = \hat{w}_c / (2\hat{w}_i)$, $r_{wbi} = \hat{w}_b / \hat{w}_i$, $r_{wexe} = \hat{w}_{ex} / \hat{w}_e$, respectively, and $t_{pm}$ is the magnet type. It is noted

that the current density is selected as a design parameter although the PMI design approach in [7] chose number of turns $N$ as a design parameter.

To formulate the optimization constraints, it is convenient to define the less than or equal to function $\mathrm{ltn}()$ and greater than or equal to function $\mathrm{gtn}()$ as

$$\mathrm{ltn}(x, x_0) = \begin{cases} 1 & x \le x_0 \\ 1/(1 + x - x_0) & x > x_0 \end{cases} \tag{3.28}$$

$$\mathrm{gtn}(x, x_0) = \begin{cases} 1 & x \ge x_0 \\ 1/(1 + x_0 - x) & x < x_0 \end{cases} \tag{3.29}$$

Next, the design constraints are imposed on the optimization. The first constraint is the MEC convergence constraint.

$$c_1 = \mathrm{mean}\left(e_1, e_2, e_3, e_4\right) \tag{3.30}$$

The second constraint is the energy constraint at rated current condition to ensure the PMI inductance is greater than the required inductance at rated current.

$$c_2 = \mathrm{gtn}\left(\hat{E}_1, 1\right) \tag{3.31}$$

The third constraint is the energy constraint at zero current condition. This constraint will ensure that the permanent magnet does not saturate the PMI at zero current.

$$c_3 = \mathrm{gtn}\left(\hat{E}_2, 1\right) \tag{3.32}$$

The fourth and fifth constraint are added here to insure the MEC is accurate.

$$c_4 = \mathrm{gtn}\left(\hat{\Phi}_{11,2}, \delta_a \hat{\Phi}_{1,2}\right) \tag{3.33}$$

$$c_5 = \text{gtn}\left(\hat{\text{F}}_{11,2} + \hat{\text{F}}_{13,2}, \delta_a(\hat{F} - 0.5\Delta\hat{F})\right) \tag{3.34}$$

The sixth constraint is to ensure that the PMs are not demagnetized.

$$c_6 = \text{gtn}\left(H_{pm}, 0.75H_{ci}\right) \tag{3.35}$$

In [31], it is pointed out that it is convenient to convert the constrained optimization problem into an unconstrained problem. To this end a multi-dimensional fitness function is defined as

$$\mathbf{f} = \begin{cases} \varepsilon\left(\dfrac{C_S - N_C}{N_C}\right)\begin{bmatrix}1\\1\end{bmatrix} & C_S < C_I \\ \begin{bmatrix}\hat{M}_{PMI}^{-1} & \hat{P}_{PMI}^{-1}\end{bmatrix}^T & C_S = N_C \end{cases} \tag{3.36}$$

where $\varepsilon$ is a small number. In (3.36), $C_I$ is the number of imposed constraints, $C_S$ is the number of satisfied constraints, and $N_C$ is the number of constraints. Initially $C_I = C_S = 0$. After imposing n$^{\text{th}}$ constraint $c_n$ both $C_I$ and $C_S$ are updated, where $C_I = C_I + 1$ and $C_S = C_S + c_n$. If a constraint is violated which will lead $C_S < C_I$, the rest of the constraints won't be evaluated and the algorithm will stop at an early stage in code to improve computational efficiency. In this case the fitness function will return a small negative number. If all constraints are satisfied, the fitness function will return the reciprocal value of system mass and system loss. The reciprocal value is used here because the optimization engine is set to maximize the fitness function.

### 3.1.5 Normalized PMI Design Case Study

To illustrate the design algorithm a case study is set forth. Herein, genetic algorithm is used to perform the optimization. In particular, the optimization engine Genetic Optimization System Engineering Tool (GOSET) [32] is applied here. The population size is set to 8000 and the generation size is set to 6000. The design space is set as in Table 3.1. The encoding in Table 3.1 represents how the design range of each design parameters is searched. “Log” means the range is searched logarithmically, “Lin” means the range is searched linearly and “Int” means only the integers in the range is searched. The permanent magnet types considered in the design space are listed in Table 3.2. The design specifications are listed in Table 3.3. The Hiperco 50 steel and the ferrite 3C90 are used as the magnetic core material of the notional dc generation system input PMI and output PMI, respectively. The material models are established in [7]. The material model parameters for Hiperco 50 and ferrite 3C90 are listed in Table 3.4 and Table 3.5, respectively.

Table 3.1 Normalized PMI Design Space

| Gene | Parameter | Min. | Max. | Encoding | Units |
|---|---|---|---|---|---|
| 1 | $\hat{g}_c$ | $3.1089 \cdot 10^{-4}$ | 0.0037 | Log | $m/J^{1/3}$ |
| 2 | $\hat{g}_e$ | 0.0012 | 0.0062 | Log | $m/J^{1/3}$ |
| 3 | $\hat{d}_s$ | 0.0062 | 0.0622 | Log | $m/J^{1/3}$ |
| 4 | $\hat{w}_s$ | 0.0062 | 0.0622 | Log | $m/J^{1/3}$ |
| 5 | $r_{dws}$ | 0.1 | 0.9 | Lin | N/A |
| 6 | $r_{wws}$ | 0.1 | 0.9 | Lin | N/A |
| 7 | $\hat{w}_i$ | 0.0124 | 0.0746 | Log | $m/J^{1/3}$ |
| 8 | $\hat{d}$ | 0.0373 | 0.3731 | Log | $m/J^{1/3}$ |
| 9 | $r_{wei}$ | 0.5 | 1.5 | Lin | N/A |
| 10 | $r_{wci}$ | 0.5 | 1.5 | Lin | N/A |
| 11 | $r_{wbi}$ | 0.5 | 1.5 | Lin | N/A |
| 12 | $r_{wexe}$ | 0.1 | 1.0 | Lin | N/A |
| 13 | $\hat{J}_{pk}$ | $1.6163 \cdot 10^{5}$ | $6.1135 \cdot 10^{6}$ | Log | $AJ^{1/3}/m^2$ |
| 14 | $\hat{l}_{pm}$ | 0.0012 | 0.0497 | Log | $m/J^{1/3}$ |
| 15 | $t_{pm}$ | 1 | 6 | Int | N/A |

Table 3.2 Permanent Magnet Material Mapping

| $t_{pm}$ | Permanent Magnet Material |
|---|---|
| 1 | Cast Alnico 5 |
| 2 | Cast Alnico 8H |
| 3 | SmCo5 Recoma 20 |
| 4 | Sm2Co17 Recoma 32 |
| 5 | NdFeB N42 |
| 6 | NdFeB N38SH |

Table 3.3 Normalized PMI Design Specification

| Specification | Value |
|---|---|
| $\delta$ | 0.01 |
| $\delta_a$ | 0.8 |
| $k_{pf}$ | 0.7 |

Table 3.4 Hiperco 50 Material Properties [7]

| Parameter | Value | Comment |
|---|---|---|
| $\rho_{mc}$ | 7844.64 kg/m$^3$ | Mass density |
| $B_{lim}$ | 2.0709 T | Recommended limit on B to avoid saturation |
| $\mu_r$ | 43371.96 | Relative permeability |
| $\alpha_k$ | [0.4378 $3.068\cdot10^{-4}$ $2.6279\cdot10^{-4}$ $2.4516\cdot10^{-4}$] 1/T | Permeability parameter |
| $\beta_k$ | [17.13367 2.139356 163.4648 1.476588] 1/T | Permeability parameter |
| $\gamma_k$ | [2.2836 1.3692 1.6772 3.494] T | Permeability parameter |

Table 3.5 Ferrite 3C90 Material Properties [7]

| Parameter | Value | Comment |
|---|---|---|
| $\rho_{mc}$ | 4743.3 kg/m$^3$ | Mass density |
| $B_{lim}$ | 0.44916 T | Recommended limit on B to avoid saturation |
| $\mu_r$ | 22266.62 | Relative permeability |
| $\alpha_k$ | [1.1542 $4.9742\cdot10^{-2}$ $4.9644\cdot10^{-2}$ $4.1155\cdot10^{-2}$] 1/T | Permeability parameter |
| $\beta_k$ | [431.1763 2.29503 15.04824 74.28908] 1/T | Permeability parameter |
| $\gamma_k$ | [0.4742 2.7955 0.59862 0.43996] T | Permeability parameter |

To ensure the optimization solution is converged, three studies with the same population and generation size are performed and the Pareto-optimal fronts are compared. Fig. 3.3 and Fig. 3.4 show that both the Hiperco core PMI and the ferrite core PMI results converged very well.

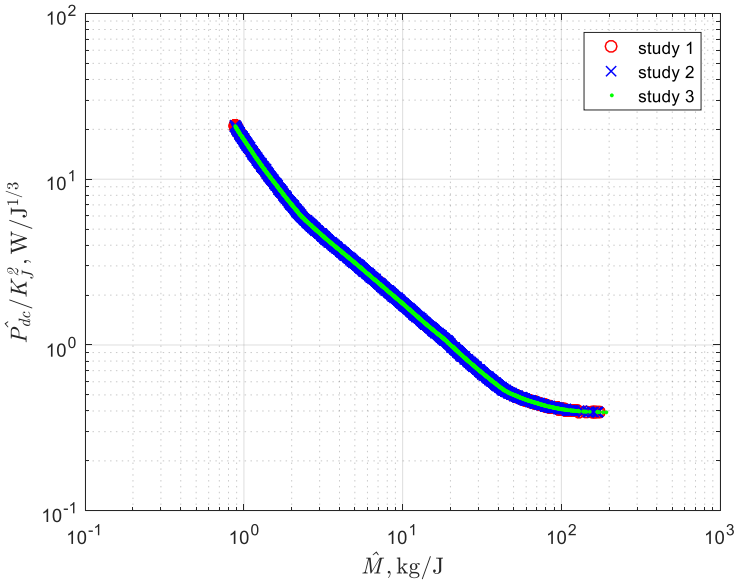


Fig. 3.3 Hiperco PMI Convergence Study

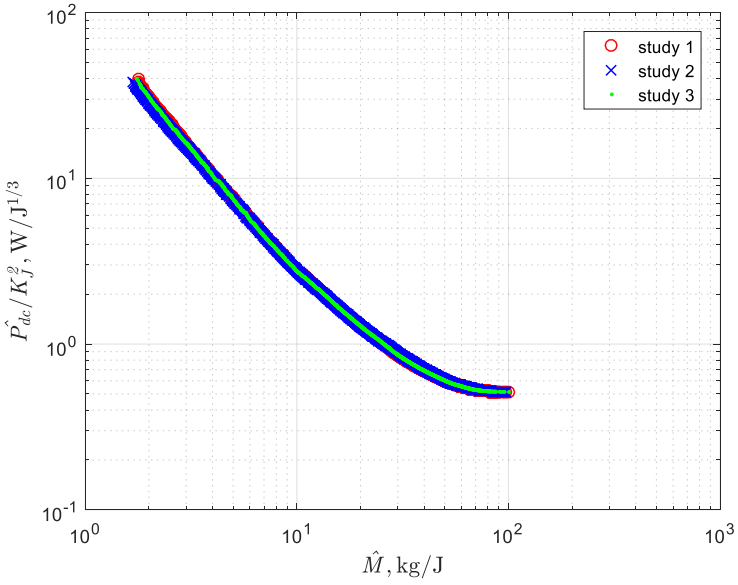


Fig. 3.4 Ferrite PMI Convergence Study

Fig. 3.5 and Fig. 3.6 show the gene distribution of the final population of designs for Hiperco core PMI and ferrite core PMI, respectively. The genes are ordered as listed in Table 3.1 and are shown normalized between 0 and 1. The genes are sorted by the PMI mass which means that the genes of designs with higher mass are toward the left of the parameter window, and the genes with lower mass are toward the right.

Comparing Fig. 3.5 and Fig. 3.6, it can be noticed that most genes have the same trend between two different core material PMIs except the gene 10 ( $\hat{w}_c / (2\hat{w}_i)$ ), gene 11 ( $\hat{w}_b / \hat{w}_i$ ) and gene 14 ( $\hat{l}_{pm}$ ). The reason of the differences of these three genes is because that ferrite material has a low saturation flux density thus it needs larger cross sectional area and larger PM branch reluctance to avoid saturation. For the rest of the genes, gene 1 denotes $\hat{g}_c$ which converged to the minimum limit which means the PMI designs want a zero center air gap; gene 2 denotes $\hat{g}_e$ which increased with decreasing mass; gene 3 and gene 4 denote $\hat{d}_s$ and $\hat{w}_s$ which decreased as the mass decreased; gene 5 and gene 6 denote $\hat{d}_w / \hat{d}_s$ and $\hat{w}_w / \hat{w}_s$ which converged to the maximum limit to maximize the slot utilization; gene 7-9 denote $\hat{w}_i$ , $\hat{d}$ and $\hat{w}_e / \hat{w}_i$ which decreased as the mass decreased; gene 12 denote $\hat{w}_{ex} / \hat{w}_e$ which increased as the mass decreased because as the inductor gets smaller, the width of the external flux path tends to be the same as the width of the end leg to avoid saturation; gene 13 denotes $\hat{J}_{pk}$ which increased as the mass decreased since higher current density will reduce the conductor mass; gene 15 denote the $t_{pm}$ which converged to NdFeB N42 PM grade and NdFeB N38SH grade since these two grade has higher residual flux density and higher absolute coercive force.

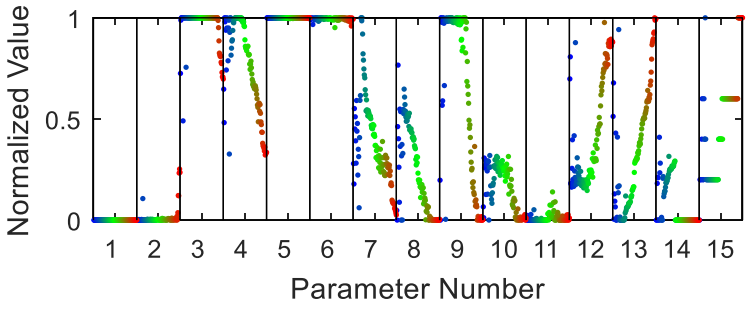


Fig. 3.5 Gene distribution for Hiperco PMI study 1

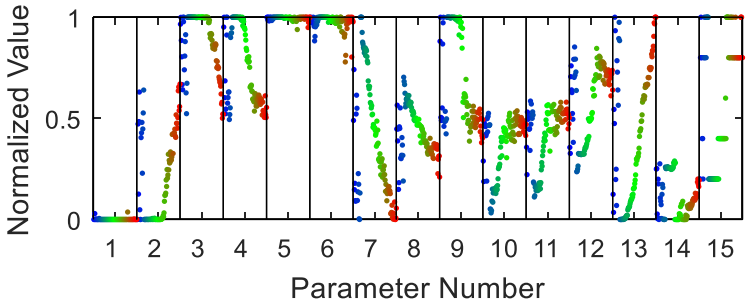


Fig. 3.6 Gene distribution for ferrite PMI study 1

In Fig. 3.7, the Hiperco core PMI and ferrite core PMI Pareto-optimal fronts are superimposed. The third Pareto-optimal front is from [29] which is a regular UI-shape ferrite core inductor. LL, NL and UL denote the designs that are against lower current density limit, not against current density limit and against upper current density limit, respectively. NMEC denotes normalized MEC. In Fig. 3.7, it can be seen that the Hiperco steel core PMI dominates the ferrite core PMI. This is because Hiperco steel has a higher saturation flux density than ferrite and because only dc loss is considered. It also shows that the PMI dominates the regular UI-shape inductor and commercial inductors. In Fig. 3.7, the black curves are inductor metamodels which will be introduced in the next section.

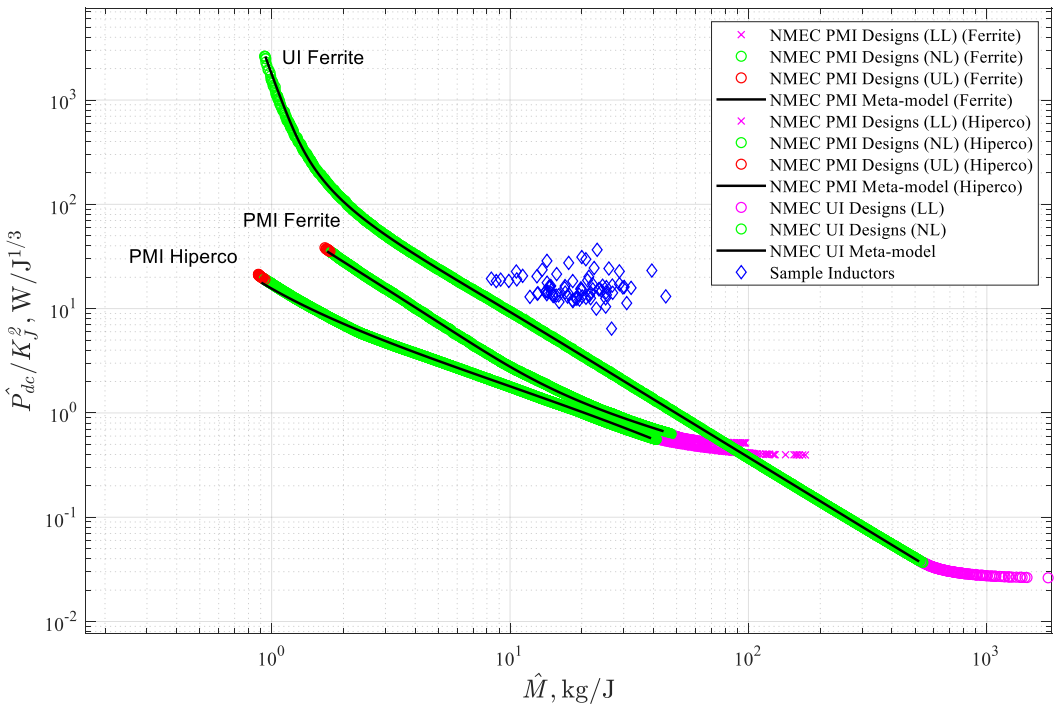


Fig. 3.7 Normalized Pareto-optimal front

### 3.1.6 PMI Metamodel

Based on the optimization results shown in Section 3.1.5, the normalized mass versus normalized current density of Hiperco and ferrite PMIs are shown in Fig. 3.8 and Fig. 3.9, respectively. The normalized dc power loss versus normalized current density of Hiperco PMI and ferrite PMI are shown in Fig. 3.10 and Fig. 3.11, respectively.

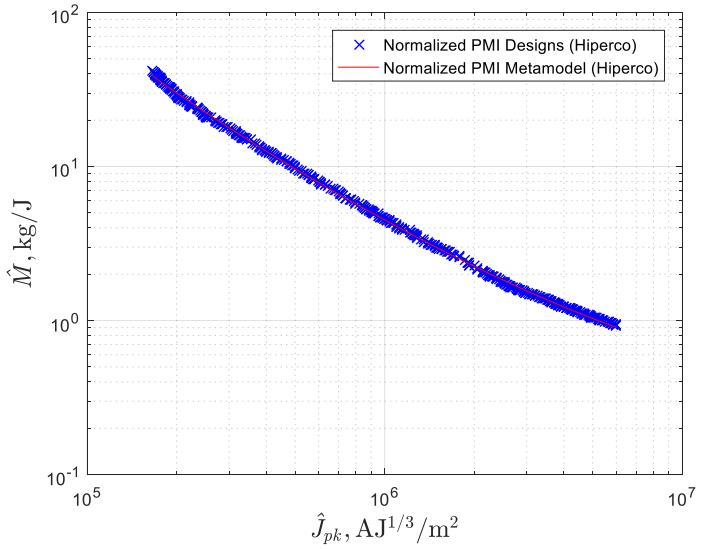


Fig. 3.8 Normalized mass versus normalized current density (Hiperco)

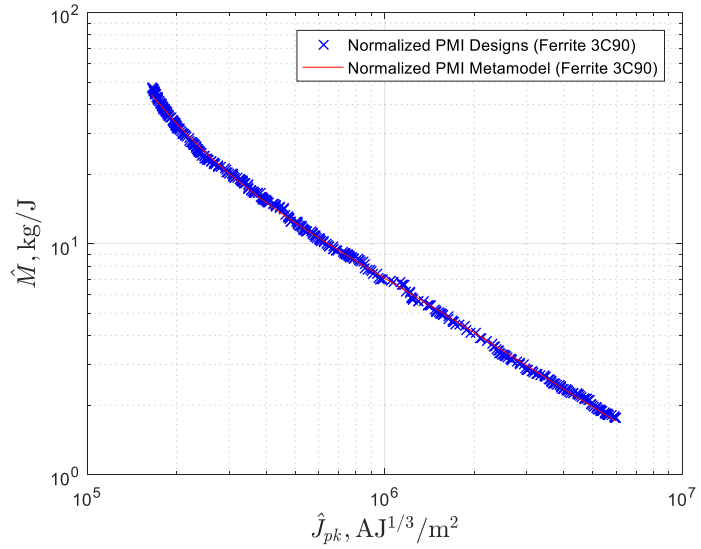


Fig. 3.9 Normalized mass versus normalized current density (Ferrite 3C90)

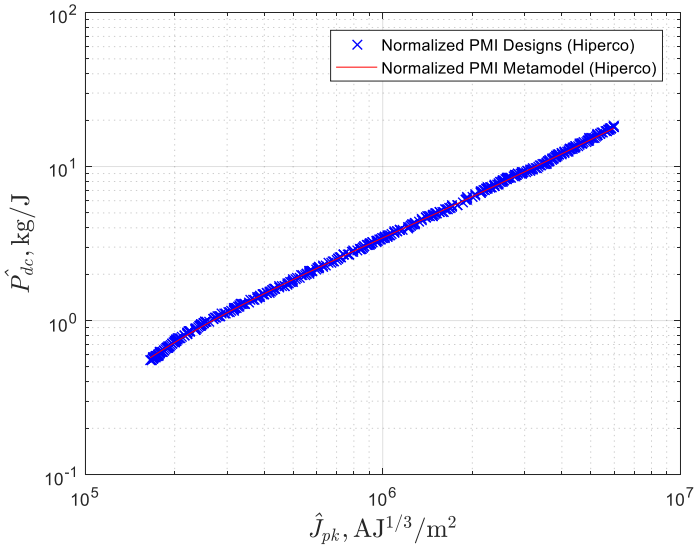


Fig. 3.10 Normalized dc power loss versus normalized current density (Hiperco)

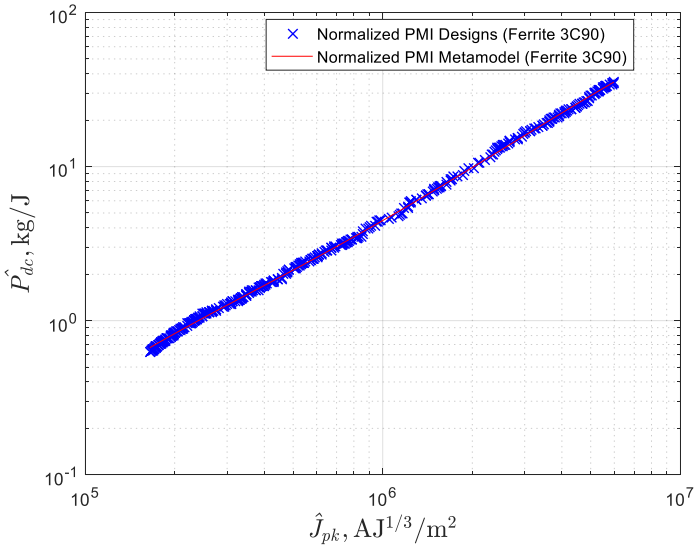


Fig. 3.11 Normalized dc power loss versus normalized current density (Ferrite 3C90)

The normalized PMI model can be achieved by fitting Fig. 3.8-Fig. 3.11 using the same fitting functions as set forth in [29]. Thus $\hat{M}_{PMI}$ and $\hat{P}_{PMI}$ can be expressed as

$$\hat{M}_{PMI} = c_M \prod_{k=1}^{K_M} \left( \hat{J}_{pk} + b_{M,k} \right)^{n_{M,k}} \tag{3.37}$$

$$\hat{P}_{PMI} = c_P K_J^2 \prod_{k=1}^{K_P} \left( \hat{J}_{pk} + b_{P,k} \right)^{n_{P,k}} \tag{3.38}$$

where $K_J$ is an application-dependent constant to relate the rms current density and the peak current density. The relationship is expressed as $J_{rms} = K_J J_{pk}$. For dc applications, $K_J = 1$.

Substitution of (3.2), (3.6), (3.7) and (3.8) into (3.37) and (3.38) yields

$$M_{PMI} = c_M E_{mi}^{\frac{1}{3}} \prod_{k=1}^{K_M} \left( J_{pk} E_{mi}^{\frac{1}{3}} + b_{M,k} \right)^{n_{M,k}} \tag{3.39}$$

$$P_{PMI} = c_P K_J^2 E_{mi}^{\frac{1}{3}} \prod_{k=1}^{K_P} \left( J_{pk} E_{mi}^{\frac{1}{3}} + b_{P,k} \right)^{n_{P,k}} \tag{3.40}$$

which is the PMI metamodel that applied to the notional dc generation system design.

For the Hiperco PMI, $c_M = 0.3670$, $c_P = 3.1838$, and $K_M$=$K_P$=7. For the ferrite PMI, $c_M = 5.1838 \cdot 10^3$, $c_P = 3.5855$, and $K_M$=$K_P$=7. The remaining parameters are given in Table 3.6 and Table 3.7. These parameters have been obtained by fitting (3.37) and (3.38) to Fig. 3.8 - Fig. 3.11. The fitted results are represented by the red curves of Fig. 3.8 - Fig. 3.11 which show that the fitted results match the normalized design results well.

The Equivalent Series Resistance (ESR) of the PMI is calculated as

$$r_{esr} = \frac{P_{PMI}}{i_{pk}^2} \tag{3.41}$$

Table 3.6 Hiperco PMI metamodel Parameters

| k | $b_{M,k}$ | $n_{M,k}$ | $b_{P,k}$ | $n_{P,k}$ |
|---|---|---|---|---|
| 1 | 0 | 0.0515 | 0 | -3.5860 |
| 2 | 100 | -3.4304 | 100 | 2.9868 |
| 3 | 237.1039 | 1.0266 | 100 | 2.8594 |
| 4 | 237.1039 | 1.5148 | 100 | 2.3135 |
| 5 | 237.1039 | -1.8021 | $3.1109 \cdot 10^4$ | -3.9952 |
| 6 | $4.1041 \cdot 10^4$ | 1.5511 | $1.5035 \cdot 10^6$ | 0.4735 |
| 7 | $1.0231 \cdot 10^7$ | 1.0769 | $2.4899 \cdot 10^8$ | -0.7637 |

Table 3.7 Ferrite PMI metamodel Parameters

| k | $b_{M,k}$ | $n_{M,k}$ | $b_{P,k}$ | $n_{P,k}$ |
|---|---|---|---|---|
| 1 | 0 | -3.9893 | 0 | 1.2189 |
| 2 | $1.3638 \cdot 10^5$ | 2.6392 | 208.9518 | 1.4752 |
| 3 | $1.5512 \cdot 10^5$ | -0.4760 | $5.7672 \cdot 10^4$ | -2.5337 |
| 4 | $1.5577 \cdot 10^5$ | 3.7702 | $5.7318 \cdot 10^5$ | 1.3308 |
| 5 | $5.5196 \cdot 10^5$ | -3.1150 | $2.7411 \cdot 10^7$ | -0.7536 |
| 6 | $5.9880 \cdot 10^7$ | 3.2095 | $2.7413 \cdot 10^7$ | -0.8378 |
| 7 | $2.2118 \cdot 10^9$ | -2.2025 | $6.6900 \cdot 10^9$ | 0.2872 |

### 3.1.7 Comparison to Dedicated Design Code

To validate the Hiperco PMI metamodel and ferrite PMI metamodel, the predicted Pareto-optimal fronts from Hiperco and ferrite PMI metamodels are compared with the Pareto-optimal fronts from the dedicated design approach established in [7].

In the dedicated design magnetic analysis, the MMF source $F$ is expressed as $Ni$. An incremental current $\Delta i = \delta i_{pk}$ is applied on the MEC to test the incremental inductance. Similar to the normalized design, the MEC is evaluated four times to insure a required incremental inductance $L_{inc}$ at rated operating point and at zero current condition. The four MEC evaluations' MMF are

set as $N(i_{pk}+\Delta i/2)$, $N(i_{pk}-\Delta i/2)$, $N(\Delta i/2)$ and $N(-\Delta i/2)$, respectively. The result of the n$^{th}$ evaluation contains the PMI flux linkage $\lambda_n$ and the convergence index $e_n$. The inductance at rated operating point $L_{inc,r}$ is expressed as $L_{inc,r}=(\lambda_1-\lambda_2)/\Delta i$. The inductance at zero current condition $L_{inc,z}$ is expressed as $L_{inc,z}=(\lambda_3-\lambda_4)/\Delta i$.

Some of the constraints of the dedicated design are different from the constraints proposed in Section 3.1.4. Since the objective of the dedicated design approach is to determine the actual PMI geometry and the coil configuration, the number of turns $N$ and the conductor area $a_{cd}$ need to be selected. In the dedicated design approach, the peak current density $J$ is determined by $a_{cd}$ and $i_{pk}$. For a dedicated PMI design, it is necessary to limit $J$ from a thermal perspective. In the dedicated design approach, the packing factor is calculated based on the slot geometry, $N$, and $a_{cd}$. The packing factor is limited to insure a valid coil configuration. The inductance constraint is used in the dedicated design approach to insure the inductance satisfies the design requirement.

The first constraint is with regard to the packing factor. In particular,

$$c_1=\mathrm{ltn}\left(k_{pfd},k_{pfmx}\right) \tag{3.42}$$

where $k_{pfmx}$ is the maximum allowed packing factor which is set as 0.7 and $k_{pfd}$ is the calculated packing factor which is expressed as $k_{pfd}=a_{cd}N/(d_w w_w)$, where $a_{cd}$ is the conductor cross section area.

The second constraint is the current density constraint. In particular,

$$c_2=\mathrm{ltn}\left(J,J_{mx}\right) \tag{3.43}$$

where $J_{mx}$ is the maximum allowed current density which will be set to 7.5 A/mm$^2$ in the example studies and $J$ is the calculated current density which is expressed as $J = (i_{pk} + \Delta i/2)/a_{cd}$.

The third constraint is the MEC convergence constraint, which may be expressed as

$$c_3 = \text{mean}\left(e_1, e_2, e_3, e_4\right) \tag{3.44}$$

The forth and fifth constraints are the inductance constraints given by

$$c_4 = \text{gtn}\left(L_{inc,r}, L_{inc}\right) \tag{3.45}$$

$$c_5 = \text{gtn}\left(L_{inc,z}, L_{inc}\right) \tag{3.46}$$

The sixth constraint is to insure the PM is not demagnetized at the rated current. This is implemented as

$$c_6 = \text{gtn}\left(H_{pm}, 0.75H_{ci}\right) \tag{3.47}$$

where $H_{pm}$ can be calculated using (3.23) with flux $\Phi_{26,1}$ and dimension $w_i$ and $d$ at $i_{pk} + \Delta i/2$.

The fitness function of dedicated design is the same as the normalized design except that the normalized mass and normalized dc power loss are substituted with mass $M_{PMI}$ and dc power loss $P_{PMI}$.

With the dedicated design approach just introduced, the incremental inductance objective $L_{inc}$ is set as 2.6 mH and the rated operating current $i_{pk}$ is set as 20 A which lead to an energy metric of 0.52 J. The design space of the dedicated design is listed in Table 3.4. It can be noticed that in dedicated design space, the number of turns is selected as a design parameter instead of current density and there is an extra design parameter $a_{cd}$ for the conductor cross sectional area.

Table 3.8 PMI Dedicated Design Space

| Gene | Parameter | Min. | Max. | Encoding | Units |
|---|---|---|---|---|---|
| 1 | $g_c$ | 0.25 | 3 | Log | mm |
| 2 | $g_e$ | 1 | 5 | Log | mm |
| 3 | $d_s$ | 5 | 50 | Log | mm |
| 4 | $w_s$ | 5 | 50 | Log | mm |
| 5 | $r_{dws}$ | 0.1 | 0.9 | Lin | N/A |
| 6 | $r_{wws}$ | 0.1 | 0.9 | Lin | N/A |
| 7 | $w_i$ | 10 | 60 | Log | mm |
| 8 | $d$ | 30 | 300 | Log | mm |
| 9 | $r_{wei}$ | 0.5 | 1.5 | Lin | N/A |
| 10 | $r_{wci}$ | 0.5 | 1.5 | Lin | N/A |
| 11 | $r_{wbi}$ | 0.5 | 1.5 | Lin | N/A |
| 12 | $r_{wexe}$ | 0.1 | 1.0 | Lin | N/A |
| 13 | $N$ | 5 | 200 | Log | N/A |
| 14 | $a_{cd}$ | 1 | 100 | Log | $mm^2$ |
| 15 | $l_{pm}$ | 1 | 40 | Log | mm |
| 16 | $t_{pm}$ | 1 | 6 | Int | N/A |

The comparison between the detailed design code and metamodel results is shown in Fig. 3.12. In Fig. 3.12, “MEC PMI Designs” are detailed design results. Designs designated “LL” are against the lower current density limit. Designs designated “NL” are not against the current density limit. Designs designated “UL” are against the upper current density limit. The metamodel matches the region of Pareto-optimal front where is not current density limited. Note that there is no current density limit in the metamodel design.

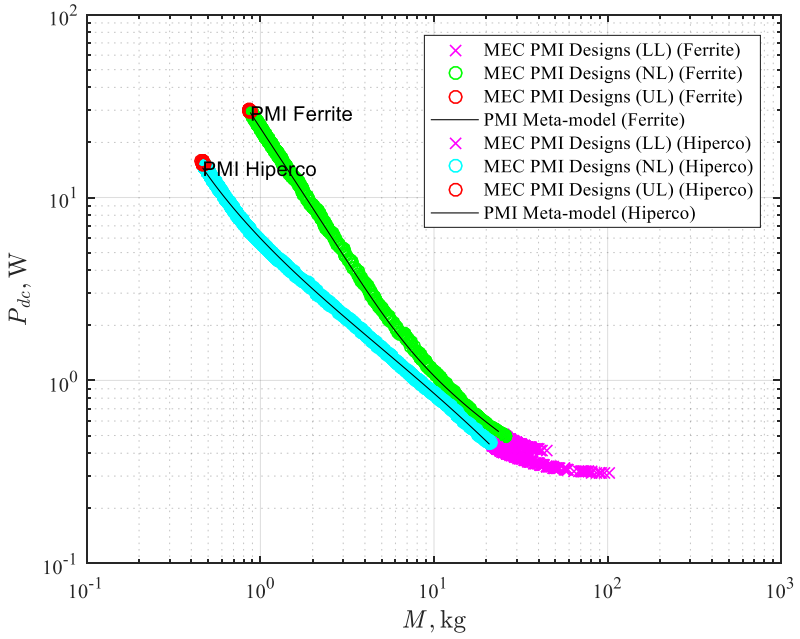


Fig. 3.12 Pareto-optimal front

It is necessary to include ac losses into the dedicated design since both the input PMI and output PMI experience current ripple. The PMI ac loss components are magnetic core eddy-current loss, permanent magnet eddy-current loss, conductor skin effect loss, and conductor proximity effect loss. The hysteresis loss in the magnetic core and the permanent magnet is assumed to be dominated by eddy-current loss. The PMI ac loss mechanisms are analyzed thoroughly in [7]. In [7], the PMI is used as the output LC filter inductor of a buck converter. The PMI current ripple in [7] is the triangular waveform shown in Fig. 2.1. Based on the current ripple waveform, the flux density in the magnetic core and permanent magnet is approximated as a triangular waveform which has a period $T$ and duty cycle $d$. The eddy-current loss density at the MEC $k^{th}$ branch is given by (10.1) from [7]. In particular,

$$P_{eddy,k} = \frac{\sigma_k}{32wd}\left(4k_1^4 + 8k_2k_1^3 + 2k_1^2k_2^2 - 2k_1k_2^3 + k_2^4\ln(1+\frac{2k_1}{k_2})\right)\frac{B_{pk,k}^2}{T^2}\left(\frac{1}{d(1-d)}\right) \tag{3.48}$$

where $\sigma_k$ is the magnetic core or the permanent magnet conductivity, $w$ and $d$ are the width and depth of the cross sectional area where eddy current flows, respectively, $k_1 = \min(w,d)$, $k_2 = |w-d|$, and $B_{pk,k}$ is the peak value of the flux density at MEC $k^{th}$ branch. The expression for $B_{pk,k}$ is given by (10.2) in [7]. The total eddy-current loss is calculated as

$$P_{eddy} = \sum_{k=1}^{26} P_{eddy,k} V_{core,k} \tag{3.49}$$

where $V_{core,k}$ is the volume of the $k^{th}$ branch.

The conductor skin effect loss is calculated as [7]

$$P_{cd,skn} = \sum_{k=1}^{n_h} i_{l,k}^2 r_{skn,k} \tag{3.50}$$

where $i_{l,k}$ is the rms amplitude of the PMI current $k^{th}$ order harmonics, $r_{skn,k}$ is the conductor ac resistance due to the skin effect, and $n_h$ is the number of harmonics considered. The harmonic current amplitude $i_{l,k}$ for the triangular current waveform is given by (6.15) in [7]. The $r_{skn,k}$ is given by (2.64) in [7].

The conductor proximity effect loss due to the current $k^{th}$ order harmonics is calculated as (10.17) from [7]. In particular,

$$P_{cd,prox,k} = 2\left(\frac{\hat{G}_k\left(\left\langle H_{hs,k}^2\right\rangle + \left\langle H_{vs,k}^2\right\rangle\right)}{\sigma_{cd}} d_c N_t + \frac{\hat{G}_k\left(\left\langle H_{hew,k}^2\right\rangle + \left\langle H_{vew,k}^2\right\rangle\right)}{\sigma_{cd}} w_c N_t\right) \tag{3.51}$$

where $\hat{G}_k$ is the proximity effect loss factor, $\langle \bullet \rangle$ is the spatial average function, $H_{hs,k}$, $H_{vs,k}$, $H_{hew,k}$, and $H_{vew,k}$ are the slot horizontal field intensity, slot vertical field intensity, end winding horizontal field intensity, and end winding vertical field intensity, respectively, $\sigma_{cd}$ is the conductor conductivity, $N_t$ is the number of turns, $d_c$ is the depth of the PMI, and $w_c$ is the width of the E core center leg. The proximity effect loss factor $\hat{G}_k$ is given by (2.36) from [7]. The expressions of $\langle H_{hs,k}^2 \rangle$, $\langle H_{vs,k}^2 \rangle$, $\langle H_{hew,k}^2 \rangle$, and $\langle H_{vew,k}^2 \rangle$ are given by (10.6), (10.9), (10.13), and (10.14) from [7], respectively. The total proximity loss is calculated as

$$P_{cd,prox} = \sum_{k=1}^{n_h} P_{cd,prox,k} \tag{3.52}$$

The PMI ac loss is calculated as

$$P_{ac} = P_{eddy} + P_{cd,skn} + P_{cd,prox} \tag{3.53}$$

The ac loss expressions (3.48) – (3.53) can be directly applied to the output PMI of the notional system since the output PMI sees the same triangular current ripple shape as [7].

The input PMI sees the current ripple introduced by the passive rectifier which is not a triangular waveform. Thus the ac loss expressions from [7] need to be modified. The current ripple spectrum of the input PMI is derived in Section 4.3. Given the current ripple harmonics magnitude and frequency, the conductor skin effect loss and proximity effect loss can be determined based on (3.50) – (3.52).

The fundamental component of the current ripple is extracted to approximate the magnetic core eddy-current loss and permanent magnet eddy-current loss. It is assumed that the fundamental

component of the current ripple produces a sinusoidal flux density in the magnetic core and permanent magnet. The $B_{pk,k}$ is calculated as

$$B_{pk,k} = \frac{B_k(i_{fund,max}) - B_k(i_{fund,min})}{2} \tag{3.54}$$

where $B_k(i_{fund,max})$ and $B_k(i_{fund,min})$ are the MEC $k^{th}$ branch flux density evaluated at $i_{fund,max}$ and $i_{fund,min}$, respectively. The $i_{fund,max}$ and $i_{fund,min}$ are calculated as

$$i_{fund,max} = \bar{i}_r + i_{r,1} \tag{3.55}$$

$$i_{fund,min} = \bar{i}_r - i_{r,1} \tag{3.56}$$

where $\bar{i}_r$ is the current dc component, and $i_{r,1}$ is the fundamental component of the current ripple. The eddy-current loss density at $k^{th}$ branch is determined based on (6.1-12) and (6.1-14) from [31] which is given by

$$P_{eddy,k} = \frac{\sigma_k}{256wd}\left(4k_1^4 + 8k_2k_1^3 + 2k_1^2k_2^2 - 2k_1k_2^3 + k_2^4\ln(1+\frac{2k_1}{k_2})\right)\omega_{r,1}^2 B_{pk,k}^2 \tag{3.57}$$

where $\omega_{r,1}$ is the current ripple fundamental component frequency. Since the input PMI is built with steel laminations, the depth $d$ of the magnetic core cross sectional area should be the lamination thickness. The total eddy-current loss is given as (3.49).

## 3.2 Polypropylene Capacitor Bank Model

The capacitors are also critical to the converter design. Because of the low effective series resistance, polypropylene capacitors are preferred for filtering at high frequencies. For the notional

system shown in Fig. 1.1, a polypropylene capacitor bank is applied to $C_{in}$ and $C_{outp}$. The capacitor bank is shown in Fig. 3.13 which contains $N_{parallel}$ parallel connected capacitors and $N_{series}$ series connected branches. The capacitors are selected from a capacitor family which has different capacitor rated voltage levels. The lowest rated voltage level is denoted as $V_{min}$ and the highest rated voltage level is denoted as $V_{max}$. There are different capacitance values at each rated voltage level. The smallest capacitance is denoted as $C_{min}$ and the largest capacitance is denoted as $C_{max}$. The first step of the capacitor bank construction is to determine the capacitor rated voltage level $v_{cap}$ and $N_{series}$ based on the capacitor bank rated voltage $v_{dc}$. The pseudo code of this step is given in Table 3.9. The next step is to determine the capacitor capacitance $C_n$ from the $v_{cap}$ capacitor family and $N_{parallel}$ based on the capacitor bank capacitance $C_{des}$ and $N_{series}$. The pseudo code of this step is given in Table 3.10.

Considering the voltage level of the notional dc generation system, the capacitor family from MKP1848C dc-link capacitor datasheet [33] is selected to construct the capacitor bank. The MKP1848C series capacitors contains the capacitor families that are rated at 500V, 600V, 800V, 900V, 1000V, and 1200V. The capacitance of each voltage level have a range that spans from 1 $\mu F$ to 500 $\mu F$.

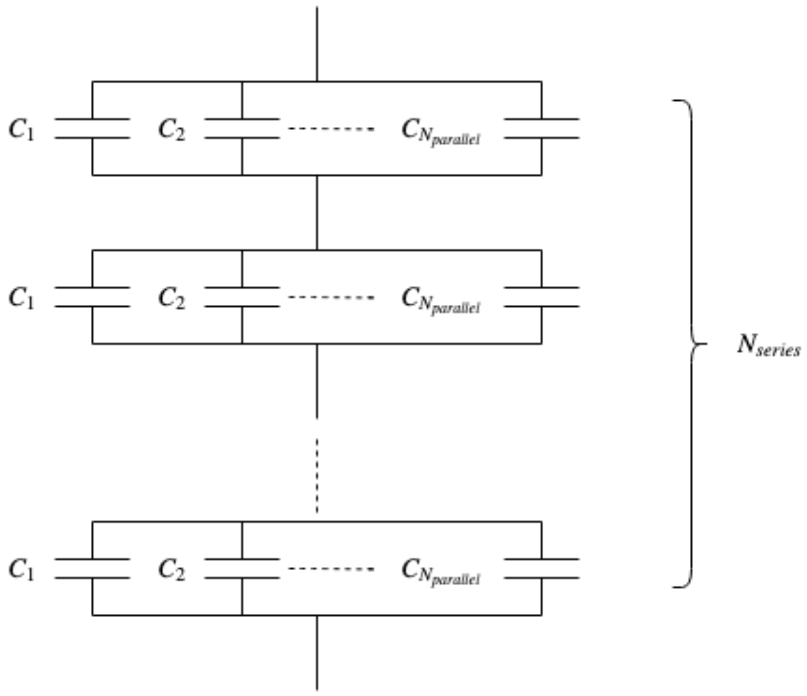


Fig. 3.13 Polypropylene Capacitor Bank

Table 3.9 Pseudo Code for $v_{cap}$ and $N_{series}$ Determination

1. Group the available capacitor rated voltage level as a vector
   $\mathbf{v}_{avai} = [V_{min} \cdots V_{max}]$
2. If ($v_{dc} \le V_{max}$)

   $v_{cap}$ is set as the first element of $\mathbf{v}_{avai}$ that is larger than or equal to $v_{dc}$.

   $N_{series} = 1$

   else

   $v_{cap} = V_{max}$

   $N_{series} = \text{ceil}\left(v_{dc} / v_{cap}\right)$ where $\text{ceil}(\bullet)$ is the ceiling function.

   end

Table 3.10 Pseudo Code for $C_n$ and $N_{parallel}$ Determination

1. Group the available capacitance from voltage level $v_{cap}$ capacitor family as a vector
   $\mathbf{C}_{vcap} = [C_{min} \cdots C_{max}]$
2. If ($C_{des} N_{series} \le C_{max}$)
   $C_1$ is set as the first element of $\mathbf{C}_{vcap}$ that is larger than or equal to $C_{des} N_{series}$.
   $N_{parallel} = 1$
   else
   $N_{parallel} = \text{ceil}\left( \frac{C_{des} N_{series}}{C_{max}} \right)$ where ceil(•) is the ceiling function.
   if (modulus of $C_{des} N_{series}$ over $C_{max}$ equals to 0)
   $C_1 = C_2 = \ldots = C_{N_{parallel}} = C_{max}$
   else
   $C_1 = C_2 = \ldots = C_{N_{parallel}-1} = C_{max}$
   $C_{N_{parallel}}$ is set as the first element of $\mathbf{C}_{vcap}$ that is larger than or equal to the modulus of $C_{des} N_{series}$ over $C_{max}$.
   end
   end

Next, the capacitor bank Equivalent Series Resistance (ESR), mass, and thermal coefficient are determined. The capacitor bank ESR $R_{esr}$ is calculated as

$$R_{esr} = N_{series} \left( \sum_{n=1}^{N_{parallel}} \frac{1}{R_{cn}} \right)^{-1} \tag{3.58}$$

where $R_{cn}$ is the ESR of capacitor $C_n$.

The capacitor bank mass $M_C$ is calculated as

$$M_C = N_{series}\left(\sum_{n=1}^{N_{parallel}} M_{cn}\right) \tag{3.59}$$

where $M_{cn}$ is the mass of capacitor $C_n$.

The capacitor bank thermal coefficient $\alpha$ is calculated using

$$\alpha_n = \frac{(R_{esr} / N_{series})^2}{R_{cn} G_{cn}} \tag{3.60}$$

$$\alpha = \max([\alpha_1 \ \alpha_2 \cdots \alpha_{N_{parallel}}]) \tag{3.61}$$

where $\alpha_n$ is capacitor $C_n$'s thermal coefficient, and $G_{cn}$ is capacitor $C_n$'s thermal conductance which has a unit of W/℃. For the notional system, $R_{cn}$, $M_{cn}$, and $G_{cn}$ are obtained from the MKP1848C catalogs [33].

Based on Table 3.9, Table 3.10, and (3.58) – (3.60), the polypropylene capacitor bank ESR, mass, and thermal coefficient are obtained from a capacitor catalog based function. The inputs of the catalog based function are $C_{des}$ and $v_{dc}$. The outputs of the function are capacitor bank ESR $R_{esr}$, capacitor bank mass $M_C$, capacitor bank thermal coefficient $\alpha$, number of series connected branch $N_{series}$, and number of parallel connected capacitors $N_{parallel}$.

The capacitor bank's Root Mean Square (RMS) current is limited since the RMS current will increase the capacitor temperature and reduce the capacitor lifetime. A maximum capacitor temperature rise $\Delta T_{max}$ is used to insure a desired capacitor lifetime. The capacitor temperature rise is calculated as

$$\Delta T = {I_{rms}}^2 \alpha \tag{3.62}$$

where $I_{rms}$ is the RMS current of the capacitor bank. For the MKP1848C capacitor family, the $\Delta T_{max}$ is set as 30 ℃ at room temperature [33].

## 3.3 Electrolytic Capacitor Model

The electrolytic capacitor models used herein are established in [7]. The electrolytic capacitor has a frequency derating property which causes the effective capacitance drop as the frequency increase. This effect has to be considered in the WBG based converter design since the switching frequency of WBG based converter is very high. The effective capacitor capacitance is expressed as [7]

$$C_{eff} = C\left(\alpha_c + \frac{1-\alpha_c}{1+\left(\frac{f_{sw}}{f_C}\right)^{n_C}}\right) \tag{3.63}$$

where $C_{eff}$ is the effective capacitance, $\alpha_c$, $f_C$ and $n_C$ are model parameters and $f_{sw}$ is the converter switching frequency.

The electrolytic capacitor ESR is required for the converter disturbance rejection analysis and ripple analysis. The ESR model is expressed as

$$R_{esr} = \frac{\gamma_C}{Cv_{c,rate}} \tag{3.64}$$

where $\gamma_C$ is the model parameter.

The electrolytic capacitor mass model is expressed as

$$M_C = \beta_C C v_{C,rate}^{3/2} \tag{3.65}$$

where $\beta_C$ is the model parameter. The electrolytic capacitor model parameters which will be used in the illustrated design study of Chapter 6 are listed in Table 3.11.

Similar to the polypropylene capacitor, the RMS current of the electrolytic capacitor is limited to ensure a proper lifetime. For the considered capacitor family [34], each capacitor has its RMS current limit which is listed in [34]. The smallest RMS current limit is 1.6 A. For the electrolytic capacitor used in the notional system, the maximum allowed RMS current $I_{coute,mx}$ is determined as 1.6 A to insure the capacitor RMS current is always under its limit given by [34]. In Chapter 6, a constraint is applied to limit the electrolytic capacitor RMS current.

Table 3.11 Electrolytic Capacitor Model Parameters [7]

| |
|---|
| $\alpha_C = 1.436 \cdot 10^{-19}$ |
| $f_C = 8746.2$ Hz |
| $n_C = 1.9255$ |
| $\beta_C = 3.3578 \cdot 10^{-2}$ kg/(F·V$^{3/2}$) |
| $\gamma_C = 2.694 \cdot 10^{-2}$ Ω·F·V |

# 4. UNCONTROLLED GENERATION SUBSYSTEM MODELS

One of the most important components of a dc generation system is the generator. A high-fidelity generator model is required to achieve an accurate system model. In this work, a symmetric Permanent Magnet Synchronous Machine (PMSM) is used as the generator. An analytical analysis approach is proposed in [31] to model the PMSM. The approach is modified herein to include the spatial winding harmonics and temporal current harmonics. In the dc generation system, a rectifier is required to convert the ac voltage to dc voltage. In this work, a passive rectifier is applied considering its low cost and robustness. The operation of passive rectifier will introduce significant harmonic components to the generator currents which makes it crucial to take the current harmonics into consideration when modeling the PMSM. A low pass LC filter is connected to the passive rectifier to suppress the dc current harmonics and stabilize the dc voltage. The PMSM, passive rectifier, and low pass filter formulate an uncontrolled dc generation system. In this chapter, the PMSM model is developed and validated in Section 4.1. The waveform reconstruction algorithm based passive rectifier model is established in Section 4.2. Section 4.3 introduces the low pass filter model. The last section explains the model dependency between the PMSM model, the passive rectifier model, and the low pass filter model.

## 4.1 PMSM Model

The analysis approach proposed in [31] has been applied to several permanent magnet machine design problems. In [35], the approach is applied to design a heterogeneous-pole permanent magnet machine. In [36], an asymmetric salient permanent magnet machine is designed based on this approach. In this section, the approach is modified to take winding and current

harmonics into consideration. The first step of the approach is to establish the PMSM geometry which is covered in Section 4.1.1. Second, the spatial winding harmonics are explored in Section 4.1.2. In Section 4.1.3, the machine's material properties are discussed. The machine radial field analysis is performed in Section 4.1.4. In Section 4.1.5, the machine lumped parameter model is established. The machine ferromagnetic portion field is analyzed in Section 4.1.6. The machine mass and loss calculation are implemented in Section 4.1.7 to finish the PMSM modelling. In Section 4.1.8, a Finite Element Model (FEM) is developed for a sample PMSM and the FEM results are compared with the analytically calculated results to validate the proposed model's accuracy. The cogging torque mechanism of the PMSM is analyzed in Section 4.1.9.

### 4.1.1 PMSM Geometry

The generator used in this work is a surface mount permanent magnet machine. The geometry of the machine is shown in Fig. 4.1. In Fig. 4.1, $\phi_{sm}$ denotes the mechanical position relative to the stator, $\phi_{rm}$ denotes the mechanical position relative to the rotor, and $\theta_{rm}$ denotes the mechanical rotor position. The machine electrical angles are defined as $P/2$ times the corresponding mechanical quantities, where $P$ is the number of poles. It can be shown that

$$\phi_s = \phi_r + \theta_r \tag{4.1}$$

where $\phi_s$ is the electrical position relative to stator, $\phi_r$ is the electrical position relative to rotor, and $\theta_r$ is the electrical rotor position. The rotor electrical speed $\omega_r$ is defined as $P/2$ times the corresponding rotor mechanical speed $\omega_{rm}$. The rotor position $\theta_r$ is given by

$$\theta_r = \omega_r t \tag{4.2}$$

where $t$ denotes time.

In Fig. 4.1, the inner most region is the rotor shaft which has the radius $r_{rs}$. The rotor magnetic inert region has a depth of $d_i$ and extends from radius $r_{rs}$ to $r_i$. The rotor backiron region has a depth of $d_{rb}$ and extends from radius $r_i$ to $r_{rb}$. The active rotor region contains the permanent magnet and magnetic inert space between magnets. The permanent magnet fraction, $\alpha_{pm}$, is defined as ratio of the angle spanned by one permanent magnet over the angle spanned by an entire pole. The active rotor region has a depth of $d_m$ and extends from radius $r_{rb}$ to $r_g$. The airgap region has a depth of $g$ and extends from radius $r_g$ to $r_{st}$. The active stator region contains the stator teeth and slots which has a depth of $d_{st}$ and extends from radius $r_{st}$ to $r_{sb}$. The stator tooth fraction, $\alpha_{st}$, is defined as ratio of the angle spanned by a stator tooth over the angle spanned by a slot and tooth, taken at $r_{st}$.The stator backiron region has a depth of $d_{sb}$ and extends from radius $r_{sb}$ to $r_{ss}$. The machine axial length $l$ is not shown in the figure. The PMSM geometry variables and their descriptions are listed in Table 4.1.

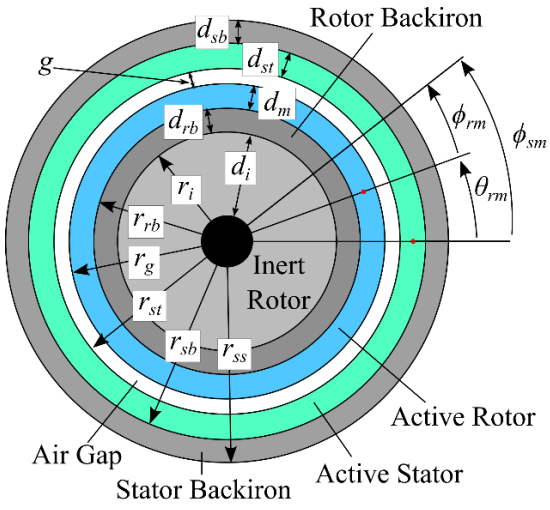


Fig. 4.1 Machine Geometry [37]

Table 4.1 PMSM Geometry Parameters

| Symbol | Description |
|---|---|
| $r_{rs}$ | Radius of rotor shaft |
| $r_i$ | Radius of rotor inert region |
| $r_{rb}$ | Radius of rotor backiron |
| $r_g$ | Radius of permanent magnet region |
| $r_{st}$ | Radius of stator teeth |
| $r_{sb}$ | Radius of stator backiron |
| $r_{ss}$ | Radius of stator shell |
| $d_i$ | Depth of inert region |
| $d_{rb}$ | Depth of rotor backiron |
| $d_m$ | Depth of permanent magnet region |
| $g$ | Depth of air gap |
| $d_{st}$ | Depth of stator teeth region |
| $d_{sb}$ | Depth of stator backiron |
| $\alpha_{pm}$ | Permanent magnet fraction |
| $\alpha_{st}$ | Stator tooth fraction |
| $l$ | Axial length |

### 4.1.2 Winding Function and Spatial Harmonics

To achieve a high-fidelity machine model, it is necessary to consider the stator MMF spatial harmonics introduced by the winding structure. The integral-slot distributed windings (ISDW) and fractional-slot concentrated windings (FSCW) are two common winding structures for machine construction. The FSCW structure tends to have more MMF spatial harmonics compared to ISDW but it has the advantage of reduced construction cost and shorter end winding

length. Spatial harmonics in PMSMs have been heavily studied in the literatures. In [38], the stator windings are skewed to reduce the spatial harmonics in a FSCW PMSM. In [39], the spatial harmonics of ISDW structure and FSCW structure are compared with respect to mitigating demagnetization vulnerability of surface mounted PMSMs. In this work, the spatial harmonics are analyzed using winding functions [40] to formulate a high fidelity stator MMF.

According to [40], the winding function quantifies how many times a winding links flux density at any given stator position. The *a*-, *b*-, and *c*-phase winding function can be grouped into a matrix as

$$\mathbf{W}_{abcs} = \begin{bmatrix} \mathbf{W}_{as} \\ \mathbf{W}_{bs} \\ \mathbf{W}_{cs} \end{bmatrix} \tag{4.3}$$

where $\mathbf{W}_{xs}$ is the *x*-phase discrete winding function [40]. The discrete winding function is transformed to the stator (not stationary) reference frame in which $\theta = \phi_s$. To this end, the transformation from three-phase variables to arbitrary reference frame variables can be expressed as [41]

$$\mathbf{f}_{qd0s} = \mathbf{K}_s \mathbf{f}_{abcs} \tag{4.4}$$

where

$$(\mathbf{f}_{qd0s})^T = [\, f_{qs} \quad f_{ds} \quad f_{0s} \,] \tag{4.5}$$

$$(\mathbf{f}_{abcs})^T = [\, f_{as} \quad f_{bs} \quad f_{cs} \,] \tag{4.6}$$

$$\mathbf{K}_s = \frac{2}{3}\begin{bmatrix} \cos\theta & \cos\left(\theta - \frac{2\pi}{3}\right) & \cos\left(\theta + \frac{2\pi}{3}\right) \\ \sin\theta & \sin\left(\theta - \frac{2\pi}{3}\right) & \sin\left(\theta + \frac{2\pi}{3}\right) \\ \frac{1}{2} & \frac{1}{2} & \frac{1}{2} \end{bmatrix} \tag{4.7}$$

and where $\mathbf{f}$ can represent either voltage, current, flux density, electrical charge, or winding function. The winding function in the stator reference frame is expressed as

$$\mathbf{W}_{qds}^{\phi_s} = \begin{bmatrix} W_{qs}^{\phi_s} \\ W_{ds}^{\phi_s} \end{bmatrix} = \mathbf{K}_{s,utr}^{\phi_s} \mathbf{W}_{abcs} \tag{4.8}$$

where $\mathbf{K}_{s,utr}^{\phi_s}$ denotes the upper two rows of $\mathbf{K}_s$ with $\theta = \phi_s$.

For the notional dc generation system, the $6n$ ( $n \in 1,2,3\ldots$ ) order winding spatial harmonics are extracted due to the symmetry of the three-phase passive rectifier and the symmetry of the machine. To this end, the winding function is decomposed into Fourier series as

$$W_{qs}^{\phi_s} = W_{q0}^{\phi_s} + \sum_{j=1}^{N_h} (W_{q,aj}^{\phi_s} \cos(6j\phi_s) + W_{q,bj}^{\phi_s} \sin(6j\phi_s)) \tag{4.9}$$

$$W_{ds}^{\phi_s} = W_{d0}^{\phi_s} + \sum_{j=1}^{N_h} (W_{d,aj}^{\phi_s} \cos(6j\phi_s) + W_{d,bj}^{\phi_s} \sin(6j\phi_s)) \tag{4.10}$$

where $W_{q0}^{\phi_s}$ and $W_{ds}^{\phi_s}$ are dc components, $N_h$ is the number of harmonics considered, $j$ is the harmonic order, and $W_{q,aj}^{\phi_s}$, $W_{q,bj}^{\phi_s}$, $W_{d,aj}^{\phi_s}$, and $W_{d,bj}^{\phi_s}$ are Fourier coefficients.

A 1-slot-per-pole-per-phase (1spp) ISDW configuration is applied to the PMSM of the notional system. This configuration will introduce more spatial harmonics than a 2-slot-per-pole-per-phase (2spp) configuration but since the passive rectifier introduces large temporal current

harmonics, the 1spp configuration is acceptable in this application. In addition, the 1spp configuration has simpler winding structure and is easier for prototype construction compared to 2spp configuration.

For the 1spp full pitch winding configuration, the discrete conductor distribution for each phase windings corresponding to a pole pair is

$$N_{as,P_p} = [0 \quad N \quad 0 \quad 0 \quad -N \quad 0] \tag{4.11}$$

$$N_{bs,P_p} = [-N \quad 0 \quad 0 \quad N \quad 0 \quad 0] \tag{4.12}$$

$$N_{cs,P_p} = [0 \quad 0 \quad -N \quad 0 \quad 0 \quad N] \tag{4.13}$$

where $N$ is the number of conductors in a slot.

The end conductor distribution for each of the phase windings is given by

$$M_{as,P_p} = \frac{N}{2}[-1 \quad -1 \quad 1 \quad 1 \quad 1 \quad -1] \tag{4.14}$$

$$M_{bs,P_p} = \frac{N}{2}[1 \quad -1 \quad -1 \quad -1 \quad 1 \quad 1] \tag{4.15}$$

$$M_{cs,P_p} = \frac{N}{2}[1 \quad 1 \quad 1 \quad -1 \quad -1 \quad -1] \tag{4.16}$$

With the conductor distribution established, the winding function is applied herein to analyze the spatial harmonics. Since the conductors are concentrated in the slot area, the discrete winding function is a series of steps. Each step spans one tooth and one slot, and is centered on the tooth. Although the stepped waveform approximates a sinusoid, spatial harmonics exist. For instance, the phase A winding function is shown in Fig. 4.2.

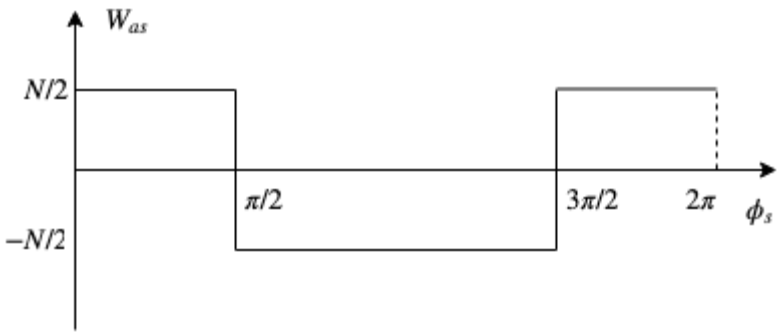


Fig. 4.2 Phase A Winding Function

From [40], the fundamental component of phase A winding function is expressed as

$$w_{as}(\phi_{sm}) = \frac{2N_{s1}^{*}}{P}\cos\left(\frac{P}{2}\phi_{sm}\right) \tag{4.17}$$

where $N_{s1}^{*}$ is the target amplitude of the fundamental conductor density component. By comparing the fundamental component of Fig. 4.2 and (4.17), $N$ can be calculated as

$$N = \text{round}(\frac{\pi N_{s1}^{*}}{P}) \tag{4.18}$$

where round(·) is a function rounds the result to the next nearest integer.

Due to the symmetry of the three-phase passive rectifier and the machine, the three-phase winding functions over sixty electrical degrees are required to analyze spatial winding harmonics. From [31], the discrete winding function over the first sixty electrical degrees is expressed as

$$W_{x,1} = \frac{1}{2}\sum_{j=1}^{S_s/P} N_{x,j} \tag{4.19}$$

$$W_{x,i+1} = W_{x,i} - N_{x,i} \tag{4.20}$$

where $i = 1 \cdots (S_{s,60} - 1)$, $S_{s,60} = S_s / 3P$, and $S_s$ is the number of slots of the PMSM. The variable $N_{x,i}$ denotes the number of conductors of phase *x* in $i^{th}$ slot where *x* is either *as*, *bs*, or *cs*. The variable $W_{x,i}$ denotes the number of times winding *x* links flux traveling through the $i^{th}$ tooth.

Next, the winding function is interpolated by

$$\mathbf{W}_{x,I} = \left[ W_{x,1} \text{ones}(1, N_{ppst}) \quad W_{x,2} \text{ones}(1, N_{ppst}) \ldots W_{x,S_{s,60}} \text{ones}(1, N_{ppst}) \right] \tag{4.21}$$

where $W_x$ is the discrete winding function given by (4.19) and (4.20) and $N_{ppst}$ is the number of interpolated positions for one slot-tooth span. Function ones(*x*,*y*) will return a *x* rows, *y* columns matrix and all the elements of this matrix is 1. The *a*-, *b*-, and *c*-phase interpolated winding function can be grouped into a matrix as

$$\mathbf{W}_{abcs,I} = \begin{bmatrix} \mathbf{W}_{as,I} \\ \mathbf{W}_{bs,I} \\ \mathbf{W}_{cs,I} \end{bmatrix} \tag{4.22}$$

With the discrete winging function established, (4.8)-(4.10) are used to calculate the $W_{q0}^{\phi_s}$, $W_{ds}^{\phi_s}$, $W_{q,aj}^{\phi_s}$, $W_{q,bj}^{\phi_s}$, $W_{d,aj}^{\phi_s}$, and $W_{d,bj}^{\phi_s}$ of the 1spp winding configuration.

### 4.1.3 Material Parameters

The material properties need to be considered to evaluate the machine performance. In Fig. 4.1, the rotor backiron region and the stator backiron region are made of silicon steel. The active rotor region contains the permanent magnets. The active stator region contains the winding conductors. The approach applied in [31] is used herein to formulate a stator material structure $\mathbf{S}$,

rotor material structure **R**, conductor material structure **C**, and permanent magnet material structure **M**. The fields of the material structures are given by

$$\mathbf{S} = \begin{bmatrix} \rho_s & B_{lim,s} & \mu_{r,s} & \alpha_{\mu,s} & \beta_{\mu,s} & \gamma_{\mu,s} & \alpha_s & \beta_s & k_{h,s} & k_{e,s} \end{bmatrix} \tag{4.23}$$

$$\mathbf{R} = \begin{bmatrix} \rho_r & B_{lim,r} & \mu_{r,r} & \alpha_{\mu,r} & \beta_{\mu,r} & \gamma_{\mu,r} \end{bmatrix} \tag{4.24}$$

$$\mathbf{C} = \begin{bmatrix} \rho_c & \sigma_c \end{bmatrix} \tag{4.25}$$

$$\mathbf{M} = \begin{bmatrix} \rho_{pm} & B_r & \chi_{pm} & H_{ci} \end{bmatrix} \tag{4.26}$$

where $\rho_x$ ($x \in ['s','r','c','pm']$) denotes the mass density of stator material, rotor material, conductor material, and permanent magnet material, $B_{lim,x}$ ($x \in ['s','r']$) is the flux density limit imposed on the stator and rotor steel to avoid saturation, $\mu_{r,x}$, $\alpha_{\mu,x}$, $\beta_{\mu,x}$, and $\gamma_{\mu,x}$ ($x \in ['s','r']$) are the permeability function [31] coefficients for the stator and rotor steel, $\alpha_s$, $\beta_s$, $k_{h,s}$, and $k_{e,s}$ denote the modified Steinmetz equation coefficients for the stator steel needed to calculate the core loss, $\sigma_c$ is the conductor conductivity, $B_r$ is the permanent magnet residual flux density, $\chi_{pm}$ is the permanent magnet susceptibility, and $H_{ci}$ is the permanent magnet intrinsic coercivity.

Listings of the material catalogs used in the notional system PMSM design can be found in the Appendix A.

### 4.1.4 Radial Field Analysis

The machine radial field analysis is performed in this section using an analytical field solution. Compared to the approach used in [35], the approach described herein includes the spatial

winding harmonics introduced in Section 4.1.2 and the temporal current harmonics which will be derived in Section 4.2. One of the key assumptions of the approach proposed in [35] is that the MMF drop across the rotor and stator backiron of the machine is negligible, which is to say that it is assumed that the most of the MMF drop occurs in the permanent magnet region, the air gap region, and the partially saturated stator teeth. Based on [35], the following equation is achieved

$$F_a(\phi_s) + F_{pm}(\phi_s) + F_{st}(\phi_s) = F_s(\phi_s) \tag{4.27}$$

where $F_a$ is the MMF drop across the air gap, $F_{pm}$ is the MMF drop across the permanent magnet region, $F_{st}$ is the MMF drop across the stator teeth, and $F_s$ is the stator MMF.

The stator MMF is expressed as

$$F_s(\theta_r, \phi_s) = \mathbf{i}_{\mathbf{abcs}}^{\mathbf{T}}(\theta_r)\mathbf{W}_{\mathbf{abcs}}(\phi_s) \tag{4.28}$$

Equation (4.28) can be transformed to *qd*-variables and combined with the winding harmonics derived in (4.9) and (4.10), whereupon $F_s$ can be expressed as

$$F_s(\theta_r, \phi_s) = \frac{3}{2}\left(\begin{array}{l} W_{qs}^{\phi_s}\left(i_{qs}^r(\theta_r)\cos(\phi_s - \theta_r) - i_{ds}^r(\theta_r)\sin(\phi_s - \theta_r)\right) \\ \qquad + W_{ds}^{\phi_s}\left(i_{qs}^r(\theta_r)\sin(\phi_s - \theta_r) + i_{ds}^r(\theta_r)\cos(\phi_s - \theta_r)\right) \end{array}\right) \tag{4.29}$$

In (4.29), $W_{qs}^{\phi_s}$ and $W_{ds}^{\phi_s}$ are the winding function in the stator reference frame, and $i_{qs}^r(\theta_r)$ and $i_{ds}^r(\theta_r)$ are the stator currents in the rotor reference frame. For the notional system, the *qd*-axis current exhibits large $6n$ ($n \in 1,2,3\ldots$) order harmonics due to the operation of the passive rectifier. The *qd*-axis currents are decomposed into Fourier series to include the temporal current harmonics which are given as

$$i_{qs}^{r} = i_{q0}^{r} + \sum_{j=1}^{N_{hc}} (i_{q,aj}^{r} \cos(6j\theta_r) + i_{q,bj}^{r} \sin(6j\theta_r)) \tag{4.30}$$

$$i_{ds}^{r} = i_{d0}^{r} + \sum_{j=1}^{N_{hc}} (i_{d,aj}^{r} \cos(6j\theta_r) + i_{d,bj}^{r} \sin(6j\theta_r)) \tag{4.31}$$

where $i_{q0}^{r}$ and $i_{d0}^{r}$ are the dc components, $N_{hc}$ is the number of harmonics considered, $j$ is the harmonic order, and $i_{q,aj}^{r}$, $i_{q,bj}^{r}$, $i_{d,aj}^{r}$, and $i_{d,bj}^{r}$ are Fourier coefficients. The derivation of $i_{qs}^{r}$ and $i_{ds}^{r}$ is given in Section 4.2.

Another assumption of the radial field analysis approach is that the radial component of the magnetic field in the air gap varies inversely with radius. The flux density in the air gap and permanent magnet region is expressed as [35]

$$B(r, \phi_s, \theta_r) = \frac{r_{rb}}{r} B_{st}(\phi_s, \theta_r) \quad r_{rb} \le r \le r_{st} \tag{4.32}$$

where $B_{st}$ is the flux density at the top of the stator teeth. The quantity $B_{st}$ is achieved by solving the following implicit equation using Newton-Ralphson solver [35].

$$B_{st}(\phi_s, \theta_r) = \frac{F_s(\theta_r, \phi_s) + F_m(\phi_r) - \frac{d_{st}}{2}\left[\frac{B_{utl}}{\mu_B(B_{ut}(\phi_s))} + \frac{B_{ltl}}{\mu_B(B_{lt}(\phi_s))}\right]}{R_m(\phi_r) + R_g(\phi_r) + \frac{cd_{st}}{2}\left[\frac{1}{\mu_B(B_{ut}(\phi_s))} + \frac{1}{\mu_B(B_{lt}(\phi_s))}\right]} \tag{4.33}$$

In (4.33), $F_m$ and $R_m$ are parameters associated with the permanent magnet, $R_g$ is the air gap quasi-reluctance, $c$ is the concentration factor used to represent the convergence of the flux into the steel of the tooth, $B_{utl}$ is the upper tooth leakage flux density, $B_{ut}$ is the flux density at the top of the stator tooth, $B_{ltl}$ is the lower tooth leakage flux density, $B_{lt}$ is the flux density at the bottom

of the stator tooth, and $\mu_B$ is the steel permeability as a function of flux density. The expressions of $F_m$ and $R_m$ are given in [31]. The expressions of $R_g$, $c$, $B_{utl}$, $B_{ut}$, $B_{ltl}$, and $B_{lt}$ can be found in [35].

### 4.1.5 Lumped Parameter Model

To analyze the generator-rectifier system, it is convenient to use the lumped parameter model of the machine. In particular, expressions of the stator resistance $r_s$, the stator *q*- and *d*-axis inductances $L_q$ and $L_d$, and the flux linkage due to the permanent magnets $\lambda_m'$ need to be derived. The approach used in [35] is applied herein to calculate these parameters. This dissertation will focus on the ferromagnetic field analysis set forth in the next section.

### 4.1.6 Ferromagnetic Field Analysis

The fields in the ferromagnetic portions of the machine are analyzed in this section to facilitate ensuring the steel is not overly saturated, the permanent magnets are not demagnetized, and to calculate the machine core loss. The basic analysis approach is set forth in [31], but it is heavily modified herein to improve the model fidelity in the presence of spatial winding and temporal current harmonics.

The ferromagnetic portions of the machine contain the stator teeth, stator backiron, rotor backiron, and the permanent magnets. The first step is to obtain the flux density of the stator teeth. In [31], the rotor is rotated over a sector of the machine consisting one slot and one tooth. Then the flux density waveform of the first stator tooth is synthesized using knowledge of flux density

of the first pole pair span of stator teeth over the aforementioned partial rotation of the rotor. This approach works for a distributed winding, inverter-fed motor design process. With a properly designed distributed winding, the spatial harmonics can be neglected. With appropriate inverter control, the phase current only contains switching frequency harmonics. Under these conditions the field waveforms in each tooth are identical except for a phase shift. In the generator-passive rectifier operation considered herein, the phase current contains large $6n$ ($n \in 1,2,3\ldots$) order harmonics and thus the stator teeth flux density analysis approach needs to be modified.

Due to the $6n$ order harmonics, the rotor is rotated sixty electrical degrees herein instead of one slot/tooth span. The corresponding mechanical rotor position vector $\boldsymbol{\theta}_{rm60}$ is expressed as

$$\boldsymbol{\theta}_{rm60,j} = -\frac{\pi}{S_s} + \frac{2\pi}{3P}\frac{j-1}{J} \qquad j \in [1\ldots J] \tag{4.34}$$

where $j$ is the rotor position index and $J$ is the number of positions considered.

Next, it is convenient to divide the stator teeth into mutually exclusive sets each spanning sixty electrical degrees of stator position. The flux density waveform on each set is identical to that of every other set except for a rotor position phase shift. Thus it is necessary to analyze the stator teeth waveforms in one set. The number of the stator teeth considered is expressed as

$$N_{t60} = \frac{S_s}{3P} \tag{4.35}$$

The next step is to determine the flux in the $i^{\text{th}}$ tooth with $B_{st}(\phi_{sm}, \theta_{rm})$ derived in Section 4.1.4. The $i^{\text{th}}$ tooth and its adjacent teeth are shown in Fig. 4.3 where $\phi_{ss,i}$ is the position of the

center of the $i^{th}$ tooth, $\phi_A$, $\phi_B$, $\phi_C$, and $\phi_D$ are the position of the vertex of the $(i-1)^{th}$ tooth, the $i^{th}$ tooth, and the $(i+1)^{th}$ tooth, respectively. The $\phi_A$, $\phi_B$, $\phi_C$, and $\phi_D$ are calculated as

$$\phi_A = \phi_{ss,i} + 2\pi / S_s(\alpha_{st} / 2 - 1) \tag{4.36}$$

$$\phi_B = \phi_{ss,i} - \pi / S_s \alpha_{st} \tag{4.37}$$

$$\phi_C = \phi_{ss,i} + \pi / S_s \alpha_{st} \tag{4.38}$$

$$\phi_D = \phi_{ss,i} + 2\pi / S_s(1 - \alpha_{st} / 2) \tag{4.39}$$

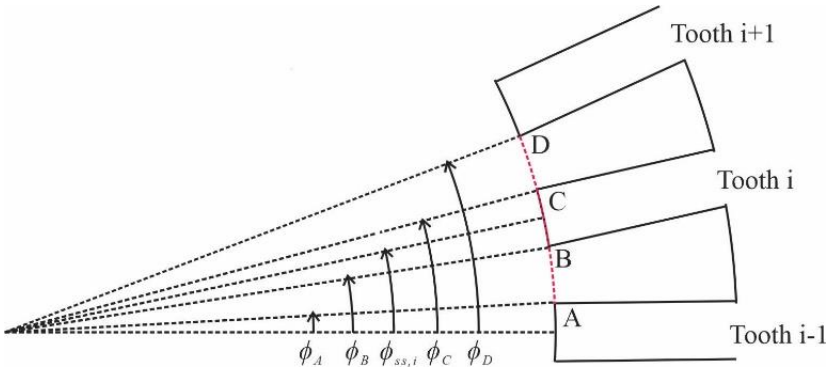


Fig. 4.3 The $i^{th}$ Tooth Flux Calculation

The flux in the $i^{th}$ tooth $\Phi_{t,i}$ is calculated by integrating the flux along curve AD in Fig. 4.3 with the weighting function $w_{AB}$ and $w_{CD}$ applied to flux along curve AB and curve CD, respectively. In particular,

$$\Phi_{t,i}(\theta_{rm}) = r_{st} l \left[ \begin{array}{l} \int_{\phi_A}^{\phi_B} B_{st}(\phi_{sm}, \theta_{rm}) w_{AB}(\phi_{sm}) d\phi_{sm} + \int_{\phi_B}^{\phi_C} B_{st}(\phi_{sm}, \theta_{rm}) d\phi_{sm} \\ + \int_{\phi_C}^{\phi_D} B_{st}(\phi_{sm}, \theta_{rm}) w_{CD}(\phi_{sm}) d\phi_{sm} \end{array} \right] \tag{4.40}$$

where

$$w_{AB}(\phi_{sm}) = \frac{\phi_{sm} - \phi_A}{\phi_B - \phi_A} \tag{4.41}$$

$$w_{CD}(\phi_{sm}) = \frac{\phi_{sm} - \phi_D}{\phi_C - \phi_D} \tag{4.42}$$

Compared to the integration approach used in [35] which integrates $B_{st}$ from the midpoint of arc AB to the midpoint of arc CD, (4.40) conserves the total flux into the stator while avoids the discontinuity in the stator field waveforms.

The tooth flux in the teeth spanning one pole pair is denoted as

$$\mathbf{\Phi}_{ts,i:j} = \mathbf{\Phi}_{t,i}(\boldsymbol{\theta}_{rm60,j}) \quad i \in [1 \ldots S_s 2/P], \quad j \in [1 \ldots J] \tag{4.43}$$

Due to the operation of the passive rectifier and the symmetry of the PMSM, when the rotor rotates sixty electrical degrees, the flux density waveform in a given tooth is identical to that of a tooth sixty electrical degrees away. Based on this fact, the following relationship can be obtained

$$\mathbf{\Phi}_{t,i}(\boldsymbol{\theta}_{rm}) = \mathbf{\Phi}_{t,i+N_{t60}}\left(\boldsymbol{\theta}_{rm} + \frac{2\pi}{3P}\right) \tag{4.44}$$

Using (4.43) and (4.44), the flux density waveform of the stator teeth in the first sixty electrical degrees over a rotational cycle of rotor positions can be synthesized using

$$\mathbf{\Phi}_{tpc,j+J(n-1)} = \mathbf{\Phi}_{ts:\mathrm{mod}(S_s+(1-n)N_{t60},S_s)+p,j} \quad p \in [1 \ldots N_{t60}], \quad n \in [1 \ldots 6], \quad j \in [1 \ldots J] \tag{4.45}$$

where $p$ is the tooth index spanned the first sixty electrical degrees, $n$ represents the $n^{th}$ sixty electrical degrees span, and $\mathrm{mod}(a,b)$ is a function which will return the modulus of $a/b$. The

first step of the synthetization is to find the $\mathbf{\Phi}_{ts}$ matrix based on (4.43) with $i = (S_s - \frac{2S_s}{P} + N_{t60}) \ldots N_{t60}$. Then the $\mathbf{\Phi}_{ts}$ is applied to (4.45) to achieve $\mathbf{\Phi}_{tpc}$.

The elements in $\mathbf{\Phi}_{tpc}$ correspond to mechanical rotor positions over a cycle given by

$$\boldsymbol{\theta}_{rmc,\, j+J(n-1)} = \boldsymbol{\theta}_{rm60,\, j} + \frac{2\pi}{3P}(n-1) \quad n \in [1 \ldots 6], \quad j \in [1 \ldots J] \tag{4.46}$$

The flux density of the stator teeth spanned the first sixty electrical degrees over a rotational cycle of rotor positions can be expressed as

$$\mathbf{B}_{tpc} = \frac{\mathbf{\Phi}_{tpc}}{w_{tb} l} \tag{4.47}$$

where $w_{tb}$ is the width of the tooth base which can be calculated based on the expression given in [35]. The maximum of stator tooth flux density is expressed as

$$B_{stmx} = \left\| \mathbf{B}_{tpc} \right\|_{\max} \tag{4.48}$$

where $\left\| \bullet \right\|_{\max}$ returns the greatest absolute value of the element of its matrix or vector argument.

The next step is to determine the flux density of the stator backiron. According to [31], the stator backiron flux vector can be related to the stator tooth flux vector using

$$\mathbf{\Phi}_{b,i}(\theta_{rm}) = \mathbf{\Phi}_{b,i-1}(\theta_{rm}) + \mathbf{\Phi}_{t,i}(\theta_{rm}) \tag{4.49}$$

where

$$\mathbf{\Phi}_{b,S_s}(\theta_{rm}) = -\frac{1}{2} \sum_{n=1}^{S_s/P} \mathbf{\Phi}_{t,n}(\theta_{rm}) \tag{4.50}$$

and where $\mathbf{\Phi}_{b,i}$ denotes the flux in backiron segment *i*.

With (4.49) and (4.50), a matrix of stator backiron segment fluxes $\mathbf{\Phi}_{bs}$ can be established using

$$\mathbf{\Phi}_{bs,i:j} = \mathbf{\Phi}_{b,i}(\boldsymbol{\theta}_{rm60,j}) \quad i \in [1 \ldots S_s 2/P], \quad j \in [1 \ldots J] \tag{4.51}$$

Similar to the stator teeth flux density waveform, when the rotor rotates sixty electrical degrees, the stator backiron segments separated by sixty electrical degrees have identical flux density waveforms, albeit phase shifted. Thus the stator backiron segment fluxes spanned the first sixty electrical degrees over a rotational cycle of rotor positions can be synthesized using

$$\mathbf{\Phi}_{bpc,j+J(n-1)} = \mathbf{\Phi}_{bs:\mathrm{mod}(S_s+(1-n)N_{t60},S_s)+p,j} \quad p \in [1 \ldots N_{t60}], \quad n \in [1 \ldots 6], \quad j \in [1 \ldots J] \tag{4.52}$$

Then the flux density in backiron segments spanned the first sixty degrees is calculated as

$$\mathbf{B}_{bpc} = \frac{\mathbf{\Phi}_{bpc}}{d_{sb} l} \tag{4.53}$$

and the maximum of stator backiron flux density is expressed as

$$B_{sbmx} = \left\| \mathbf{B}_{bpc} \right\|_{\max} \tag{4.54}$$

With the stator teeth flux density and stator backiron flux density, the rotor peak tangential flux density $B_{rbtmx}$, the rotor peak radial flux density $B_{rbrmx}$, and the permanent magnet minimum field intensity $H_{mn}$ can be obtained using the approach described in [31].

At this point, the following array of results can be obtained

$$\mathbf{F} = \left[ \mathbf{B}_{tpc} \ \mathbf{B}_{bpc} \ B_{stmx} \ B_{sbmx} \ B_{rbrmx} \ B_{rbtmx} \ H_{mn} \right] \tag{4.55}$$

### 4.1.7 PMSM Mass and Loss Calculation

The PMSM mass considered herein is the electromagnetic mass which is calculated as

$$M_G = V_s\rho_s + V_{rb}\rho_r + V_{pm}\rho_{pm} + 3V_{cd}\rho_{cd} \tag{4.56}$$

where $V_s$ is the stator steel volume, $V_{rb}$ is the rotor backiron volume, $V_{pm}$ is the permanent magnet volume, and $V_{cd}$ is the volume of stator conductor per phase. The expressions of $V_s$, $V_{rb}$, $V_{pm}$, and $V_{cd}$ are given as (9.3-25), (9.3-26), (9.3-28), and (9.4-17) in [31], respectively.

The PMSM loss includes the conductor dc loss $P_{cd,dc}$, conductor ac loss $P_{cd,prox}$, and stator core loss $P_c$. The conductor dc loss $P_{cd,dc}$ is calculated as

$$r_s = \frac{V_{cd}}{a_c^2\sigma_c} \tag{4.57}$$

$$I_{s,rms} = \mathrm{rms}\left(i_{as}(\theta_r)\right) \tag{4.58}$$

$$P_{cd,dc} = 3r_s I_{s,rms}^2 \tag{4.59}$$

where $r_s$ is the single phase winding resistance, $a_c$ is the conductor cross sectional area, $\mathrm{rms}(\bullet)$ is a function which returns the rms value of its argument, and $i_{as}(\theta_r)$ is the instantaneous *a*-phase current waveform obtained from Section 4.2.

The conductor ac loss includes the skin effect loss and proximity effect loss. In rotating machines, the skin effect loss is often negligible assuming appropriately sized conductors. Since the proximity effect loss is frequency dependent, it is necessary to derive the phase current spectrum first. With Fourier coefficients of the *qd*-axis current given in (4.30) and (4.31), the *qd*-axis current harmonics are given by

$$A_{q,j} = \sqrt{{i_{q,aj}^r}^2 + {i_{q,bj}^r}^2} \tag{4.60}$$

$$A_{d,j} = \sqrt{{i_{d,aj}^r}^2 + {i_{d,bj}^r}^2} \tag{4.61}$$

$$\theta_{q,j} = \text{angle}\left(i_{q,aj}^r + j i_{q,bj}^r\right) \tag{4.62}$$

$$\theta_{d,j} = \text{angle}\left(i_{d,aj}^r + j i_{d,bj}^r\right) \tag{4.63}$$

$$I_{q,j} = A_{q,j}\cos\left(6j\theta_r - \theta_{q,j}\right) \quad j = 1\ldots N_{hc} \tag{4.64}$$

$$I_{d,j} = A_{d,j}\cos\left(6j\theta_r - \theta_{d,j}\right) \quad j = 1\ldots N_{hc} \tag{4.65}$$

where $\text{angle}(\bullet)$ is a function which returns the phase angle of its complex valued argument.

The phase current harmonics are obtained by

$$I_{abc,j} = \begin{bmatrix} \cos\theta_r & \sin\theta_r \\ \cos\left(\theta_r - \frac{2\pi}{3}\right) & \sin\left(\theta_r - \frac{2\pi}{3}\right) \\ \cos\left(\theta_r + \frac{2\pi}{3}\right) & \sin\left(\theta_r + \frac{2\pi}{3}\right) \end{bmatrix} \begin{bmatrix} I_{q,j} \\ I_{d,j} \end{bmatrix} \tag{4.66}$$

The *a*-phase current harmonics are calculated as

$$I_{a,j} = A_{a,6j-1}\cos\left(-(6j-1)\theta_r + \arctan\left(\theta_{a,6j-1}\right)\right) + A_{a,6j+1}\cos\left((6j+1)\theta_r + \arctan\left(\theta_{a,6j+1}\right)\right) \tag{4.67}$$

where

$$A_{a,6j-1} = \sqrt{\frac{1}{4}A_{q,j}^2 + \frac{1}{4}A_{d,j}^2 + \frac{1}{2}A_{q,j}A_{d,j}\sin(\theta_{d,j} - \theta_{q,j})} \tag{4.68}$$

$$A_{a,6j+1} = \sqrt{\frac{1}{4}A_{q,j}^2 + \frac{1}{4}A_{d,j}^2 + \frac{1}{2}A_{q,j}A_{d,j}\sin(\theta_{q,j} - \theta_{d,j})} \tag{4.69}$$

$$\theta_{a,6j-1} = \frac{A_{q,j}\sin\theta_{q,j} - A_{d,j}\cos\theta_{d,j}}{A_{q,j}\cos\theta_{q,j} + A_{d,j}\sin\theta_{d,j}} \tag{4.70}$$

$$\theta_{a,6j+1} = \frac{A_{q,j}\sin\theta_{q,j} + A_{d,j}\cos\theta_{d,j}}{A_{d,j}\sin\theta_{d,j} - A_{q,j}\cos\theta_{q,j}} \tag{4.71}$$

With the phase current spectrum established, the proximity effect loss expression from [31] is used here. In particular, $P_{cd,prox}$ is calculated as

$$I_{s,0} = \sqrt{i_{q0}^{r\ 2} + i_{d0}^{r\ 2}} / \sqrt{2} \tag{4.72}$$

$$P_{cd,prox,0} = \frac{\pi\sigma_c l r_c^4 \omega_r^2 \mu_0^2 S_s}{12 w_{siR}^2} I_{s,0}^2 \left(\left|N_{as,1}\right| + \left|N_{bs,1}\right|\right)\left(N_{as,1}^2 - N_{as,1}N_{bs,1} + N_{bs,1}^2\right) \tag{4.73}$$

$$P_{cd,prox,6j\pm1} = \frac{\pi\sigma_c l r_c^4 ((6j\pm1)\omega_r)^2 \mu_0^2 S_s}{12 w_{siR}^2} \frac{A_{a,6j\pm1}^2}{2}\left(\left|N_{as,1}\right| + \left|N_{bs,1}\right|\right)\left(N_{as,1}^2 - N_{as,1}N_{bs,1} + N_{bs,1}^2\right) \tag{4.74}$$

$$P_{cd,prox} = P_{cd,prox,0} + \sum_{j=1}^{N_{hc}} P_{cd,prox,6j\pm1} \tag{4.75}$$

where $r_c$ is the conductor radius, $\mu_0$ is the vacuum permeability, and $w_{siR}$ is the width of the rectangularized slot [31].

With the stator teeth and stator backiron field waveforms established in Section 4.1.6, the approach used in [35] is applied herein to calculate the stator core loss $P_c$. The rotor core loss is neglected since the rotor backiron does not see significant flux density variations. The total loss of the PMSM is calculated as

$$P_G = P_{cd,dc} + P_{cd,prox} + P_c \tag{4.76}$$

### 4.1.8 Model Validation

To validate the analytical model derived in Section 4.1.1-Section 4.1.6, a surface mount PMSM as described in Section 4.1.1 is considered as the generator of a 10 kW generator-passive rectifier system. The PMSM's geometry, materials, winding configuration, and *qd*-axis currents are listed in Table 4.2. In Table 4.2, $i_{q0}^{r}$, $i_{q,a}^{r}$, $i_{q,b}^{r}$, $i_{d0}^{r}$, $i_{d,a}^{r}$, and $i_{d,b}^{r}$ are obtained based on (4.30) and (4.31).

Table 4.2 PMSM Specifications

| Description | Symbol | Value |
|---|---|---|
| Number of poles | $P$ | 14 |
| Rotor shaft radius | $r_{rs}$ | 1 cm |
| Rotor inert region radius | $r_i$ | 5.62 cm |
| Rotor backiron radius | $r_{rb}$ | 6.15 cm |
| Rotor permanent magnet radius | $r_g$ | 6.39 cm |
| Stator teeth radius | $r_{st}$ | 6.52 cm |
| Stator backiron radius | $r_{sb}$ | 7.64 cm |
| Stator shell radius | $r_{ss}$ | 8.15 cm |
| Tooth fraction | $\alpha_{st}$ | 0.5082 |
| Permanent magnet fraction | $\alpha_{pm}$ | 0.6828 |
| Active length | $l$ | 5.04 cm |
| Stator slots | $S_s$ | 42 |
| Mechanical rotor speed | $\omega_{rm}$ | 9000 RPM |
| Stator material | $m_s$ | JFE 10JNEX900 |
| Rotor material | $m_r$ | JFE 10JNEX900 |
| Conductor material | $m_c$ | Copper |
| Permanent magnet type | $t_{pm}$ | Sm2Co17-R30S |
| Fundamental conductor density | $N_{s1}$ | 120.1264 cond/rad |
| A phase winding pattern (1 pole) | $N_{as}$ | [0, 27, 0] |
| $Q$-axis fundamental current | $i_{q0}^r$ | -8.44 A |
| $Q$-axis current Fourier coefficients | $i_{q,a}^r$ | [0.125, -0.0781, -0.0136, 0.0284, -0.0351, 0.0260, -0.0188, 0.0109, -0.0042 , -0.0011] A |
| $Q$-axis current Fourier coefficients | $i_{q,b}^r$ | [1.10, -0.240, 0.106, -0.0521, 0.022, -0.0044, -0.0057, 0.0103, -0.0113, 0.0097] A |
| $D$-axis fundamental current | $i_{d0}^r$ | -3.57 A |
| $D$-axis current Fourier coefficients | $i_{d,a}^r$ | [-1.46, 0.207, -0.0208, -0.0283, 0.0405, -0.0369, 0.028, -0.0171, 0.0073, 0.000716] A |
| $D$-axis current Fourier coefficients | $i_{d,b}^r$ | [-1.41, 0.230, -0.172, 0.0743, -0.0421, 0.0086, 0.0040, -0.0144, 0.0152, -0.0146] A |

The derived analytical model is applied to the machine to predict the torque and field waveforms. Then the analytical results are compared with the results from a Finite Element Model (FEM) to verify the analytical model's accuracy. A transient 2D FEM of a single pole of the PMSM is created in Ansys Maxwell [42], as seen in Fig. 4.4. In the FEM, the JFE steel is modeled based on a magnetically non-linear model from [43]. The permanent magnet is assumed to have a

constant permeability. The rotor inert region is assumed to be vacuum. The FEM is evaluated over a full electrical cycle with 61 time steps. As it is pointed out in the previous section, for the PMSM-passive rectifier application, it is only necessary to analyze the fields over sixty electrical degrees. For the PMSM considered, sixty electrical degrees contains one stator tooth and one stator backiron segment. Thus in the FEM, one stator tooth and one stator backiron segments are selected for investigation. In Fig. 4.4, stator tooth and stator backiron segment are labeled. The stator tooth consists a positive half tooth and negative half tooth due to the 180 electrical degrees phase shift. The flux densities along the grey lines are integrated to calculate the fluxes of the stator tooth and stator backiron segment, respectively. Then the fluxes are divided by the cross sectional area along the grey lines to achieve the flux density in stator tooth and stator backiron segment.

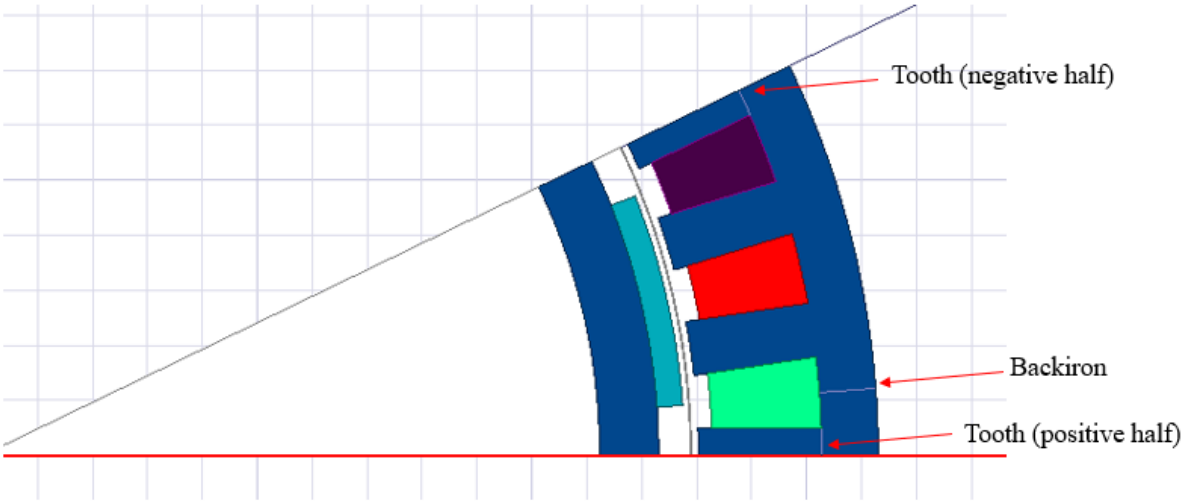


Fig. 4.4 Maxwell 2D Finite Element Model

The stator tooth and stator backiron flux densities calculated from the analytical model and FEM are compared in Fig. 4.5. The flux density waveforms agree well between analytical model and FEM.

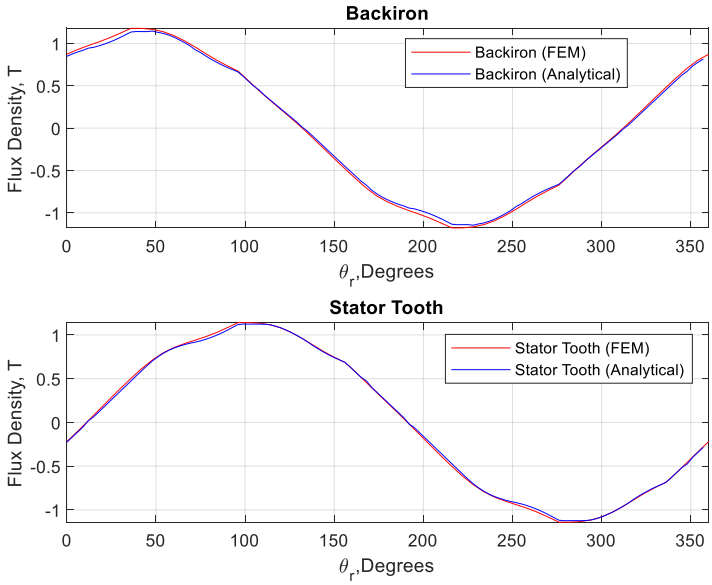


Fig. 4.5 Comparison of Stator Flux Densities between Analytical Model and FEM

The torque calculated from FEM is given in Fig. 4.6. One of the shortcomings of the analytical model is that it does not predict the torque ripple. The average value of the FEM calculated torque $T_{e,FEM}$ = -10.46 N and analytically calculated torque $T_{e,analytical}$ = -10.79 N are indicated on the figure. The FEM predicts a smaller magnitude of torque than the analytical model since the FEM considers the MMF drop in all parts of the machine. The percent difference is calculated as

$$\%_{diff} = 100\left|\frac{T_{e,analytical} - T_{e,FEM}}{T_{e,FEM}}\right|\% \tag{4.77}$$

The percent difference in torque estimate is 3% between the analytical model and the FEM. By comparing the stator flux density waveforms and average torque, the analytical model agrees well with FEM and thus the model is validated.

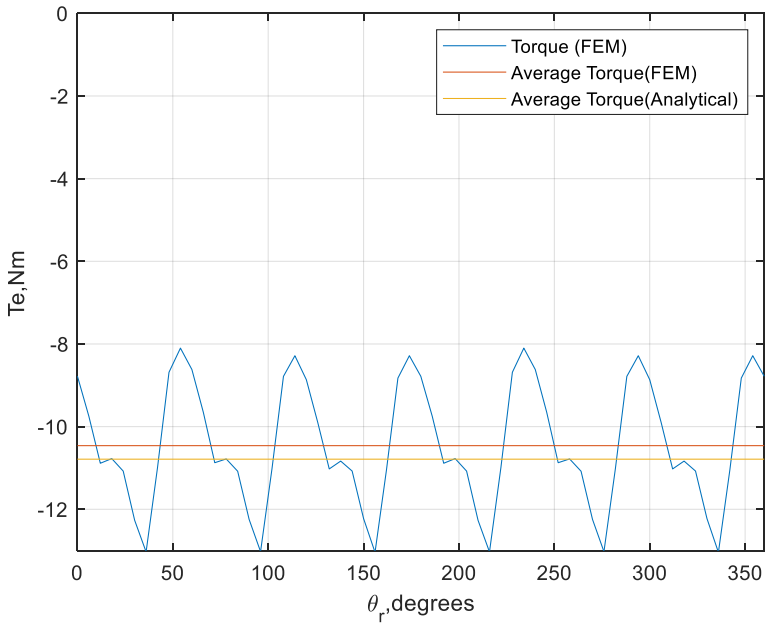


Fig. 4.6 FEM Electromagnetic Torque

### 4.1.9 Cogging Torque Evaluation

Another important PMSM design criteria is the torque ripple performance. Cogging torque is one of the sources of the torque ripple which is generated due to the interaction between rotor magnets and the slotting on stator. Due to the 1spp configuration applied in this work, the cogging torque has to be considered and limited.

In [44], six analytical models are presented to predict the cogging torque of PMSM. The analytical model results are compared to FEM in terms of cogging torque waveform and the optimal value of permanent magnet span ratio for cogging torque minimization. Considering the model accuracy and model computational efficiency, the model III [44] is applied herein to calculate the cogging torque.

In model III, the cogging torque $T_{cog}$ is calculated from the energy variation with the angle of rotation which can be written as

$$T_{cog}(\theta_{rm}) = \frac{\partial W_{airgap}(\theta_{rm})}{\partial \theta_{rm}} = \frac{\partial}{\partial \theta_{rm}}[\frac{1}{2\mu_0}\int_V G^2(\phi_{sm})B^2(\phi_{sm},\theta_{rm})dV] \tag{4.78}$$

where $W_{airgap}$ is the magnetic energy in the airgap, $\mu_0$ is the air permeability, $G(\phi_{sm})$ is the airgap relative permeance, and $B(\phi_{sm},\theta_{rm})$ is the airgap flux density in an equivalent slotless machine. By substituting the Fourier series of $G^2(\phi_{sm})$ and $B^2(\phi_{sm},\theta_{rm})$ into (4.49), the following equations are obtained

$$T_{cog}(\theta_{rm}) = -\frac{\pi l}{4\mu_0}(r_{st}^2 - r_g^2)\sum_{n=1}^{\infty} nN_L[G_{an}B_{an}\sin(nN_L\theta_{rm})] \tag{4.79}$$

where $N_L$ is the least common multiplier of $S_s$ and $P$, $G_{an}$ and $B_{an}$ are the Fourier coefficients of $G^2(\phi_{sm})$ and $B^2(\phi_{sm},\theta_{rm})$, respectively. From [44], $G_{an}$ can be calculated as

$$G_{an} = -\frac{2S_s}{n\pi N_L}\sin(nN_L\frac{(1-\alpha_{st})\pi}{S_s}) \tag{4.80}$$

In model III, $B_{an}$ is calculated with Laplacian equation and quasi-Poissonian equation which is expressed as

$$B_{an} = \frac{2P}{\pi}\int_0^{\pi/P}\left\{\sum_{i=1,3,5,\ldots}^{\infty}\frac{4PB_r}{\mu_r\pi}\frac{\sin(\frac{i\pi\alpha_{pm}}{2})\left(\frac{r_g}{r_{st}}\right)^{\frac{iP}{2}+1}}{(\frac{iP}{2})^2-1}A\cos(\frac{iP}{2}\theta)\right\}^2\cos(nN_L\theta)d\theta \tag{4.81}$$

where $B_r$ is the magnet residual flux density, $\mu_r$ is the magnet relative permeability, and A is expressed as

$$A=\frac{(\frac{iP}{2}-1)+2\left(\frac{r_{rb}}{r_g}\right)^{\frac{iP}{2}+1}-(\frac{nP}{2}+1)\left(\frac{r_{rb}}{r_g}\right)^{iP}}{\frac{\mu_r+1}{\mu_r}\left[1-\left(\frac{r_{rb}}{r_{st}}\right)^{iP}\right]-\frac{\mu_r-1}{\mu_r}\left[\left(\frac{r_g}{r_{st}}\right)^{iP}-\left(\frac{r_{rb}}{r_g}\right)^{iP}\right]} \tag{4.82}$$

The model is applied to the PMSM considered in Section 4.1.7 with permanent magnet span ratio set as $2/3$. The cogging torque waveform from model III and FEM are compared in Fig. 4.7. The waveform from model III underestimates the cogging torque peak value compared to FEM result but overall the two waveforms are similar.

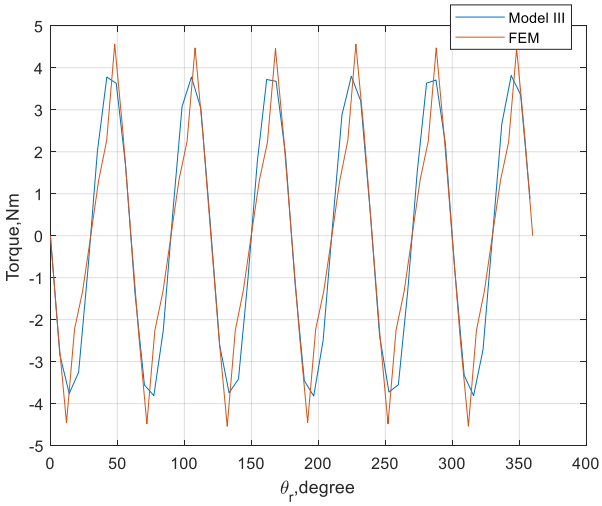


Fig. 4.7 Cogging Torque Waveform

## 4.2 Passive Rectifier Model

In Section 4.1, the PMSM model is established and validated. In this section, the passive rectifier connected to the PMSM to convert ac to dc is considered. The operation of passive rectifier introduces significant current harmonics which are taken into consideration when modeling PMSM. In this section, the passive rectifier model is established based on the waveform reconstruction algorithm proposed in [24]. To achieve the rectifier model, the PMSM is modeled as a voltage behind reactance model as in Fig. 4.8. Therein $v_{as}$, $v_{bs}$, and $v_{cs}$ denote the line-to-neutral voltages and $i_{as}$, $i_{bs}$, and $i_{cs}$ denote the stator currents, which are positive into the machine. The dc output voltage is denoted as $v_r$ and the dc current is denoted as $i_r$.

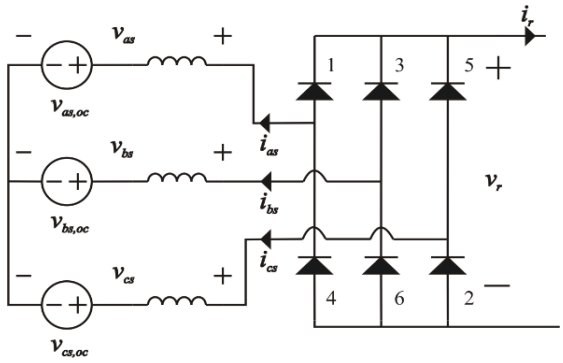


Fig. 4.8 PMSM Connected to a Passive Rectifier

With the PMSM lumped parameter model derived in Section 4.1, the waveform reconstruction algorithm [24] is applied herein to reconstruct the instantaneous voltages $v_{as}(\theta_r)$, $v_{bs}(\theta_r)$, $v_{cs}(\theta_r)$, and $v_r(\theta_r)$ and instantaneous currents $i_{as}(\theta_r)$, $i_{bs}(\theta_r)$, and $i_{cs}(\theta_r)$.

The input parameters to the waveform reconstruction algorithm are the stator resistance $r_s$, $q$-axis subtransient inductance $L_q'' = L_q$, $d$-axis subtransient inductance $L_d'' = L_d$, $q$-axis

subtransient flux linkage $\lambda_q'' = 0$, *d*-axis subtransient flux linkage $\lambda_d'' = \lambda_m'$, diode forward voltage drop $v_t$, rotor electrical speed $\omega_r$, commanded firing angle relative to back EMF $\alpha^*$, dc link average current $\overline{i}_r$, number of rotor positions $N_{\theta r}$ used to represent the waveform, and the vector of rotor positions $\boldsymbol{\theta}_\mathbf{r}$ used to represent the waveform and $p\overline{i}_r / \omega_r$. The Heaviside notation $p = d/dt$ is used here. The outputs of the waveform reconstruction algorithm are *a*-, *b*- and *c*-phase instantaneous current $i_{as}(\theta_r)$, $i_{bs}(\theta_r)$, $i_{cs}(\theta_r)$, the RMS value of the phase current $i_s$, the dc link average voltage $\overline{v}_r$, the average *q*- and *d*- axis current $\overline{i}_q$, $\overline{i}_d$, the firing angle relative to the back EMF $\alpha$, the firing angle relative to rotor position $\beta$, the commutation angle $u$, the operation mode ($\theta_{mode}$) of the rectifier [24], the instantaneous value of *a*-, *b*- and *c*- phase voltage $v_{as}(\theta_r), v_{bs}(\theta_r), v_{cs}(\theta_r)$, and the instantaneous value of dc voltage $v_r(\theta_r)$.

The instantaneous *q*- and *d*- axis current then can be achieved by converting the instantaneous *a*-, *b*- and *c*- phase currents to the rotor reference frame. In particular,

$$\mathbf{i}_{qds}^r(\theta_r) = \mathbf{K}_{s,utr}^r(\theta_r)\mathbf{i}_{abcs}(\theta_r) \tag{4.83}$$

where $\mathbf{K}_{s,utr}^r$ denotes the upper two rows of $\mathbf{K}_s$ with $\theta$ substituted with $\theta_r$. The calculated current $\mathbf{i}_{qds}^r$ is decomposed into Fourier series as (4.30) and (4.31).

## 4.3 Low Pass Filter Model

Due to the passive rectifier, the rectified dc current exhibits significant ripple. A low pass filter ($L_{in}$ and $C_{in}$ in Fig. 1.1) is connected to the rectifier to reduce the current ripple and stabilize

the dc bus voltage. In this section, the low pass filter model is established to predict the input inductor and input capacitor ripple. To this end, the rectifier voltage waveform $v_r(\theta_r)$ determined using the waveform reconstruction algorithm is decomposed into a Fourier series as

$$v_r(\theta_r) \approx \overline{v}_r + \sum_{j=1}^{N} (v_{r,aj} \cos(6j\theta_r) + v_{r,bj} \sin(6j\theta_r)) \tag{4.84}$$

where $N$ is the number of harmonics considered.

The phasor form of the $n^{\text{th}}$ order harmonic of $v_r(\theta_r)$ is expressed as

$$\tilde{v}_{r,n} = \sqrt{\frac{v_{r,an}{}^2 + v_{r,bn}{}^2}{2}} e^{j(\text{angle}(v_{r,an} - jv_{r,bn}))} \tag{4.85}$$

where $\text{angle}(\bullet)$ is a function which returns the phase angle of its complex valued argument.

The impedance of the input inductor and input capacitor at the $n^{\text{th}}$ order harmonic are expressed as

$$Z_{lin,n} = r_{lin} + j\omega_n L_{in} \tag{4.86}$$

$$Z_{cin,n} = r_{cin} - j(\omega_n C_{in})^{-1} \tag{4.87}$$

where $\omega_n = 6n\omega_r$ and $r_{lin}$, $r_{cin}$ are the ESR of the $L_{in}$ and $C_{in}$, respectively.

Assuming the input capacitor has small voltage ripple, the input inductor current ripple $\Delta i_r$ and input capacitor voltage ripple $\Delta v_{cin}$ are calculated using

$$t = \frac{\theta_r}{\omega_r} \tag{4.88}$$

$$\tilde{i}_{r,n} = \tilde{v}_{r,n} / Z_{lin,n} = \frac{i_{r,an} - j i_{r,bn}}{\sqrt{2}} \tag{4.89}$$

$$i_{r,n}(t) = \sqrt{2}\left|\tilde{i}_{r,n}\right| \cos\left(\omega_n t + \text{angle}\left(\tilde{i}_{r,n}\right)\right) \tag{4.90}$$

$$i_r(t) \approx \bar{i}_r + \sum_{n=1}^{N} i_{r,n}(t) \tag{4.91}$$

$$\Delta i_r = \max\left(i_r(t)\right) - \min\left(i_r(t)\right) \tag{4.92}$$

$$\tilde{v}_{cin,n} = \tilde{i}_{r,n} Z_{cin,n} \tag{4.93}$$

$$v_{cin,n}(t) = \sqrt{2}\left|\tilde{v}_{cin,n}\right| \cos\left(\omega_n t + \text{angle}\left(\tilde{v}_{cin,n}\right)\right) \tag{4.94}$$

$$\Delta v_{cin} = \max\left(\sum_{n=1}^{N} v_{cin,n}(t)\right) - \min\left(\sum_{n=1}^{N} v_{cin,n}(t)\right) \tag{4.95}$$

## 4.4 Models Dependency

The PMSM model, passive rectifier model, and the low pass filter model are developed in Section 4.1-Section 4.3. The three models formulate an uncontrolled generation subsystem. It is necessary to discuss the model dependency between the three models. A block diagram is given in Fig. 4.9 to illustrate the model dependency. First, the PMSM lumped parameter model is developed in Section 4.1.5. Then the passive rectifier model established in Section 4.2 is applied to calculate the rectifier instantaneous dc voltage and *qd*-axis current fundamental component and harmonics. The rectifier instantaneous dc voltage is passed to the low pass filter model to calculate the input inductor current ripple and input capacitor voltage ripple. The *qd*-axis current fundamental component and harmonics are passed to the PMSM model to perform the ferromagnetic field analysis.

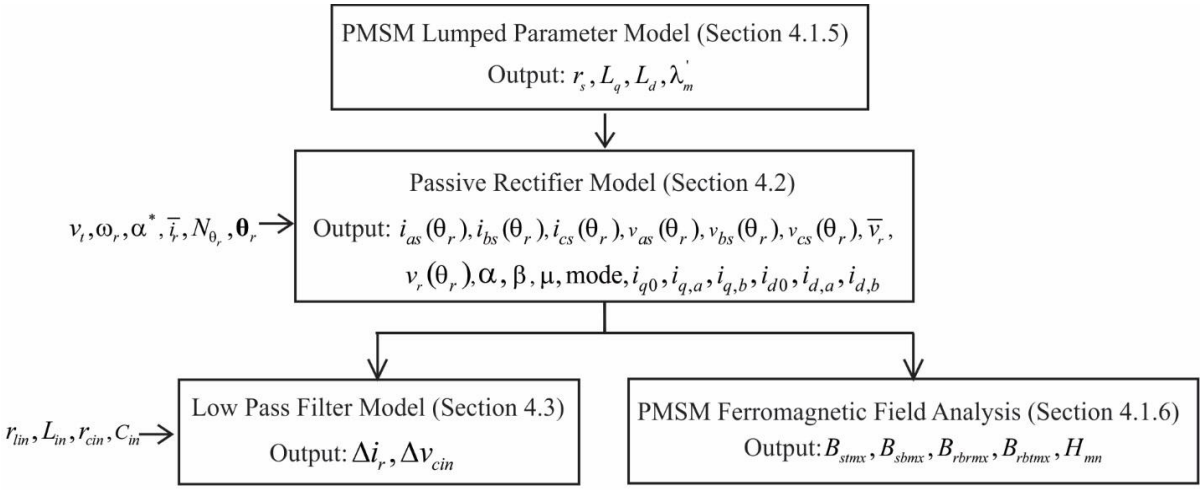


Fig. 4.9 Uncontrolled Generation Subsystem's Model Dependency

# 5. DC GENERATION SYSTEM MODEL

In Chapter 4, the uncontrolled dc generation subsystem models are derived. The dc generation system also includes a dc-dc converter which is connected to the uncontrolled dc generation subsystem to regulate the dc bus voltage. In this chapter, first, a steady-state analysis of the dc generation system is set forth to determine the system operating point. Second, a control strategy is developed to regulate the dc bus voltage. Next, an Average Value Model (AVM) is developed. A linearized model based on the AVM is also derived. The system's small-signal stability analysis and output impedance analysis are performed based on the linear model to insure the system is stable at the rated operating point and that the system has a desired disturbance rejection capability.

## 5.1 System Steady State Analysis

The notional dc generation system topology is shown in Fig. 5.1. Therein, $v_r$ denotes the rectifier dc voltage, $i_r$ denotes the rectifier dc current, $v_c$ denotes the input capacitor voltage, $i_s$ denotes the switching stage current, $v_s$ denotes the switching stage voltage, $i_l$ denotes the output inductor current, $i_{out}$ denotes the system output current, and $v_{out}$ denotes the system output voltage. The full load output inductor current waveform is shown in Fig. 5.2 to analyze the output inductor current ripple. The waveform is also used to determine the MOSFET $T_1$ effective voltage drop $v_{fsw}$ and diode $D_2$ effective voltage drop $v_{fd}$.

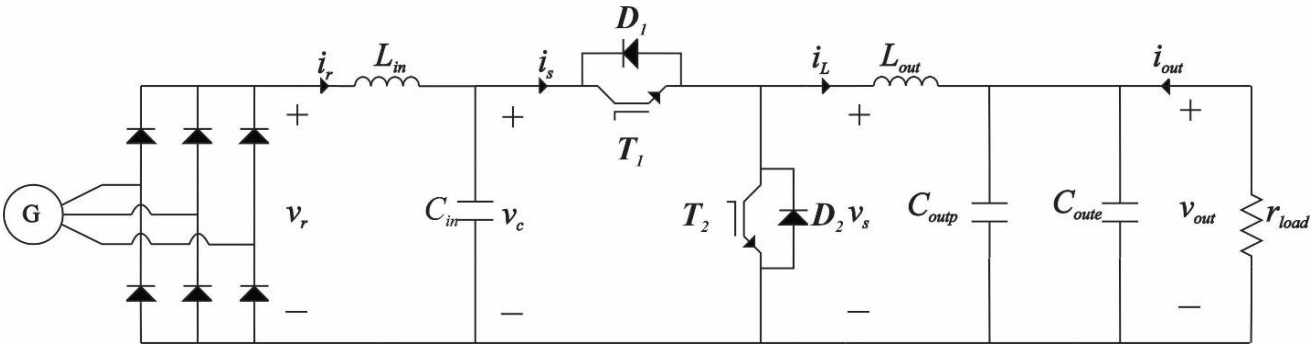


Fig. 5.1 DC Generation System

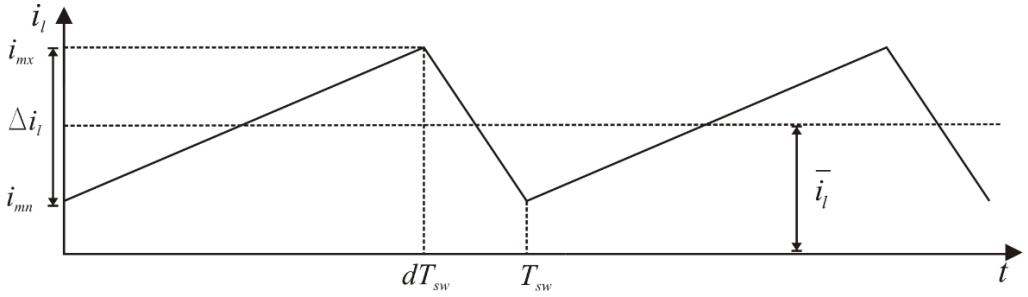


Fig. 5.2 Output Inductor Current Waveform

To perform steady state analysis, the average value of a signal $x$ in steady state is defined as

$$\overline{x} = \frac{1}{T_{sw}} \int_{t_{ss}}^{t_{ss}+T_{sw}} x(t)dt \tag{5.1}$$

where $t_{ss}$ is an instant of time in steady state and $T_{sw}$ is the switching period.

### 5.1.1 Transistor and Diode Voltage Drops Determination

To determine the system steady state operating point, the MOSFET $T_1$ effective voltage drop $v_{fsw}$ and diode $D_2$ effective voltage drop $v_{fd}$ are required. The voltage drops $v_{fsw}$ and $v_{fd}$ are

defined here as if they represented the switch-on state transistor conduction loss and switch-off state diode conduction loss, respectively. However, they are chosen such that they result in the same total loss as predicted by the sum of the conduction and switching loss as calculated using the more detailed models of Chapter 2. They are not the actual semiconductor voltage drops. The $v_{fsw}$ and $v_{fd}$ calculations are described in this section.

During the converter on-state, the transistor conduction loss is calculated as

$$P_t = i_t v_{fsw} \tag{5.2}$$

where $i_t$ is the instantaneous transistor current. Based on the current waveform shown in Fig. 5.2 and (5.1), the average transistor conduction loss is calculated by

$$\bar{P}_t = d\bar{i}_l v_{fsw} \tag{5.3}$$

where *d* is the duty cycle of the output inductor current.

During the converter off-state, the diode conduction loss is calculated as

$$P_d = i_d v_{fd} \tag{5.4}$$

where $i_d$ is the instantaneous transistor current. Based on the current waveform shown in Fig. 5.2 and (5.1), the average diode conduction loss is calculated by

$$\bar{P}_d = (1-d)\bar{i}_l v_{fd} \tag{5.5}$$

The voltage drops $v_{fsw}$ and $v_{fd}$ are selected to result in the same loss as the sum of the semiconductor conduction and switching loss. In particular, $\bar{P}_t$ and $\bar{P}_d$ are calculated as

$$\bar{P}_t = P_{t,cd}\left(i_{mx}, i_{mn}\right) + P_{t,sw}\left(i_{mx}, i_{mn}\right) \tag{5.6}$$

$$\bar{P}_d = P_d\left(i_{mn}, \bar{v}_c, T_{sw}\right) \tag{5.7}$$

where $P_{t,cd}\left(i_{mx}, i_{mn}\right)$, $P_{t,sw}\left(i_{mx}, i_{mn}\right)$, and $P_d\left(i_{mn}, v_c, T_{sw}\right)$ are transistor conduction loss, transistor switching loss, and diode loss calculated from Chapter 2, respectively. The expressions of output inductor current extrema $i_{mx}$ and $i_{mn}$ are given in Section 5.1.3. Based on (5.3) and (5.5)-(5.7), $v_{fsw}$ and $v_{fd}$ are calculated by

$$v_{fsw} = \frac{P_{t,cd}\left(i_{mx}, i_{mn}\right) + P_{t,sw}\left(i_{mx}, i_{mn}\right)}{d\bar{i}_l} \tag{5.8}$$

$$v_{fd} = \frac{P_d\left(i_{mn}, v_c, T_{sw}\right)}{\left(1-d\right)\bar{i}_l} \tag{5.9}$$

In this way, the loss prediction of the average value model is consistent with a detailed analysis of the conduction and switching losses.

### 5.1.2 System Steady State Operating Point Determination

With the transistor voltage drop and diode voltage drop established, the system steady state operating point is determined in this section.

The first step is to determine the switching stage voltage average value $\bar{v}_s$ and current average value $\bar{i}_s$. When $T_1$ is on, $v_s$ equals to $v_c - v_{fsw}$. The $T_1$ on-time is $dT_{sw}$. When $T_1$ is off, $v_s$ equals to $-v_{fd}$. The $T_1$ off-time is $\left(1-d\right)T_{sw}$. Using (5.1), $\bar{v}_s$ can be expressed as

$$\bar{v}_s = d\left(\bar{v}_c - v_{fsw}\right) - \left(1-d\right)v_{fd} \tag{5.10}$$

When $T_1$ is on, $i_s$ equals to $i_l$. When $T_1$ is off, $i_s$ is zero. Using (5.1), $\overline{i_s}$ can be expressed as

$$\overline{i_s} = d\overline{i_l} \tag{5.11}$$

Next, the Kirchhoff's voltage law is applied to the converter. The following equations are obtained

$$\overline{v}_{out} = \overline{v}_s - r_{lout}\overline{i_l} \tag{5.12}$$

$$\overline{v}_c = \overline{v}_r - r_{lin}\overline{i_r} \tag{5.13}$$

where $\overline{i_r} = \overline{i_s}$, $r_{lin}$ and $r_{lout}$ are the ESR of $L_{in}$ and $L_{out}$, respectively.

For steady state condition, $\overline{i_l}$ is expressed as

$$\overline{i_l} = -\overline{i}_{out} \tag{5.14}$$

where $\overline{i}_{out}$ equals to $P_{out} / \overline{v}_{out}$ and $P_{out}$ is the rated output power.

By substituting (5.10), (5.11), (5.13), and (5.14) to (5.12), the following equations are obtained

$$ad^2 + bd + c = 0 \tag{5.15}$$

where

$$a = -r_{lin}P_{out} / \overline{v}_{out} \tag{5.16}$$

$$b = \overline{v}_r - v_{fsw} + v_{fd} \tag{5.17}$$

$$c = -v_{fd} - r_{lout}\overline{i_l} - \overline{v}_{out} \tag{5.18}$$

Since $b$ is positive, the positive root of (5.15) is selected to obtain a valid duty cycle $d$ which is calculated as

$$d = \left(-b + \sqrt{b^2 - 4ac}\right) / (2a) \tag{5.19}$$

Inspection of (5.8)-(5.19) reveals a transcendental system of equations. An iterative algorithm is used to solve these equations based on a Gauss-Seidel approach. A flowchart of the algorithm is shown in Fig. 5.3. In Fig. 5.3, the algorithm starts with an initialization. The initial estimate of the rectifier dc voltage $\overline{v}_r$ is set as an arbitrary number that is larger than $\overline{v}_{out}$. In this work, $\overline{v}_r$ is set as $1.3\overline{v}_{out}$. The initial estimate of rectifier dc current is set as $\overline{i}_r = P_{out} / \overline{v}_r$. The remaining initial estimates are $v_{fsw} = 0$, $v_{fd} = 0$, $k = 1$, and $d = 0$, where $k$ is the iterative counter. The iterative process is finished when the duty cycle error $d_e$ is smaller than a predetermined maximum duty cycle error $d_{e,max}$ or the voltage error $v_e$ is smaller than a predetermined maximum voltage error $v_{e,max}$ or $k$ reaches the predetermined maximum iteration times $k_{max}$. The voltage error $v_e$ is expressed as

$$v_e = \sqrt{\left(v_{fsw} - v_{fswnew}\right)^2 + \left(v_{fd} - v_{fdnew}\right)^2} \tag{5.20}$$

Upon execution of the algorithm of Fig. 5.3, the system steady state operating point is found. The algorithm typically requires less than five iterations to reach to the steady state. The determined operating point will be used in Section 5.4 as the equilibrium point for the small-signal stability analysis and disturbance rejection analysis.

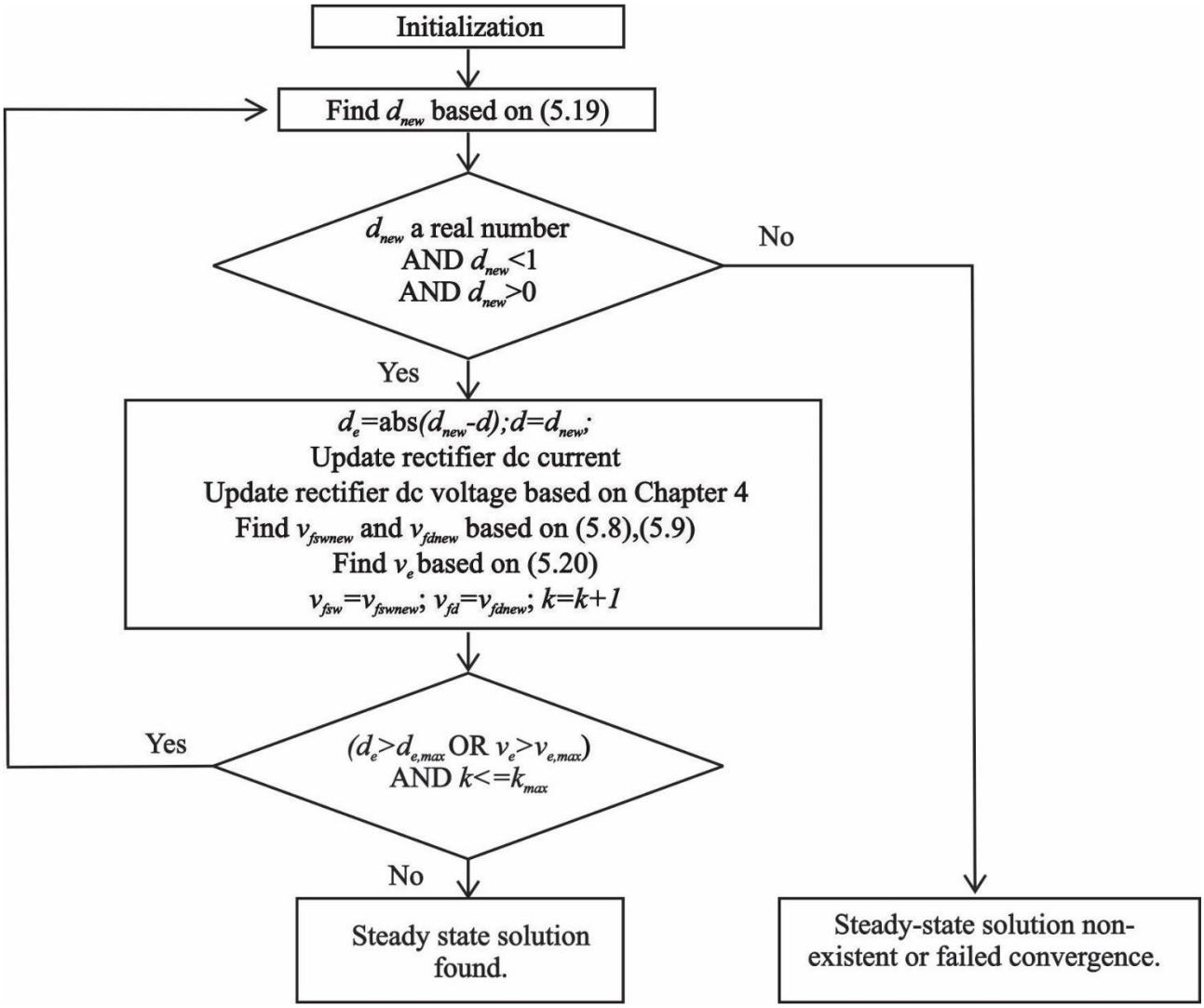


Fig. 5.3 System Steady State Analysis

### 5.1.3 Output Inductor Current Ripple and Output Voltage Ripple Determination

The output inductor current ripple and the output voltage ripple are determined in this section. The output inductor current ripple $\Delta i_l$ is obtained by applying Kirchhoff's voltage law to the converter on-state and off-state topologies combined with the output inductor current waveform shown in Fig. 5.2.

During the converter on-state, applying Kirchhoff's voltage law to the converter yields

$$-v_c + v_{fsw} + L_{out}\frac{di_l}{dt} + r_{lout}i_l + v_{out} = 0 \tag{5.21}$$

Assuming the inductor current waveform shown in Fig. 5.2, (5.21) becomes

$$L_{out}\frac{\Delta i_l}{dT_{sw}} = v_c - v_{fsw} - r_{lout}i_l - v_{out} \tag{5.22}$$

In (5.22), $v_c$ can be substituted with $\overline{v}_c$ assuming the input capacitor voltage doesn't have a significant variation in the steady state.

During the converter off-state, applying Kirchhoff's voltage law to the converter yields

$$v_{fd} + L_{out}\frac{di_l}{dt} + r_{lout}i_l + v_{out} = 0 \tag{5.23}$$

In view of the waveform shown in Fig 5.2, (5.23) yields

$$L_{out}\frac{\Delta i_l}{(1-d)T_{sw}} = v_{fd} + r_{lout}i_l + v_{out} \tag{5.24}$$

Based on (5.13), (5.22), and (5.24), the output inductor ripple $\Delta i_l$ is expressed as

$$\Delta i_l = \frac{d(1-d)}{(L_{out}\ f_{sw})}\left(\overline{v}_r - r_{lin}\overline{i}_r - v_{fsw} + v_{fd}\right) \tag{5.25}$$

The extrema of the output inductor current waveform $i_{mx}$ and $i_{mn}$ are given by

$$i_{mx} = \overline{i}_l + \Delta i_l / 2 \tag{5.26}$$

$$i_{mn} = \overline{i}_l - \Delta i_l / 2 \tag{5.27}$$

To determine the output voltage ripple, it is necessary to first find the output inductor current spectrum and the output capacitor bank impedance.

Given $i_{mn}$, $i_{mx}$, $d$, and $f_{sw}$, the output inductor current waveform $i_l(t)$ is achieved based on Fig. 5.2. The $i_l(t)$ is decomposed into Fourier series as

$$i_l(t) \approx \bar{i}_l + \sum_{j=1}^{N_{il}} (i_{l,aj} \cos(j\omega t) + i_{l,bj} \sin(j\omega t)) \tag{5.28}$$

where $N_{il}$ is the number of harmonics considered, $\omega = 2\pi f_{sw}$, and $i_{l,aj}$ and $i_{l,bj}$ are the Fourier coefficients which are given by

$$i_{l,aj} = 0 \tag{5.29}$$

$$i_{l,bj} = -\frac{(i_{mx} - i_{mn})(-1)^j}{j^2 \pi^2 d(1-d)} \sin(j\pi(1-d)) \tag{5.30}$$

The phasor form of the $n^{\text{th}}$ order harmonic of $i_l(t)$ is expressed as

$$\phi = \text{angle}(i_{l,an} - j i_{l,bn}) \tag{5.31}$$

$$\tilde{i}_{l,n} = \sqrt{\frac{i_{l,an}{}^2 + i_{l,bn}{}^2}{2}} e^{j\phi} \tag{5.32}$$

The impedance of the output polypropylene capacitor and the output electrolytic capacitor at the $n^{\text{th}}$ order harmonic are expressed

$$Z_{coutp,n} = r_{coutp} + (j\omega_{nfsw} C_{oup})^{-1} \tag{5.33}$$

$$C_{oute,n} = C_{oute} \left( \alpha_c + \frac{1-\alpha_c}{1+\left(nf_{sw} / f_C\right)^{n_C}} \right) \tag{5.34}$$

$$Z_{coute,n} = r_{coute} + (j\omega_{nfsw} C_{oute,n})^{-1} \tag{5.35}$$

where $\omega_{nfsw} = 2n\pi f_{sw}$, $\alpha_c$, $f_C$, and $n_C$ are given in Chapter 3, and $r_{coutp}$, $r_{coute}$ are the ESR of $C_{outp}$ and $C_{oute}$, respectively.

The impedance of the output capacitor bank at the n[th] order harmonic is expressed

$$Z_{cout,n} = \frac{Z_{coutp,n} Z_{coute,n}}{Z_{coutp,n} + Z_{coute,n}} \tag{5.36}$$

Then the output voltage ripple is calculated using

$$\tilde{v}_{out,n} = \tilde{i}_{l,n} Z_{cout,n} \tag{5.37}$$

$$v_{out,n}(t) = \sqrt{2}\left|\tilde{v}_{out,n}\right| \cos\left(\omega_{nfsw} t + \text{angle}\left(\tilde{v}_{out,n}\right)\right) \tag{5.38}$$

$$\Delta v_{out} = \max\left(\sum_{n=1}^{N_{il}} v_{out,n}(t)\right) - \min\left(\sum_{n=1}^{N_{il}} v_{out,n}(t)\right) \tag{5.39}$$

### 5.1.4 RMS Capacitor Current Analysis

It is necessary to compute the RMS currents in each capacitor in order to ensure the capacitor temperature rise is under the rated value. The input capacitor sees the current ripple from the rectifier and the switching current from the transistor.

The RMS value of the rectifier current ripple $I_{rms,cin\_rec}$ is expressed as

$$I_{rms,cin\_rec} = \sqrt{\frac{1}{2}\sum_{n=1}^{N} (i_{r,an}^2 + i_{r,bn}^2)} \tag{5.40}$$

where $i_{r,an}$ and $i_{r,bn}$ are obtained from (4.89).

Next, the ripple component due to the transistor switching is analyzed. When transistor is on, $i_s$ is approximated as $\bar{i}_l$ and $i_r$ is approximated as $d\bar{i}_l$. Thus the input capacitor sees a current of $(d-1)\bar{i}_l$. When transistor is off, $i_s$ is 0 and $i_r$ is approximated as $d\bar{i}_l$. Thus the input capacitor sees a current of $d\bar{i}_l$. The RMS value of switch current ripple $I_{rms,cin\_t}$ can be approximated as

$$I_{rms,cin\_t} = \bar{i}_l \sqrt{d(1-d)} \tag{5.41}$$

Since the transistor switching frequency is much higher than the rectifier ripple frequency, the rectifier ripple and the switching ripple are essentially orthogonal (the average of the product of the two components is zero). Thus the total RMS current of $C_{in}$ may be found from

$$I_{rms,cin} = \sqrt{I_{rms,cin\_rec}^2 + I_{rms,cin\_t}^2} \tag{5.42}$$

Based on the output inductor current spectrum and the output capacitor's impedance derived in the previous section, the RMS current of the output polypropylene capacitor $I_{rms,Coutp}$ and the RMS current of the output electrolytic capacitor $I_{rms,Coute}$ can be calculated using

$$\tilde{i}_{coup,n} = \tilde{i}_{l,n} \frac{Z_{coute,n}}{Z_{coute,n} + Z_{coutp,n}} = \frac{i_{coup,an} - j i_{coup,bn}}{\sqrt{2}} \tag{5.43}$$

$$I_{rms,Coutp} = \sqrt{\frac{1}{2} \sum_{n=1}^{N_{il}} (i_{coup,an}^2 + i_{coup,bn}^2)} \tag{5.44}$$

$$\tilde{i}_{coue,n} = \tilde{i}_{l,n} \frac{Z_{coutp,n}}{Z_{coute,n} + Z_{coutp,n}} = \frac{i_{coue,an} - j i_{coue,bn}}{\sqrt{2}} \tag{5.45}$$

$$I_{rms,Coute} = \sqrt{\frac{1}{2}\sum_{n=1}^{N_{il}}(i_{coue,an}^2 + i_{coue,bn}^2)} \tag{5.46}$$

## 5.2 Control and Control Design

To regulate the dc bus voltage, a multi-loop duty cycle controller is applied to the system. The proposed controller contains a voltage control loop, a current control loop, and a low pass filter. The block diagram is shown in Fig. 5.4. In Fig. 5.4, $v_{out}^*$ is the output voltage command, $v_{out}$ is the measured output voltage, $i_{out}$ is the measured output current, $i_l$ is the measured output inductor current, $i_{limit}$ is the anti-windup current limit, $i_l^*$ is the output inductor current command, $d^*$ is the duty cycle command, and $\hat{d}^*$ is the duty cycle command after the low pass filter. A PI controller is applied in the voltage control loop. Anti-windup is used in the PI controller to avoid integral wind-up. The current control loop contains a proportional controller. The low pass filter is applied to the duty cycle command to filtering switching frequency component.

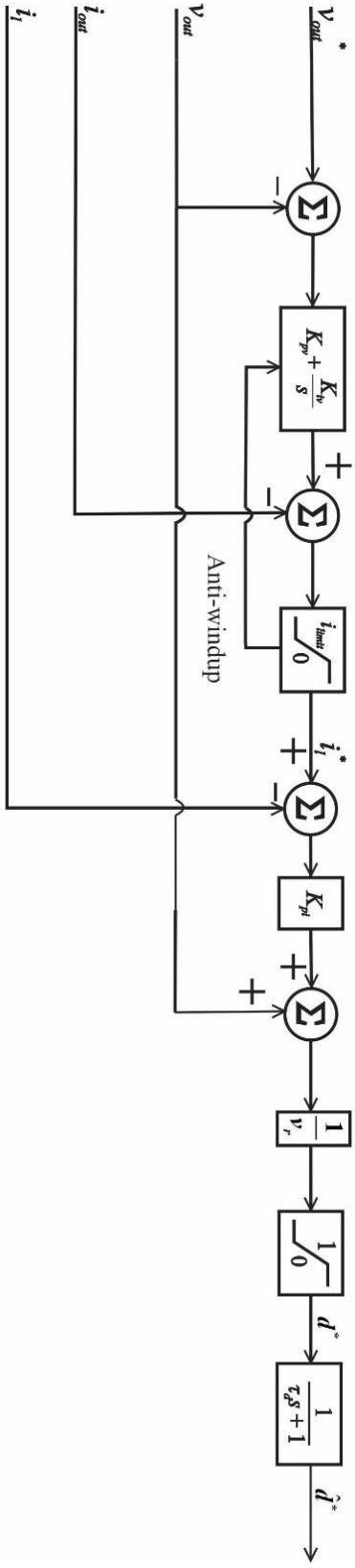


Fig. 5.4 Duty Cycle Controller

The design methodology proposed in this work is to integrate the controller design to the design process. Since the control architecture is fixed by Fig. 5.4, the parameters that need to be decided are the controller gains and the low pass filter time constant. In [15], the controller gains are set as part of the design space. The approach used in this work is to tie the controller gains and low pass filter time constant to the converter switching frequency. Compared to the approach used in [15], this approach achieves a smaller design space which helps the optimization convergence. The approach used in this work can also demonstrate how the switching frequency influences the system dynamic performance.

For the low pass filter, the pole location is set as

$$s_\tau = -2\pi f_{sw} / 10 \tag{5.47}$$

Thus the duty cycle command is immune to the switching frequency ripple. The time constant is calculated based on the pole location as

$$\tau_d = -1/s_\tau = 5/(\pi f_{sw}) \tag{5.48}$$

For the current control loop, the pole location is set as

$$s_i = -2\pi f_{sw} / 50 \tag{5.49}$$

Thus the current control loop is five times slower than the low pass filter. The current control loop transfer function is expressed as

$$i_l = \frac{K_{pi}}{L_{out}s + r_{lout} + K_{pi}} i_l^* \tag{5.50}$$

Based on the pole location and the current loop transfer function, the proportional gain is expressed as

$$K_{pi} = -s_i L_{out} - r_{lout} = \pi f_{sw} L_{out} / 25 - r_{Lout} \tag{5.51}$$

For the voltage control loop, the pole locations are set to

$$s_{v1} = s_{v2} = -2\pi f_{sw} / 250 \tag{5.52}$$

Thus the voltage control loop is five times slower than the current control loop and the $i_l^*$ can be treated as a constant to the current control loop. To calculate the voltage control loop gains, it is convenient to lump $C_{outp}$ and $C_{oute}$ together. Since the disturbance frequency is relatively low, the lumped capacitors' effective capacitance is the summation of $C_{outp}$ and $C_{oute}$. The lumped capacitors' ESR is the parallel combination of $C_{outp}$ ESR and $C_{oute}$ ESR. Therefore

$$C_{out} = C_{outp} + C_{oute} \tag{5.53}$$

$$r_{cout} = \frac{r_{coutp} r_{coute}}{r_{coutp} + r_{coute}} \tag{5.54}$$

The voltage control loop transfer function is expressed as

$$v_{out} = \frac{(K_{pv} r_{cout} C_{out}) s^2 + (K_{pv} + K_{iv} r_{cout} C_{out}) s + K_{iv}}{(C_{out} + r_{cout} C_{out} K_{pv}) s^2 + (K_{pv} + K_{iv} r_{cout} C_{out}) s + K_{iv}} v_{out}^* \tag{5.55}$$

Based on the desired pole locations ( $s = s_{v1}$ and $s = s_{v2}$ ) and the voltage control loop transfer function, the proportional gain is

$$K_{pv} = -\frac{C_{out}}{(s_{v1} + s_{v2} + s_{v1} s_{v2} r_{Cout} C_{out})^{-1} + C_{out} r_{Cout}} \tag{5.56}$$

and the integral gain is

$$K_{iv} = s_{v1} s_{v2} C_{out} (1 + r_{Cout} K_{pv}) \tag{5.57}$$

## 5.3 System Stability and Disturbance Rejection Capability Analysis

The system stability and disturbance rejection capability are two important design criteria. Time domain analysis is widely used to predict the system's disturbance rejection capability. However, this approach is computationally expensive; thus, it is not ideal for optimization based design. In this work, a computationally efficient frequency domain analysis is developed. The first step is to establish an Average Value Model (AVM) of the system. Then a linearized system model is developed based on the AVM for small-signal stability analysis and disturbance rejection capability analysis.

### 5.3.1 Average Value Modeling

According to [15], the variables in AVM are represented in such a way that the non-linearities and primary dynamics are captured in a moving average sense. The state variables of AVM are constant at steady state. The average value of $x$ at any instant of time is defined as

$$\hat{x} = \frac{1}{T_{sw}} \int_{t}^{t+T_{sw}} x(\tau) d\tau \tag{5.58}$$

The value of the steady state of the variable $\hat{x}$, is denoted by $\bar{x}$ which is given by (5.1).

To establish the AVM of the notional system, the PMSM and the rectifier are represented by an equivalent circuit [45]. In [45], the average dc voltage of a three-phase semi-controlled bridge converter is expressed as

$$\hat{v}_d = \frac{3\sqrt{6}}{\pi} E \cos\alpha - \frac{3}{\pi} l_c \omega_g \hat{i}_d - 2l_c \frac{d\hat{i}_d}{dt} \tag{5.59}$$

where $E$ is the rms magnitude of the source voltage, $\alpha$ is the converter firing angle, $l_c$ is the commutating inductance, $\omega_g$ is the source frequency and $\hat{i}_d$ is the average dc current during $1/6$ of the source period. In the notional system, a symmetrical PMSM is selected as the ac source. The rms magnitude of the source voltage is the PMSM back-emf which is expressed as

$$E = \frac{1}{\sqrt{2}} \lambda'_m \omega_r \tag{5.60}$$

The commutating inductance is set as the *q*-axis inductance $L_q$ since the saliency of the generator is low. The source frequency is $\omega_r$ . The average dc voltage and average dc current in the notional system are denoted as $\hat{v}_r$ and $\hat{i}_r$ , respectively. The voltage drop on the stator resistance $r_s$ is included. The firing angle for a rectifier is zero. Thus for the notional PMSM-rectifier application, (5.59) can be rewritten as

$$\hat{v}_r = \frac{3\sqrt{3}}{\pi} \lambda'_m \omega_r - \left( 2r_s + \frac{3}{\pi} L_q \omega_r \right) \hat{i}_r - 2L_q \frac{d\hat{i}_r}{dt} \tag{5.61}$$

From (5.58) and (5.61), the AVM of the system is shown in Fig. 5.5. In Fig. 5.5, $r_c$ is the PMSM-rectifier equivalent circuit resistance, $L_c$ is the commutating inductance, and $v_{source}$ is the equivalent circuit voltage source. These quantities may be expressed as

$$r_c = 2r_s + \frac{3}{\pi} L_q \omega_r \tag{5.62}$$

$$L_c = L_q \tag{5.63}$$

$$v_{source} = (3\sqrt{3}/\pi) \lambda'_m \omega_r \tag{5.64}$$

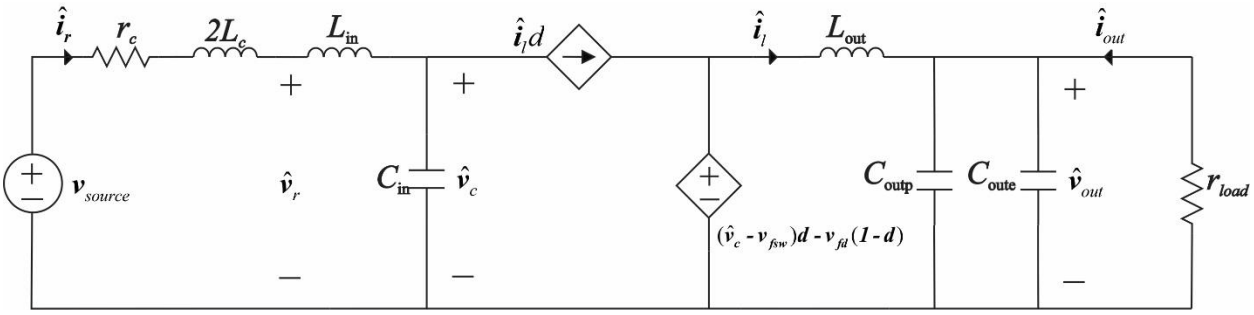


Fig. 5.5 System Average Value Model

### 5.3.2 Linear Modeling

The system AVM is linearized to perform the small-signal stability analysis and disturbance rejection analysis. The perturbation of a signal $\hat{x}$ from the steady state operating point $\overline{x}_o$ is defined as

$$\Delta\hat{x} = \hat{x} - \overline{x}_o \tag{5.65}$$

The system's perturbed variables are expressed

$$\Delta\hat{i}_r = \hat{i}_r - \overline{i}_r \tag{5.66}$$

$$\Delta\hat{v}_{cin} = \hat{v}_{cin} - \overline{v}_{cin} \tag{5.67}$$

$$\Delta\hat{i}_l = \hat{i}_l - \overline{i}_l \tag{5.68}$$

$$\Delta\hat{v}_{coutp} = \hat{v}_{coutp} - \overline{v}_{coutp} \tag{5.69}$$

$$\Delta\hat{v}_{coute} = \hat{v}_{coute} - \overline{v}_{coute} \tag{5.70}$$

$$\Delta\hat{d} = \hat{d} - \overline{d} \tag{5.71}$$

$$\Delta\hat{x}_{kiv} = \hat{x}_{kiv} - \overline{x}_{kiv} \tag{5.72}$$

where $v_{cin}$ is the capacitor $C_{in}$ voltage, $v_{coutp}$ is the polypropylene output capacitor $C_{outp}$ voltage, $v_{coute}$ is the electrolytic output capacitor $C_{oute}$ voltage, and $x_{kiv}$ is a variable associated with the controller integral feedback. It should be noted that the capacitor voltage $v_{cin}$, $v_{coutp}$, and $v_{coute}$ does not include the voltage drop across the capacitor equivalent series resistance (ESR).

The linearized system model is expressed as

$$\frac{d\Delta\hat{\mathbf{x}}}{dt} = \mathbf{A}\Delta\hat{\mathbf{x}} + \mathbf{B}\Delta\hat{\mathbf{u}} \tag{5.73}$$

$$\Delta\hat{\mathbf{y}} = \mathbf{C}\Delta\hat{\mathbf{x}} + \mathbf{D}\Delta\hat{\mathbf{u}} \tag{5.74}$$

where $\Delta\hat{\mathbf{x}}$ is the state vector of the linearized system which is expressed as

$$\Delta\hat{\mathbf{x}} = \begin{bmatrix} \Delta\hat{i}_r & \Delta\hat{v}_{cin} & \Delta\hat{i}_l & \Delta\hat{v}_{coutp} & \Delta\hat{v}_{coute} & \Delta\hat{d} & \Delta\hat{x}_{kiv} \end{bmatrix}^T \tag{5.75}$$

The input vector is denoted as $\Delta\hat{\mathbf{u}}$ which is the dc output current perturbation $\Delta\hat{i}_{out}$. The output vector is denoted as $\Delta\hat{\mathbf{y}}$ which is taken to be the dc output voltage $\Delta\hat{v}_{out}$.

Based on the AVM given in Fig. 5.5 and the system controller shown in Fig. 5.4, the matrix $\mathbf{A}$ is derived as

$$\mathbf{A}=\begin{bmatrix} -\frac{r_{lin}+r_{cin}+r_c}{L_{in}+2L_c} & -\frac{1}{L_{in}+2L_c} & \frac{r_{cin}\bar{d}}{L_{in}+2L_c} & 0 & 0 & \frac{r_{cin}\bar{i}_l}{L_{in}+2L_c} & 0 \\ \frac{1}{C_{in}} & 0 & -\frac{\bar{d}}{C_{in}} & 0 & 0 & -\frac{\bar{i}_l}{C_{in}} & 0 \\ \frac{r_{cin}\bar{d}}{L_{out}} & \frac{\bar{d}}{L_{out}} & a_{33} & a_{34} & a_{35} & a_{36} & 0 \\ 0 & 0 & a_{43} & a_{44} & a_{45} & 0 & 0 \\ 0 & 0 & a_{53} & a_{54} & a_{55} & 0 & 0 \\ a_{61} & a_{62} & a_{63} & a_{64} & a_{65} & a_{66} & \frac{K_{pi}}{\tau_d v_{r,e}} \\ 0 & 0 & a_{73} & a_{74} & a_{75} & 0 & 0 \end{bmatrix} \tag{5.76}$$

In (5.76), The partial derivative terms $\frac{\partial v_{out}}{\partial v_{coutp}}$, $\frac{\partial v_{out}}{\partial v_{coute}}$, and $\frac{\partial v_{out}}{\partial i_l}$ are calculated using the following sequence

$$r_{T,out}=\frac{r_{coutp}r_{coute}}{r_{coutp}+r_{coute}} \tag{5.77}$$

$$\frac{\partial v_{out}}{\partial v_{coutp}}=\frac{r_{coute}}{r_{coutp}+r_{coute}}\frac{r_{load}}{r_{T,out}+r_{load}} \tag{5.78}$$

$$\frac{\partial v_{out}}{\partial v_{coute}}=\frac{r_{coutp}}{r_{coutp}+r_{coute}}\frac{r_{load}}{r_{T,out}+r_{load}} \tag{5.79}$$

$$\frac{\partial v_{out}}{\partial i_l}=\frac{r_{T,out}r_{load}}{r_{T,out}+r_{load}} \tag{5.80}$$

where $r_{T,out}$ is the converter output interface Thevenin equivalent circuit resistance, $r_{coutp}$ is the output polypropylene capacitor ESR, and $r_{coute}$ is the output electrolytic capacitor ESR.

The elements of the form $a_{mn}$ in $\mathbf{A}$ are calculated using the sequence

$$v_{r,e} = \frac{\bar{i}_r \left(2L_c(r_{cin} + r_{lin}) - r_c L_{in}\right) + 2L_c \bar{v}_{cin} - 2L_c r_{cin} \bar{i}_l \bar{d} + v_{source} L_{in}}{L_{in} + 2L_c} \tag{5.81}$$

$$v_{out,e} = \frac{\left(\bar{v}_{coutp} + (\bar{i}_l + \bar{v}_{coue} / r_{coue}) r_{coup}\right) r_{coue}}{r_{coup} + r_{coute}} \frac{r_{load}}{r_{T,out} + r_{load}} \tag{5.82}$$

$$a_{33} = -\frac{r_{lout}}{L_{out}} - \frac{r_{cin}\bar{d}^2}{L_{out}} - \frac{\frac{\partial v_{out}}{\partial i_l}}{L_{out}} \tag{5.83}$$

$$a_{34} = -\frac{\frac{\partial v_{out}}{\partial v_{coutp}}}{L_{out}} \tag{5.84}$$

$$a_{35} = -\frac{\frac{\partial v_{out}}{\partial v_{coute}}}{L_{out}} \tag{5.85}$$

$$a_{36} = \frac{-2r_{cin}\bar{i}_l\bar{d} + \bar{v}_{cin} + r_{Cin}\bar{i}_r - v_{fsw} + v_{fd}}{L_{out}} \tag{5.86}$$

$$a_{43} = \frac{\frac{\partial v_{out}}{\partial i_l}}{r_{coutp} C_{outp}} \tag{5.87}$$

$$a_{44} = \frac{\frac{\partial v_{out}}{\partial v_{coutp}} - 1}{r_{coutp} C_{outp}} \tag{5.88}$$

$$a_{45} = \frac{\frac{\partial v_{out}}{\partial v_{coute}}}{r_{coutp} C_{outp}} \tag{5.89}$$

$$a_{53} = \frac{\frac{\partial v_{out}}{\partial i_l}}{r_{coute} C_{oute}} \tag{5.90}$$

$$a_{54} = \frac{\frac{\partial v_{out}}{\partial v_{coutp}}}{r_{coute} C_{oute}} \tag{5.91}$$

$$a_{55} = \frac{\frac{\partial v_{out}}{\partial v_{coute}} - 1}{r_{coute} C_{oute}} \tag{5.92}$$

$$a_{61} = -\frac{v_{out,e} + K_{pi} \bar{x}_{kiv}}{v_{r,e}^2 \tau_d} \frac{2L_c (r_{cin} + r_{lin}) - r_c L_{in}}{L_{in} + 2L_c} \tag{5.93}$$

$$a_{62} = -\frac{v_{out,e} + K_{pi} \bar{x}_{kiv}}{v_{r,e}^2 \tau_d} \frac{2L_c}{L_{in} + 2L_c} \tag{5.94}$$

$$a_{63} = \frac{v_{out,e} + K_{pi} \bar{x}_{kiv}}{v_{r,e}^2 \tau_d} \frac{2L_c r_{cin} \bar{d}}{L_{in} + 2L_c} + \frac{\frac{\partial v_{out}}{\partial i_l} (1 - K_{pi} K_{pv}) - K_{pi}}{v_{r,e} \tau_d} \tag{5.95}$$

$$a_{64} = \frac{\partial v_{out}}{\partial v_{coutp}} \frac{1 - K_{pi} K_{pv}}{v_{r,e} \tau_d} \tag{5.96}$$

$$a_{65} = \frac{\partial v_{out}}{\partial v_{coute}} \frac{1 - K_{pi} K_{pv}}{v_{r,e} \tau_d} \tag{5.97}$$

$$a_{66} = -\frac{1}{\tau_d} + \frac{v_{out,e} + K_{pi} \bar{x}_{kiv}}{v_{r,e}^2 \tau_d} \frac{2L_c r_{cin} \bar{i}_l}{L_{in} + 2L_c} \tag{5.98}$$

$$a_{73} = -K_{iv} \frac{\partial v_{out}}{\partial i_l} \tag{5.99}$$

$$a_{74} = -K_{iv} \frac{\partial v_{out}}{\partial v_{coutp}} \tag{5.100}$$

$$a_{75} = -K_{iv} \frac{\partial v_{out}}{\partial v_{coute}} \tag{5.101}$$

where $r_{cin}$ is the input capacitor ESR, $r_{lin}$ is the input inductor ESR, and $r_{lout}$ is the output inductor ESR.

The $\mathbf{B}$ matrix is expressed as

$$\mathbf{B} = \begin{bmatrix} 0 \\ 0 \\ 0 \\ 0 \\ 0 \\ -\dfrac{K_{pi}}{v_{r,e}\tau_d} \\ 0 \end{bmatrix} \tag{5.102}$$

The $\mathbf{C}$ matrix is given by

$$\mathbf{C} = [0 \quad 0 \quad \frac{\partial v_{out}}{\partial i_l} \quad \frac{\partial v_{out}}{\partial v_{coutp}} \quad \frac{\partial v_{out}}{\partial v_{coute}} \quad 0 \quad 0] \tag{5.103}$$

The $\mathbf{D}$ matrix is zero.

With the state space form derived, the system output impedance transfer function is expressed as

$$Z_{out} = \frac{\Delta \hat{v}_{out}}{\Delta \hat{i}_{out}} = \mathbf{C}(s\mathbf{I} - \mathbf{A})^{-1}\mathbf{B} + \mathbf{D} \tag{5.104}$$

where $Z_{out}$ is the system output impedance.

At this point, the system's stability and disturbance rejection capability can be evaluated. The system's small-signal stability is guaranteed if all the eigenvalues of $\mathbf{A}$ are in the open left half plane. The system's disturbance rejection capability is characterized by (5.104). For a given

output dc current disturbance at a given frequency, the output voltage deviation is limited if the magnitude of $Z_{out}$ at that frequency is limited.

Although the system's disturbance rejection capability could be checked by performing a time domain simulation, the proposed output impedance analysis approach is much more computational efficient because stiffness is not an issue in the frequency domain. In the proposed optimization based design methodology, two constraints are formulated to guarantee the system's stability and disturbance rejection capability. The first constraint is to ensure all the eigenvalues of $\mathbf{A}$ are in the open left half plane. The second constraint is to ensure the magnitude of $Z_{out}$ is small compared to the nominal output impedance over the frequency range of interest. The nominal output impedance is defined as $\bar{v}_{out}^2 / P_{out}$. This will be further discussed in Chapter 6.

# 6. DC GENERATION SYSTEM DESIGN

The dc generation system's component models are developed in Chapter 2-Chapter 4. The system steady state analysis, stability analysis, and disturbance rejection analysis are set forth in Chapter 5. In this chapter, the models developed are applied to formulate a design study of the notional dc generation system. The proposed design methodology is to cast the system design problem as an optimization problem. The first step in this process is to define the design space which is covered in Section 6.1. The optimization constraints and metrics are introduced in Section 6.2. In Section 6.3, the system specifications of a 10 kW dc generation system are set forth to serve as a case study. The results are presented in Section 6.4. As pointed out in Chapter 1, one of the objectives of this work is to evaluate the advantage of WBG devices. To achieve this objective, the results of a SiC semiconductor based design case study are compared to those of a Si semiconductor based design case study in Section 6.5.

## 6.1 Design Space

The system design space consists of the free and independent parameters that are required to describe the system. For the notional dc generation system design, twenty independent design parameters are required. The design parameters are grouped into the vector $\boldsymbol{\theta}_s$, which is expressed as

$$\boldsymbol{\theta}_s = [P_p \; r_{st} \; d_{rb} \; d_m \; g \; d_{tb} \; \alpha_t \; d_{sb}^* \; \alpha_{pm} \; B_r^* \; l \; N_{s1}^* \; f_{sw} \; L_{in} \; J_{Lin} \; L_{out} \; J_{Lout} \; C_{in} \; C_{outp} \; C_{oute}] \qquad (6.1)$$

where $P_p$ is the number of pole pairs, $r_{st}$, $d_{rb}$, $d_m$, $g$, $d_{tb}$, $\alpha_t$, $\alpha_{pm}$, and $l$ are the PMSM geometrical parameters that are defined in Chapter 4, $d_{sb}^*$ is the desired stator backiron depth, $B_r^*$

is the desired permanent magnet residual flux density, $N_{s1}^{*}$ is the peak value of the fundamental component of the stator conductor density function, $f_{sw}$ is the converter switching frequency, $L_{in}$, $L_{out}$, $C_{in}$, $C_{outp}$, and $C_{oute}$ are the converter passive components defined in Chapter 1, and $J_{Lin}$ and $J_{Lout}$ are the input inductor current density and output inductor current density, respectively.

## 6.2 Design Constraints, Metrics, and Fitness Function

To achieve a viable system design, it is necessary to impose constraints on the optimization. The function ltn() and gtn() defined in Chapter 3 are used here to describe the constraints. The description of these constraints is given in this section.

The first constraint is to ensure that the depth of the inert region $d_i$ is larger than zero. Since $d_i$ is calculated using

$$d_i = r_{st} - g - d_m - d_{rb} - r_{rs} \tag{6.2}$$

and $r_{st}$, $g$, $d_m$, and $d_{rb}$ are independent variables and $r_{rs}$ is fixed, it is possible to produce a design with negative $d_i$. The constraint is expressed as

$$c_1 = \text{gte}\left(d_i, 0\right) \tag{6.3}$$

The radius of the PMSM is limited by a maximum allowed radius $r_{ss,lim}$. The depth of the stator backiron is calculated by

$$d_{sb} = \min(d_{sb}^{*}, r_{ss,lim} - r_{st} - d_{tb}) \tag{6.4}$$

This approach can give a design with negative $d_{sb}$; thus the constraint

$$c_2 = \mathrm{gte}\left(d_{sb}, 0\right) \tag{6.5}$$

is imposed.

The cogging torque peak value $T_{cog,peak}$ is calculated from Section 4.1.9. The constraint that limits the $T_{cog,peak}$ is expressed as

$$T_{ave} = \frac{P_{out}}{\omega_{rm}} \tag{6.6}$$

$$c_3 = \mathrm{lte}\left(T_{cog,peak}, T_{ave}\alpha_{cogging}\right) \tag{6.7}$$

where $T_{ave}$ is the average torque at rated operating point, and $\alpha_{cogging}$ is the cogging torque peak value specification.

A maximum aspect ratio is imposed on the stator teeth to ensure a mechanically sound structure. The constraint is expressed as

$$c_4 = \mathrm{ltn}\left(d_{st} / w_{tb}, \alpha_{tar}\right) \tag{6.8}$$

where $\alpha_{tar}$ is the maximum tooth aspect ratio.

For structural reasons, a constraint is imposed on the ratio between permanent magnet height and width. In particular,

$$c_5 = \mathrm{ltn}\left(\frac{d_m}{2\pi r_{rb}\alpha_{pm} / P}, \alpha_{pmr}\right) \tag{6.9}$$

where $\alpha_{pmr}$ is the maximum permanent magnet aspect ratio.

The rotor tip speed is limited to avoid large centrifugal force which could damage the permanent magnet. The constraint is expressed as

$$c_6 = \mathrm{ltn}\left(r_{rb}\max(\omega_{rm}), v_{tpmx}\right) \tag{6.10}$$

where $v_{tpmx}$ is the maximum allowed tip speed.

To facilitate the winding construction, the slot opening must be larger than the diameter of the winding conductor $d_{ss}$ multiplied by the slot opening factor $\alpha_{so}$. The associated constraint is expressed as

$$c_7 = \mathrm{ltn}\left(d_{ss}\alpha_{so}, w_{so}\right) \tag{6.11}$$

To avoid a design with an impractically small wire, a constraint is imposed on the cross sectional area of the conductors

$$c_8 = \mathrm{gtn}\left(a_c, a_{cmn}\right) \tag{6.12}$$

where $a_{cmn}$ is the minimum allowed conductor cross sectional area.

An iterative Newton-Raphson nonlinear solver is applied to calculate the $B_{st}(\phi_{sm})$. The solver must converge to ensure a valid result. Thus a constraint

$$c_{9,op} = c_{\lambda} \tag{6.13}$$

is applied, where $c_{\lambda}$ is 1 if the solver converges, and 0 if it does not.

The PMSM mass is limited to ensure the generator design is in a range of interest. The constraint is expressed as

$$c_{10} = \text{ltn}\left(M_G, M_{lim}\right) \tag{6.14}$$

where $M_{lim}$ is the maximum allowed generator mass.

Similar to the mass constraint, a length constraint is imposed on the PMSM

$$c_{11} = \text{ltn}\left(l, l_{lim}\right) \tag{6.15}$$

where $l_{lim}$ is the maximum allowed generator length.

To ensure the PMSM is not operated in high saturation, four flux density constraints are imposed on the design. In particular,

$$c_{12,op} = \text{ltn}\left(B_{stmx}, B_{slim}\right) \tag{6.16}$$

$$c_{13,op} = \text{ltn}\left(B_{sbmx}, B_{slim}\right) \tag{6.17}$$

$$c_{14,op} = \text{ltn}\left(B_{rbtmx}, B_{rlim}\right) \tag{6.18}$$

$$c_{15,op} = \text{ltn}\left(B_{rbrmx}, B_{rlim}\right) \tag{6.19}$$

where $B_{stmx}$ is the stator teeth maximum flux density, $B_{sbmx}$ is the stator backiron maximum flux density, $B_{rbtmx}$ is the rotor backiron maximum tangential flux density, and $B_{rbrmx}$ is the rotor backiron maximum radial flux density. The $B_{slim}$ and $B_{rlim}$ are steel flux density limit for the stator and rotor, respectively. The constraints $c_{12,op}$ - $c_{15,op}$ are evaluated at zero current to make sure the unexcited machine is not highly saturated and at each operating point.

To avoid demagnetizing permanent magnets of the PMSM, the field intensity of the permanent magnet is limited by

$$c_{16,op} = \text{ltn}\left(\frac{H_{mn}}{H_{ci}}, k_m\right) \tag{6.20}$$

where $H_{mn}$ is the most negative field intensity in a positively magnetized permanent magnet, $H_{ci}$ is the material's intrinsic coercitivity, and $k_m$ is the demagnetization safety factor which is less than 1. Similar to $c_{12,op}$ - $c_{15,op}$, this constraint is evaluated at zero current and at each operating point.

For thermal reasons, the PMSM winding current density is limited. The constraint is expressed as

$$c_{17} = \text{ltn}\left(\frac{\max(\mathbf{I}_s)}{a_c}, J_{max}\right) \tag{6.21}$$

where $\max(\bullet)$ is a function which will return the maximum value of its argument, $\mathbf{I}_s$ is a vector of winding current rms value at each operating point, and $J_{max}$ is the current density limit.

The eighteenth to twenty-eighth constraints are related to the converter. First, the rectifier operating mode [24] is limited to ensure the waveform reconstruction algorithm is applicable to the design. Due to the existence of commutating inductance, mode 0 is not considered herein. In mode 1 and mode 2, the rectifier dc voltage waveform is continuous and always larger than zero. In mode 3, the rectifier dc voltage waveform is discontinuous and the rectifier is shorting. Thus the rectifier operating mode is limited to mode 1 and mode 2.

$$c_{18,op} = \left(\theta_{mode} = 1\right) \text{or} \left(\theta_{mode} = 2\right) \tag{6.22}$$

where $\theta_{mode}$ is the rectifier operating mode.

To achieve a valid dc-dc buck converter design, the input dc bus voltage is required to be higher than the output dc bus voltage. Thus a constraint is imposed on the rectifier dc bus voltage

$$c_{19,op} = g\text{tn}\left(\overline{v}_r, v_{r,min}\right) \tag{6.23}$$

where $v_{r,min}$ is the rectifier dc voltage lower limit.

Four constraints are imposed here to ensure the voltage and current ripple of the converter filters are within desired levels. These are

$$c_{20,op} = \text{ltn}\left(\Delta v_{cin}, \delta_{vcin}\overline{v}_{cin,fl}\right) \tag{6.24}$$

$$c_{21,op} = \text{ltn}\left(\Delta i_r, \delta_{ir}\overline{i}_{r,fl}\right) \tag{6.25}$$

$$c_{22,op} = \text{ltn}\left(\Delta v_{out}, \delta_{vout}\overline{v}_{out,fl}\right) \tag{6.26}$$

$$c_{23,op} = \text{ltn}\left(\Delta i_l, \delta_{il}\overline{i}_{l,fl}\right) \tag{6.27}$$

where $\delta_{vcin}$, $\delta_{ir}$, $\delta_{vout}$, and $\delta_{il}$ are the ripple specifications of input capacitor voltage, input inductor current, output capacitor voltage, and output inductor current, respectively, $\overline{v}_{cin,fl}$, $\overline{i}_{r,fl}$, $\overline{v}_{out,fl}$, and $\overline{i}_{l,fl}$ are the corresponding steady state values at the full load operating point. The four constraints are evaluated at each operating point.

To ensure the converter is operated in the continuous conduction mode [23], two constraints are imposed on the input inductor current ripple and output inductor current ripple. Specifically,

$$c_{24,op} = \text{gtn}\left(i_{rmn,op}, 0\right) \tag{6.28}$$

$$c_{25,op} = \text{ltn}\left(\Delta i_l, 2\overline{i}_{l,op}\right) \tag{6.29}$$

where $i_{rmn,op}$ is the minimum dc rectifier current at each operating point which is obtained from Section 4.3, and $\bar{i}_{l,op}$ is the steady state value of output inductor current at each operating point. The two constraints are evaluated at each operating point.

The polypropylene capacitor's lifetime is related to its operating temperature. To ensure a desired lifetime, the temperature rise of the polypropylene capacitors are limited by

$$c_{26,op} = \text{ltn}\left(\Delta T_{cin}, \Delta T_{max}\right) \tag{6.30}$$

$$c_{27,op} = \text{ltn}\left(\Delta T_{cout}, \Delta T_{max}\right) \tag{6.31}$$

where $\Delta T_{cin}$ and $\Delta T_{cout}$ are the temperature rise of input capacitor and output polypropylene capacitor, respectively. The $\Delta T_{max}$ is the allowed capacitor temperature rise.

To ensure a desired lifetime of the electrolytic capacitor, the RMS value of the ripple current passing through $C_{oute}$ is constrained as

$$c_{28,op} = \text{ltn}\left(I_{rms,Coute}, I_{coute,mx}\right) \tag{6.32}$$

where $I_{coute,mx}$ is the maximum RMS value of the $C_{oute}$ ripple current.

In Chapter 2, the semiconductor thermal analysis is performed to calculate heat sink mass. Using that procedure, it is possible to achieve a heatsink-to-air thermal resistance $R_{s,ha}$ which is less than zero and thus not achievable. To avoid this, a constraint is imposed on $R_{s,ha}$. Thus

$$c_{29} = \text{gtn}\left(R_{s,ha}, 0\right) \tag{6.33}$$

In Chapter 5, the system small signal stability is determined based on the system eigenvalue distribution. The following constraint is added to ensure the system is stable.

$$c_{30} = c_{st} \tag{6.34}$$

The variable $c_{st}$ is 1 if the equilibrium point is stable, and 0 if it is not.

The disturbance rejection analysis is set forth in Chapter 5. A constraint is imposed on the maximum output impedance $Z_{out,mx}$ over a desired disturbance frequency range to ensure the system has good disturbance rejection capability. The constraint is expressed as

$$c_{31} = \text{ltn}\left( Z_{out,mx}, \delta_Z \frac{\bar{v}_{out}^2}{P_{out}} \right) \tag{6.35}$$

where $\delta_Z$ is the output impedance specification.

Among all the constraints applied to the system optimization, the constraints $c_1$ - $c_8$, $c_{10}$, $c_{11}$, $c_{17}$ and $c_{29}$ - $c_{31}$ are applied only once. The constraints $c_{9,op}$, $c_{12,op}$ - $c_{16,op}$ are applied to the PMSM design at zero current and at each operating point. The constraints $c_{18,op}$ - $c_{28,op}$ are applied to the converter design at each operating point. Thus the total number of constraints applied for a design is expressed as

$$N_C = 20 + 17 N_{op} \tag{6.36}$$

where $N_{op}$ is the number of operating points.

The next step is to determine the optimization metrics. The system mass $M$ and the system aggregate loss $P_a$ are selected herein as the two metrics of interest. The system mass includes the

generator electromagnetic mass $M_G$, the input and output inductor mass $M_{Lin}$, $M_{Lout}$, the input capacitor mass $M_{Cin}$, output electrolytic capacitor mass $M_{Coute}$, output polypropylene capacitor mass $M_{Coutp}$, and the heatsink mass $M_H$. The system mass is expressed as

$$M = M_G + M_{Lin} + M_{Cin} + M_{Lout} + M_{Coute} + M_{Coutp} + M_H \tag{6.37}$$

The system loss at each operating point includes the generator loss $P_G$, the input and output PMI dc loss $P_{Lin}$, $P_{Lout}$, the rectifier loss $P_{rec,cd}$, the dc-dc converter semiconductor conduction and switching loss $P_{t,cd}$, $P_{t,sw}$, $P_d$. The system loss at each operating point is expressed as

$$P_{op} = P_G + P_{Lin} + P_{Lout} + P_{rec,cd} + P_{t,cd} + P_{t,sw} + P_d \tag{6.38}$$

The system aggregate loss is calculated by

$$P_a = \sum_{op=1}^{N_{op}} w_{op} P_{op} \tag{6.39}$$

where $w_{op}$ is the weighting for each operating point.

The multi-dimensional fitness function evaluated for each design is defined as

$$\mathbf{f}(\boldsymbol{\theta}_s) = \begin{cases} \varepsilon\left(\dfrac{C_S - N_C}{N_C}\right)\begin{bmatrix}1\\1\end{bmatrix} & C_S < C_I \\ \begin{bmatrix} M^{-1} & P_a^{-1} \end{bmatrix}^T & C_S = N_C \end{cases} \tag{6.40}$$

where $\varepsilon$ is a small number ($10^{-6}$), $C_I$ is the number of imposed constraints, and $C_S$ is the number of satisfied constraints. Initially $C_I = C_S = 0$. After imposing n$^{\text{th}}$ constraint $c_n$, both $C_I$ and $C_S$ are updated, where $C_I = C_I + 1$ and $C_S = C_S + c_n$. If a constraint is violated which will lead

$C_S < C_I$, the rest of the constraints won't be evaluated and the algorithm will stop at an early stage in code to improve computational efficiency. In this case the fitness function will return a small negative number. The Pseudo-code of this constraint testing procedure is given in Table 6.1. If all constraints are satisfied, the fitness function will return the reciprocal value of system mass and system loss. The fitness function evaluation Pseudo-code is shown in Table 6.2.

Table 6.1 Pseudo Code for Testing Constraints Satisfied Against Constraints Imposed

1. Update $C_S$
2. Update $C_I$
3. If ($C_S < C_I$)

$$\mathbf{f}(\boldsymbol{\theta}_s) = \varepsilon\left(\frac{C_S - N_C}{N_C}\right)\begin{bmatrix}1\\1\end{bmatrix}$$

return

end

Table 6.2 Pseudo Code for Evaluating Fitness Function

1. Initialize constraint count to $N_C = 20 + 17N_{op}$

   Assign PMSM material properties (Section 4.1.3).
   Calculate machine geometry (Section 4.1.1). Calculate cogging torque peak value (Section 4.1.9).
   Calculate winding parameters (Section 4.1.2). Evaluate constraints $c_1 - c_8$.

   Test constraints (Table 6.1).
   Calculate lumped parameter model (Section 4.1.5). Evaluate constraint $c_{9,op}$.

   Calculate PMSM mass $M_G$. Evaluate constraint $c_{10}$ and $c_{11}$. Test constraints (Table 6.1).

   Perform PMSM magnetic field analysis at no current condition (Section 4.1.4 and 4.1.6). Evaluate constraints $c_{12,op} - c_{16,op}$. Test constraints (Table 6.1).

   Perform output capacitor modeling based on $v_{out}$ (Section 3.2 and Section 3.3).
2. Set $n_{op} = 1$
3. While $n_{op} < N_{op}$
   i. Perform system steady state analysis (Section 5.1). Calculate $P_{Lin}$, $P_{Lout}$, $P_{t,cd}$, $P_{t,sw}$, and $P_d$. Evaluate constraints $c_{18,op}$ and $c_{19,op}$. Test constraints (Table 6.1).
   ii. Perform PMSM magnetic field analysis at operating point $n_{op}$ (Section 4.1.4 and 4.1.6). Calculate $P_G$. Evaluate constraints $c_{9,op}$, and $c_{12,op} - c_{16,op}$. Test constraints (Table 6.1).
   iii. Perform input capacitor modeling based on $\bar{v}_r$ at full load operating point (Section 3.2). Calculate the input filter ripple (Section 4.3). Calculate $P_{rec}$. Evaluate constraints $c_{20,op} - c_{25,op}$. Test constraints (Table 6.1).
   iv. Calculate capacitor RMS current (Section 5.1.4) and temperature rise (Section 3.2). Evaluate constraints $c_{26,op}$ - $c_{28,op}$. Test constraints (Table 6.1). Calculate $P_{op}$.
   v. $n_{op} = n_{op} + 1$
4. Calculate $P_a$. Evaluate constraint $c_{17}$. Calculate $M_{Lin}$ and $M_{Lout}$ based on full load operating point current (Section 3.1.6). Calculate $M_H$ based on full load operating point semiconductor loss (Section 2.5). Evaluate constraint $c_{29}$. Test constraints (Table 6.1).
5. Perform the stability analysis and disturbance rejection analysis (Section 5.3). Evaluate constraints $c_{30}$ and $c_{31}$. Test constraints (Table 6.1).
6. Compute fitness function and return.

## 6.3 Case Study

With the design space, optimization constraints, and fitness function defined, a case study is conducted to demonstrate the design methodology. Table 6.3 lists the design variables and their range for a 10 kW, 750V dc generation system. In Table 6.3, the encoding type is defined in Chapter 3 and defines how the design variables are searched in their respective range. The system specifications, power converter design specifications, and PMSM design specifications are listed in Table 6.4, Table 6.5, and Table 6.6, respectively. Considering the system voltage and current rating, the Si semiconductors applied to the system design are Micorsemi APT13GP120B IGBT and Powerex CS241250D diode. The Si semiconductor specifications are given in Table 6.7. The IGBT is used for transistors $T_1$ and $T_2$. The diode is used for the rectifier diodes and for dc-dc converter diodes $D_1$ and $D_2$.The conduction and switching loss parameters of these devices can be found in Chapter 2. The analysis parameters used in Chapter 4 for the uncontrolled generation subsystem design are listed in Table 6.8. The system steady state analysis parameters are listed in Table 6.9. The frequency range of the disturbance rejection analysis is taken to be 1-1000Hz which is the most significant current disturbance frequency. In this frequency range, the linearized system's impedance must be less than the impedance specification to avoid a large voltage deviation.

The population size and the generation size of the GA are both set as 2000. The optimization yields a Pareto-optimal front (a set of designs characterizing the trade-off between, in this case, system mass and system loss). Each individual of the Pareto-optimal front represents a complete system design.

Table 6.3 Design Space

| Gene | Parameter | Min. | Max. | Encoding | Units |
|---|---|---|---|---|---|
| 1 | $P_P$ | 2 | 7 | Int | N/A |
| 2 | $r_{st}$ | 1.4 | 36.25 | Log | cm |
| 3 | $d_{rb}$ | 0.1 | 15 | Log | cm |
| 4 | $d_m$ | 0.1 | 5 | Log | cm |
| 5 | $g$ | 1 | 2.5 | Lin | mm |
| 6 | $d_{tb}$ | 0.1 | 5 | Log | cm |
| 7 | $\alpha_t$ | 0.1 | 0.9 | Lin | N/A |
| 8 | $d^*_{sb}$ | 0.1 | 5 | Log | cm |
| 9 | $\alpha_{pm}$ | 0.1 | 0.9 | Lin | N/A |
| 10 | $B^*_r$ | 0.5 | 1.3 | Lin | T |
| 11 | $l$ | 1 | 20 | Lin | cm |
| 12 | $N^*_{s1}$ | 1 | $1.0\cdot10^4$ | Log | cond/rad |
| 13 | $f_{sw}$ | $1.0\cdot10^3$ | $1.0\cdot10^6$ | Log | Hz |
| 14 | $L_{in}$ | $1.0\cdot10^{-6}$ | $1.0\cdot10^{-1}$ | Log | H |
| 15 | $J_{Lin}$ | $7.5\cdot10^4$ | $7.5\cdot10^6$ | Log | $A/m^2$ |
| 16 | $L_{out}$ | $1.0\cdot10^{-6}$ | $1.0\cdot10^{-1}$ | Log | H |
| 17 | $J_{Lout}$ | $7.5\cdot10^4$ | $7.5\cdot10^6$ | Log | $A/m^2$ |
| 18 | $C_{in}$ | $1.0\cdot10^{-6}$ | $1.0\cdot10^{-2}$ | Log | F |
| 19 | $C_{outp}$ | $1.0\cdot10^{-6}$ | $1.0\cdot10^{-2}$ | Log | F |
| 20 | $C_{oute}$ | $1.0\cdot10^{-6}$ | $1.0\cdot10^{-2}$ | Log | F |

Table 6.4 System Specifications

| Description | Symbol | Value |
|---|---|---|
| Output dc bus voltage | $v_{out}$ | 750 V |
| Number of operating points | $N_{op}$ | 1 |
| Weight of operating point 1 | $w_1$ | 1 |
| Output power at operating point 1 | $P_{out}$ | 10 kW |
| Output impedance constraint criterion | $\delta_Z$ | 0.05 |

Table 6.5 Converter Design Specifications

| Description | Symbol | Value |
|---|---|---|
| Output voltage ripple fraction | $\delta_{vout}$ | 0.001 |
| Output current ripple fraction | $\delta_{il}$ | 0.2 |
| Rectifier dc voltage ripple fraction | $\delta_{vcin}$ | 0.05 |
| Rectifier dc current ripple fraction | $\delta_{ir}$ | 0.2 |
| Rectifier dc voltage lower limit | $v_{r,min}$ | 775 V |
| Rectifier diode forward drop | $v_t$ | 2 V |
| Rectifier commanded firing angle relative to back EMF | $\alpha^*$ | -0.5 |
| Polypropylene capacitor maximum temperature rise | $\Delta T_{max}$ | 30°C |
| Electrolytic capacitor maximum RMS current | $I_{coute,mx}$ | 1.6 A |

Table 6.6 PMSM Design Specifications

| Description | Symbol | Value |
|---|---|---|
| Rotor shaft radius | $r_{rs}$ | 0.01 m |
| Mechanical rotor speed | $\omega_{rm}$ | 9000 RPM |
| Stator material | $m_s$ | JFE 10JNEX900 |
| Rotor material | $m_r$ | JFE 10JNEX900 |
| Conductor material | $m_c$ | Copper |
| Outer radius limit | $r_{ss,lim}$ | 1 m |
| Length limit | $l_{lim}$ | 1 m |
| Maximum mass | $M_{lim}$ | 500 kg |
| Maximum tip speed | $v_{tpmx}$ | 200 m/s |
| Minimum conductor cross sectional area | $a_{cmn}$ | $1 \cdot 10^{-9}$ m$^2$ |
| Cogging torque factor | $\alpha_{cogging}$ | 0.3 |
| Maximum PM aspect ratio | $\alpha_{pmr}$ | 0.5 |
| Maximum tooth aspect ratio | $\alpha_{tar}$ | 10 |
| Slot opening factor | $\alpha_{so}$ | 1.25 |
| Maximum winding current density | $J_{max}$ | $7.5 \cdot 10^6$ A/m$^2$ |
| Winding packing factor | $k_{pf}$ | 0.42 |
| End winding offset | $l_{eo}$ | 0.01 m |
| Demagnetization safety factor | $k_m$ | 0.5 |
| Slots per pole per phase | $n_{spp}$ | 1 |

Table 6.7 Si Semiconductor Specifications

| Specification | APT13GP120B | CS241250D |
|---|---|---|
| Rated Voltage | 1200 V | 1200 V |
| Rated Current | 20 A at Case Temperature = 110 $^o$C | 50 A at Case Temperature = 105 $^o$C |

Table 6.8 Uncontrolled Generation System Analysis Parameters

| Description | Symbol | Value |
|---|---|---|
| Number of rotor position considered | $J$ | 20 |
| Number of interpolated positions for one slot-tooth span | $N_{ppst}$ | 100 |
| Number of harmonics considered in spatial harmonic analysis | $N_h$ | 2 |
| Number of harmonics considered in temporal harmonic analysis | $N_{hc}$ | 10 |
| Number of harmonics considered in rectifier dc current | $N$ | 8 |

Table 6.9 Steady State Analysis Parameters

| Description | Symbol | Value |
|---|---|---|
| Maximum iteration times | $k_{max}$ | 20 |
| Maximum duty cycle error | $d_{e,max}$ | 0.0001 |
| Maximum voltage error | $v_{e,max}$ | 0.01 |

## 6.4 Case Study Design Results

The case study was run three times (Study 1, Study 2, and Study 3) with the same genetic algorithm parameters to gain confidence that the optimization converged. The Pareto-optimal fronts of the three runs are shown in Fig. 6.1. As can be seen the optimization seems to have converged. The results of Study 1 are selected for investigation.

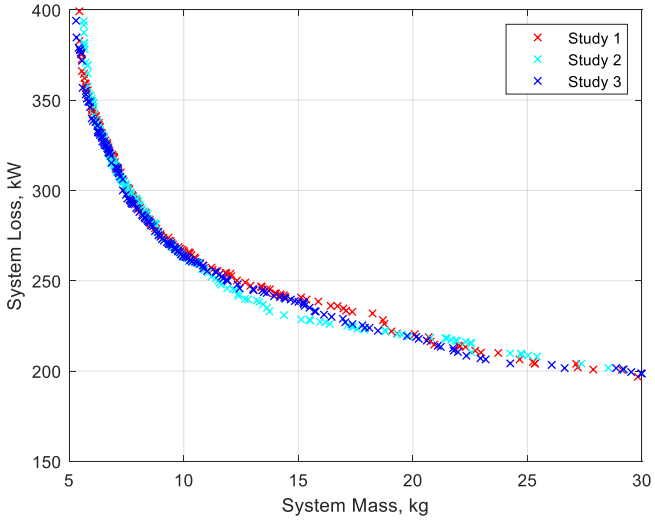


Fig. 6.1 Convergence Study

The gene distribution is shown in Fig. 6.2 for the final population of designs. The genes are ordered as listed in Table 6.3 and are normalized between 0 and 1. The genes are sorted by the system mass which means that the genes of designs with higher mass are toward the left of the parameter window, and the genes with lower mass are toward the right. The mappings between the genes of Fig. 6.2 and the design variables are listed in Table 6.10 for reader's convenience.

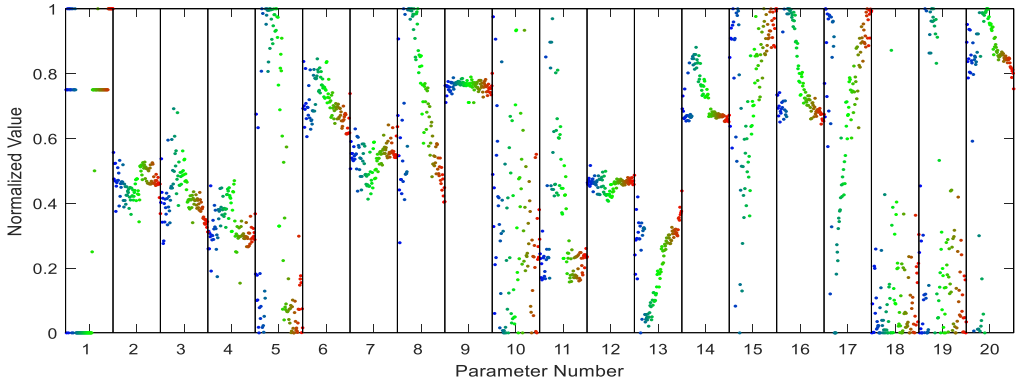


Fig. 6.2 Gene Distribution of Study 1

Table 6.10 Mapping between Gene and Design Variable

| | | | | | | | | | |
|---|---|---|---|---|---|---|---|---|---|
| 1 | 2 | 3 | 4 | 5 | 6 | 7 | 8 | 9 | 10 |
| $P_P$ | $r_{st}$ | $d_{rb}$ | $d_m$ | $g$ | $d_{tb}$ | $\alpha_t$ | $d_{sb}^*$ | $\alpha_{pm}$ | $B_r^*$ |
| 11 | 12 | 13 | 14 | 15 | 16 | 17 | 18 | 19 | 20 |
| $l$ | $N_{s1}^*$ | $f_{sw}$ | $L_{in}$ | $J_{Lin}$ | $L_{out}$ | $J_{Lout}$ | $C_{in}$ | $C_{outp}$ | $C_{oute}$ |

In Fig. 6.2, gene 1 to gene 12 are associated to the PMSM design which corresponding to the design variables $P_P$ to design variable $N_{s1}^*$ in Table 6.10. The design variable $P_P$ converged to the highest pole count as mass decreased since the higher pole count requires thinner backiron which helps reducing the machine mass. The PMSM dimension variables $r_{st}$, $d_{rb}$, $g$, $d_m$, $d_{tb}$, $d_{sb}^*$, and $l$ decreased as mass decreased since a smaller machine volume means a smaller machine mass. The tight convergence of $\alpha_{pm}$ compared to other design variables is due to the cogging torque constraint. The $B_r^*$ did not converge as well as other design variables since the permanent magnet is selected from a catalog which is a limited set.

Gene 13 to gene 20 are associated with the converter design which corresponding to the design variables $f_{sw}$ to $C_{oute}$ in Table 6.10. The $f_{sw}$ increases as the system mass decreases since higher switching frequency facilitates smaller input and output filters which means smaller $L_{in}$, $L_{out}$, $C_{in}$, $C_{outp}$, and $C_{oute}$. The $J_{Lin}$ and $J_{Lout}$ increases as mass decreases since the high current density will reduce the inductor winding mass; The $C_{in}$ clusters at the lower part of the range which implies the input filter doesn't require large capacitance to filter the voltage ripple. The $C_{outp}$ and $C_{oute}$ have the same design space range ($1\mu F$ - $10000\mu F$), the fact that $C_{oute}$ converged to a

much higher value compared to $C_{outp}$ indicates that using the electrolytic capacitor as the output capacitor is advantageous for most of the designs. This result is consistent with the fact that electrolytic capacitors have higher energy density compared to polypropylene capacitors. The comparison of electrolytic capacitor and polypropylene capacitor will be discussed more thoroughly in the next section.

## 6.5 Comparison between WBG Devices and Silicon Devices

One of the objectives of this work is to quantify the advantage of WBG devices over silicon devices. To achieve this, a SiC semiconductor based case study is compared to the Si based case study conducted in Section 6.4. The SiC semiconductors considered herein include Cree C2M0080120D MOSFETs and Cree C4D20120A diodes. The SiC semiconductor specifications are given in Table 6.11. The MOSFET is used for transistors $T_1$ and $T_2$. The diode is used for the rectifier diodes and for dc-dc converter diodes $D_1$ and $D_2$.The conduction and switching loss parameters of these devices can be found in Chapter 2. Four studies are performed here to assess the relative merits of the two technologies. They have the same system design specifications. The four studies are (1) Si based system design with a disturbance rejection requirement, (2) Si based system design without a disturbance rejection requirement, (3) SiC based system design with a disturbance rejection requirement, and (4) SiC based system design without a disturbance rejection requirement. The studies without disturbance rejection requirement are conducted to demonstrate the effect of a disturbance rejection requirement on the system design, especially with regard to the system's passive components.

Table 6.11 SiC Semiconductor Specifications

| Specification | C2M0080120D MOSFET | C4D20120A Diode |
|---|---|---|
| Rated Voltage | 1200 V | 1200 V |
| Rated Current | 24 A at Case Temperature = 100 $^{o}$C | 20 A at Case Temperature = 150 $^{o}$C |

The Pareto optimal fronts of four studies are shown in Fig. 6.3. To demonstrate the difference between the four fronts more clearly, system designs that have mass between 4 kg and 12 kg are plotted in Fig. 6.4. In Fig. 6.3 and Fig. 6.4, 'w/o DR' denotes the case study without a disturbance rejection requirement, and 'w DR' denotes the case study with a disturbance rejection requirement. The optimization results show that the SiC based system designs dominate the Si based system designs. This advantage becomes more pronounced when a disturbance rejection requirement is included.

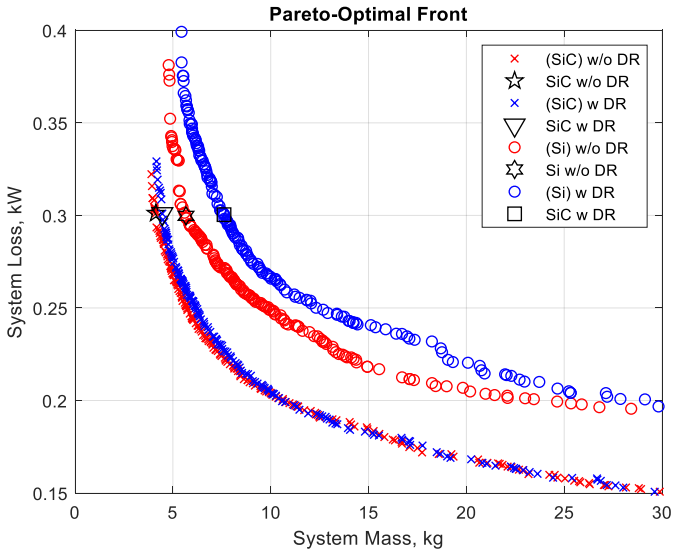


Fig. 6.3 Pareto Optimal Front Comparison

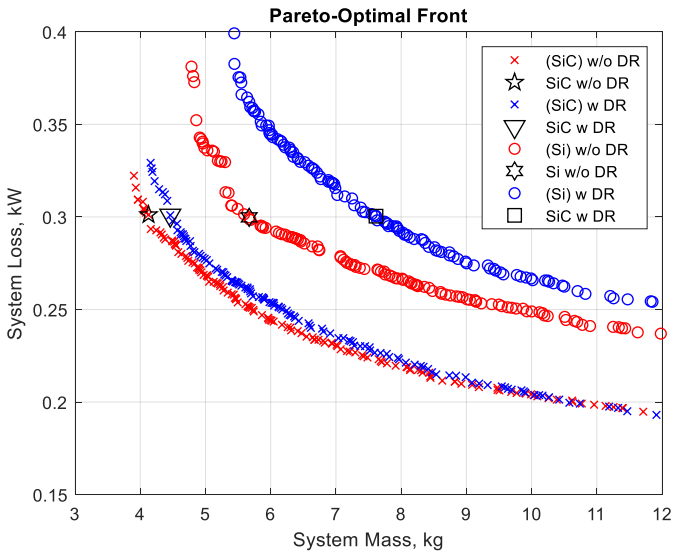


Fig. 6.4 Pareto Optimal Front Comparison

Fig. 6.5 - Fig. 6.8 show the gene distribution of the four studies. The distribution of the first twelve genes are similar for the four studies which indicates that the semiconductor type has small impact on the PMSM optimization. The $f_{sw}$ (gene 13) varies substantially between the four studies. Compared to the Si based case studies, the switching frequency of the SiC based case studies converges to the higher part of the range. It is also noticed that the case studies that have the disturbance rejection analysis have higher switching frequency compared to the case studies that do not have the disturbance rejection analysis. The $L_{in}$ (gene 14) is consistent between the four studies since the input inductor size is dominated by the rectifier dc current ripple. The same trend can be found in $C_{in}$ (gene 18). The $J_{Lin}$ (gene 15) and $J_{Lout}$ (gene 17) follow the same trends for the four studies since the inductor current density always tend to converge to the highest allowed value to reduce mass. It can be observed that the $L_{out}$ (gene 16) of the SiC based case studies converged to a lower part of the range compared to the Si based case studies which is due to the higher switching frequency the SiC based case studies obtained. For the studies without a

disturbance rejection requirement, $C_{oute}$ (gene 20) tends to converge to the lowest part of the region. This phenomenon indicates that the polypropylene capacitor is more effective as a filter capacitor for both Si based study and SiC based study. In the Si based study, the large ESR of the electrolytic capacitor makes it difficult to meet the output voltage ripple requirement. In the SiC based study, the disadvantage of electrolytic capacitor is its frequency derating property. For the studies with a disturbance rejection requirement, $C_{oute}$ (gene 20) converges to a higher part of the range compared to $C_{outp}$ (gene 19) which suggests the use of the electrolytic capacitor as the energy storage capacitor to improve the system's disturbance rejection capability. This is mainly due to the electrolytic capacitor's high energy density.

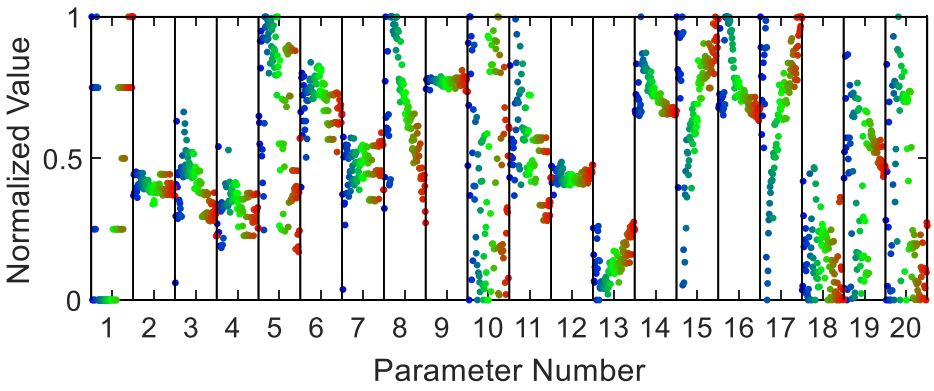


Fig. 6.5 Gene Distribution of Si Based Case Study without a Disturbance Rejection Requirement

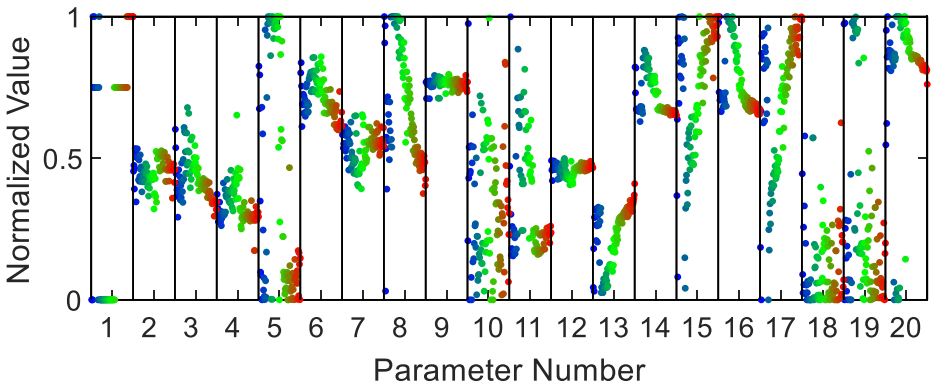


Fig. 6.6 Gene Distribution of Si Based Case Study with a Disturbance Rejection Requirement

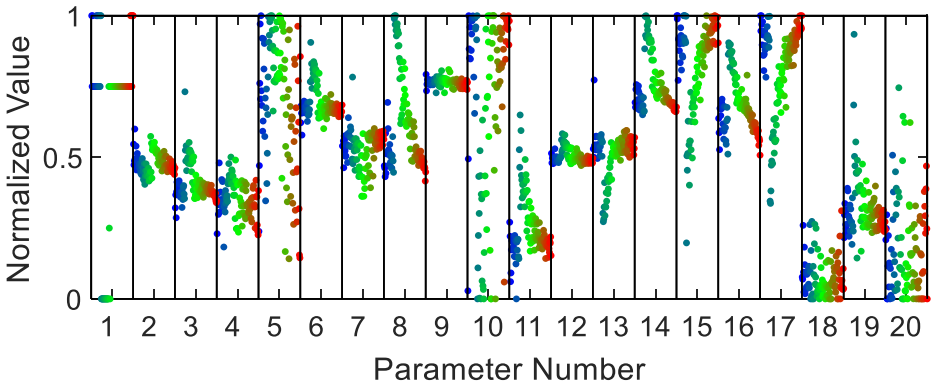


Fig. 6.7 Gene Distribution of SiC Based Case Study without a Disturbance Rejection Requirement

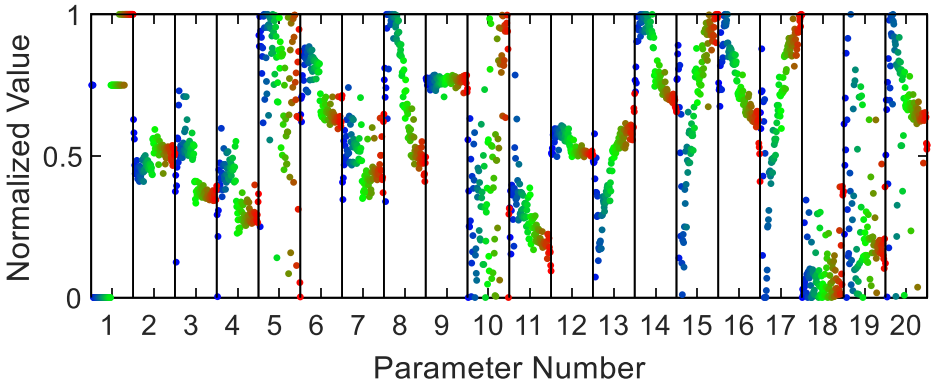


Fig. 6.8 Gene Distribution of SiC Based Case Study with a Disturbance Rejection Requirement

The switching frequency versus system mass for the four studies is shown in Fig. 6.9. The studies with a disturbance rejection requirement utilize a higher switching frequency since the higher switching frequency leads to a faster control which benefits the system's disturbance rejection capability. The SiC based system designs use much higher frequency (up to 120 kHz) compared to the Si based system designs (up to 20 kHz) since the SiC semiconductors have lower losses and the rated junction temperature is higher.

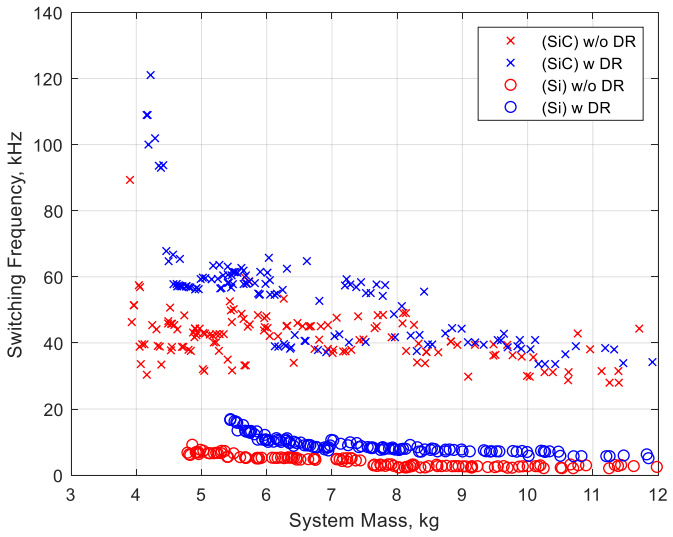


Fig. 6.9 Switching Frequency versus System Mass

Four example designs are picked from Fig. 6.4 for investigation. Design 'Si w/o DR' (Si based case study without a disturbance rejection requirement), design 'Si w DR' (Si based case study with a disturbance rejection requirement), design 'SiC w/o DR' (SiC based case study without a disturbance rejection requirement) and design 'SiC w DR' (SiC based case study with a disturbance rejection requirement) are selected from four Pareto-optimal fronts, respectively. The system efficiency of each of the selected designs is close to 97% which is equivalent to a system

loss of 300W. The design parameters of each design are listed in Table 6.12. In Table 6.12, $M_C$ is the converter mass, and $P_C$ is the converter loss.

From Table 6.12, the ‘SiC w DR’ design system mass is 58.6% of the ‘Si w DR’ design system mass. The ‘SiC w/o DR’ design system mass is 72.8% of the ‘Si w/o DR’ design system mass. This shows that the advantage of SiC increases in the presence of a disturbance rejection requirement. This is due to the control strategy applied in the system design. Since the controller gains are tied to the switching frequency, the higher switching frequency will give the system faster response thus smaller passive components can be applied.

It is interesting to compare the converter mass and loss between the case studies. Compared to the Si based converter design, the mass reduction of the SiC based converter design is mainly due to the increase in switching frequency which results in a reduced size for the output inductor and output capacitor. The ‘SiC w DR’ design converter loss is 67.4% of the ‘Si w DR’ design converter loss. The loss reduction is due to the extremely low switching loss and relatively low conduction loss in the SiC diode. The loss reduction also contributes to the heat sink mass reduction.

Since the four case studies have the same loss, the high converter loss of the Si based designs leads to low PMSM loss. In order to meet the low loss requirement, the number of pole pair of the PMSM of the Si based design drops to six to reduce resistive loss since the number of stator slots drops which decreases the phase resistance.

Table 6.12 Example Designs

| Parameter | SiC w/o DR | SiC w DR | Si w/o DR | Si w DR |
|---|---|---|---|---|
| $M$(kg) | 4.126 | 4.46 | 5.67 | 7.614 |
| $P$(W) | 301.2 | 300.9 | 299.8 | 300.4 |
| $M_C$(kg) | 0.4561 | 0.7796 | 0.8885 | 2.628 |
| $P_C$(W) | 77.95 | 82.75 | 108 | 122.7 |
| $M_G$(kg) | 3.67 | 3.681 | 4.781 | 4.987 |
| $P_G$(W) | 223.2 | 218.2 | 191.7 | 177.7 |
| $P_p$ | 7 | 7 | 6 | 6 |
| $r_{st}$(cm) | 5.465 | 6.662 | 5.114 | 6.458 |
| $d_{rb}$(mm) | 4.993 | 5.613 | 5.314 | 6.995 |
| $d_m$(mm) | 2.946 | 3.515 | 4.329 | 2.927 |
| $g$(mm) | 1.424 | 2.241 | 1.569 | 1 |
| $d_{tb}$(mm) | 14.13 | 11.46 | 14.82 | 13.98 |
| $\alpha_t$ | 56.56% | 50.06% | 53.67% | 54.91% |
| $d_{sb}$(mm) | 5.085 | 5.41 | 5.975 | 8.214 |
| $\alpha_{pm}$ | 71.14% | 73.13% | 72.16% | 70.9% |
| $B_r$(T) | 1.3 | 1.233 | 0.7843 | 0.6371 |
| $l$(cm) | 5.316 | 4.576 | 6.674 | 4.946 |
| $N_{s1}$ | 81.17 | 106.3 | 67.82 | 76.55 |
| $f_{sw}$(kHz) | 39.852 | 67.799 | 5.418 | 8.343 |
| $L_{in}$(mH) | 1.947 | 2.94 | 1.959 | 2.246 |
| $J_{Lin}$(A/mm$^2$) | 7.5 | 7.5 | 4.922 | 4.46 |
| $L_{out}$(mH) | 0.3879 | 1.173 | 1.461 | 2.711 |
| $J_{Lout}$(A/mm$^2$) | 6.756 | 7.5 | 6.527 | 5.841 |
| $C_{in}$(μF) | 2 | 2 | 2 | 2 |
| $C_{outp}$( μF) | 15 | 4 | 80 | 20 |
| $C_{oute}$( μF) | 10.18 | 170.5 | 0.5207 | 1174 |

Fig. 6.10 and Fig. 6.11 illustrate system mass stacked bar plots of the designs in Table 6.12. From Fig. 6.10, it can be seen that the generator mass dominates the system mass for the four designs. Interestingly, SiC semiconductors yield a modest decrease in generator size which is due to their impact on converter loss. Since these designs all have the same loss, reducing converter loss allows the machine loss to increase which translates to reduced machine size. This phenomenon is observed in Table 6.12 by comparing $P_C$ and $P_G$ through four example designs. Unexpectedly, while in percentage terms the machine sizes were similar; the difference that did exist between the generators was a significant contributor to the difference between the total system masses.

To clearly demonstrate the converter mass difference between the four designs, Fig. 6.10 is zoomed in at mass range 4 kg-10 kg and plotted as Fig. 6.11. It can be seen that the mass of the input inductor is relatively consistent across all designs. The input capacitor made an almost insignificant contribution to the total system masses in all cases. In the output stage, the mass of the output inductor was similar for all SiC designs; though these were smaller than for the Si based designs.

The output polypropylene capacitor contributed to the mass of the 'Si w/o DR' design since the polypropylene capacitor's small ESR make it favorable as the filter capacitor. For the other three designs, the output polypropylene capacitor contribute negligible mass. There are two reasons behind this phenomenon. In the 'Si w DR' design, the electrolytic capacitor is preferred over the polypropylene capacitor due to its high energy density. The ESR of a high capacitance electrolytic capacitor is small thus the electrolytic capacitor functions as a filter capacitor as well as an energy storage capacitor. In SiC based system designs, the polypropylene capacitor is used as the filter capacitor. However, due to the high switching frequency, only a small filter capacitor

is required. The output electrolytic capacitor contributed little mass to the total system mass for those designs without a dynamic rejection requirement; but did contribute to the mass of those designs in which a dynamic rejection requirement was present. It can also be seen that the heatsink mass is reduced by going from Si to SiC.

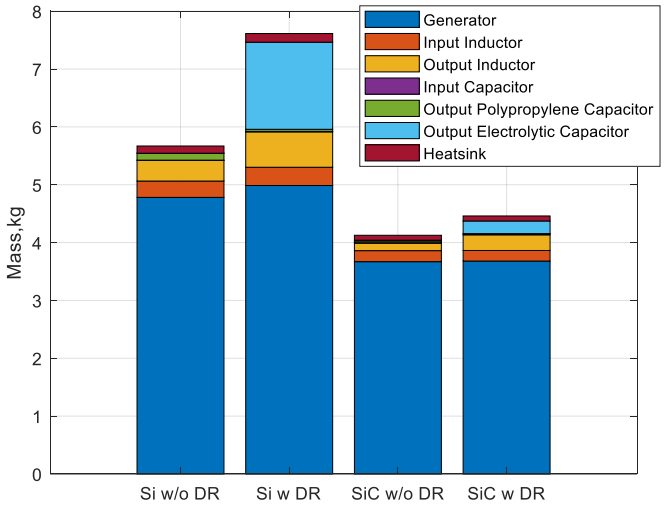


Fig. 6.10 System Mass of the Example Designs

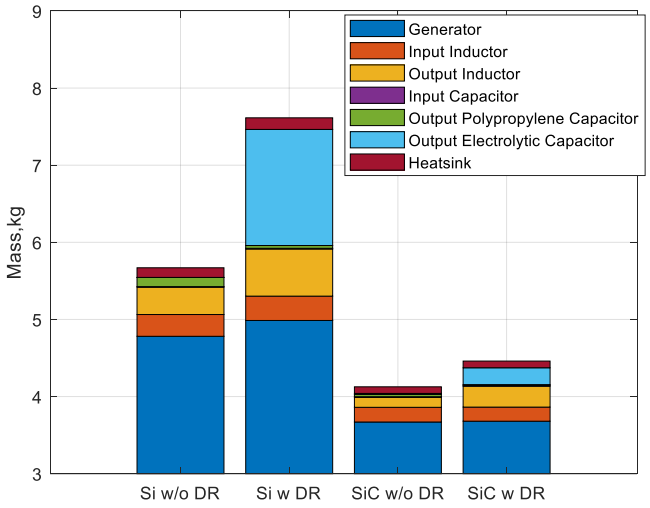


Fig. 6.11 System Mass of the Example Designs

To evaluate the disturbance rejection capability of the four example designs, a time domain simulation is implemented in Matlab/Simulink. The waveform level model is developed based on the model shown in Fig. 6.12. The PMSM equivalent circuit model parameters used for the four designs are listed in Table 6.13. The system disturbance is a load step change which is applied to the system at 0.5s to increase the system output power from 1 kW to 10 kW. The transient response of the system output voltage $v_{out}$ is shown in Fig. 6.13 – Fig. 6.16. From the transient response of the four designs, it is clear that the designs without a disturbance rejection requirement have larger voltage deviation (150 V for Si design and SiC design) compared to the designs which have a disturbance rejection requirement (10 V for both the Si design and SiC design). The results validate the effectiveness of the disturbance rejection analysis proposed in this work.

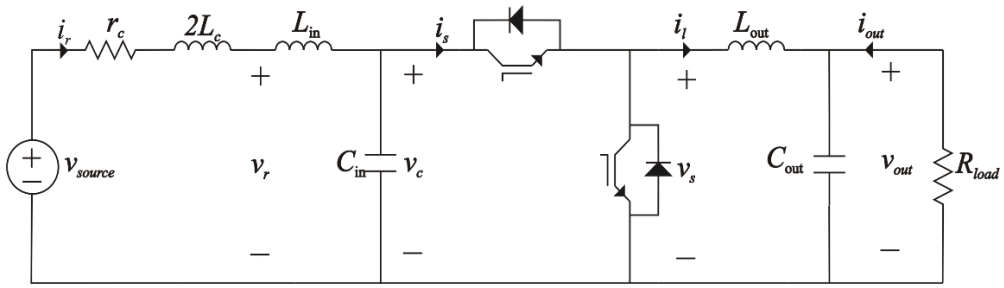


Fig. 6.12 Waveform Level Model

Table 6.13 PMSM Equivalent Circuit Model Parameter

| Parameter | SiC w/o DR | SiC w DR | Si w/o DR | Si w DR |
|---|---|---|---|---|
| $v_{source}$ | 892.3 V | 959.5 V | 860.6 V | 906.4 V |
| $r_c$ | 7.657 Ω | 8.954 Ω | 6.250 Ω | 6.808 Ω |
| $L_c$ | $1.1\cdot10^{-3}$ H | $1.2\cdot10^{-3}$ H | $1.0\cdot10^{-3}$ H | $1.1\cdot10^{-3}$ H |

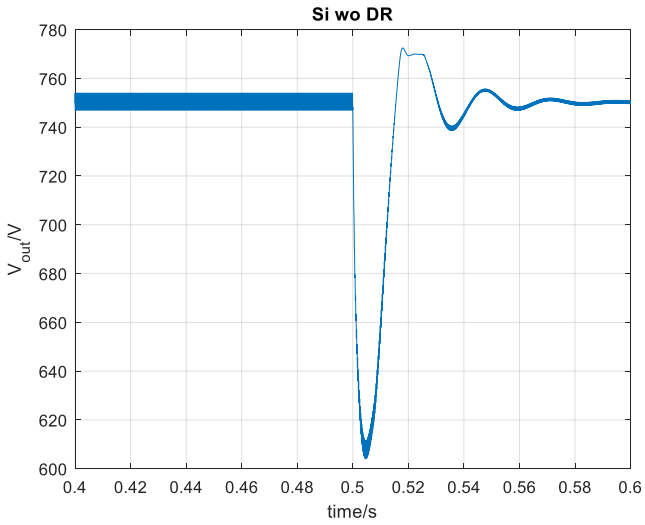


Fig. 6.13 Output Voltage Deviation of ‘Si w/o DR’ Design

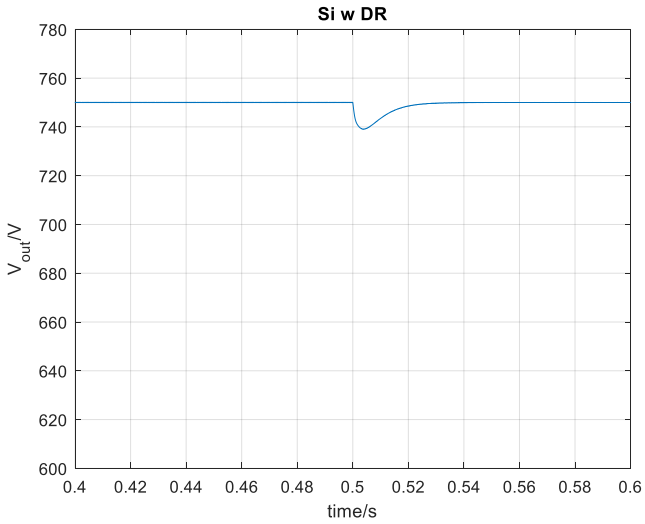


Fig. 6.14 Output Voltage Deviation of ‘Si w DR’ Design

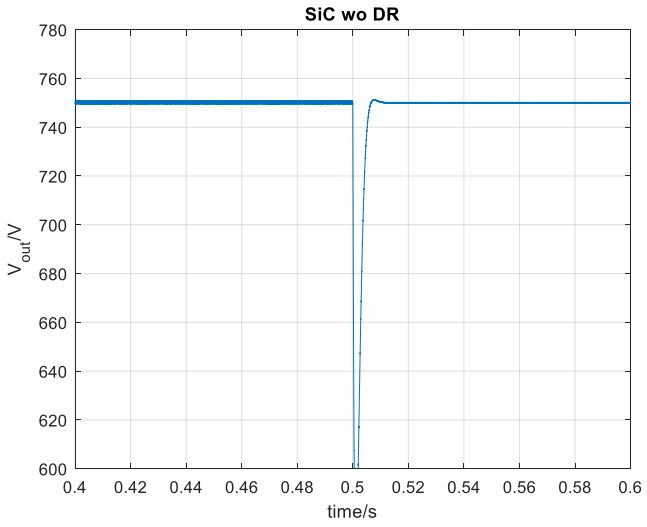


Fig. 6.15 Output Voltage Deviation of 'SiC w/o DR' Design

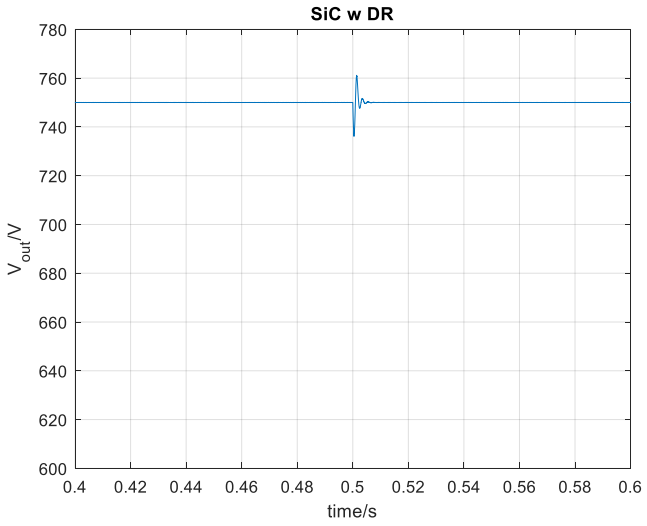


Fig. 6.16 Output Voltage Deviation of 'SiC w DR' Design

# 7. HARDWARE VALIDATION

In this chapter, a 10 kW SiC based dc generation system is designed based on a preliminary version of the design code. Measurements of the system steady-state operation are compared to those produced by the analytical design model. To this end, Section 7.1 describes the system as built. Section 7.2 compares system steady-state operating waveforms with the results obtained from the design model.

## 7.1 10 kW DC Generation System as Built

The system as built contains a surface mount PMSM, two PMIs, a SiC based passive rectifier, and a SiC based dc-dc converter. The design and fabrication of those components are described in this section.

### 7.1.1 PMSM as Built

The PMSM prototype is designed with the analytical model proposed in Section 4.1 except the number of slots per pole per phase is set as 2 instead of 1. The PMSM specifications are listed in Table 7.1.

Table 7.1 Prototype PMSM Specifications

| Description | Symbol | Value |
|---|---|---|
| Number of poles | $P$ | 14 |
| Rotor inert region radius | $r_i$ | 6.41 cm |
| Rotor backiron radius | $r_{rb}$ | 7.05 cm |
| Rotor permanent magnet radius | $r_g$ | 7.39 cm |
| Stator teeth radius | $r_{st}$ | 7.62 cm |
| Stator backiron radius | $r_{sb}$ | 9.05 cm |
| Stator shell radius | $r_{ss}$ | 9.69 cm |
| Tooth fraction | $\alpha_{st}$ | 0.5397 |
| Permanent magnet fraction | $\alpha_{pm}$ | 0.7350 |
| Active length | $l$ | 3.65 cm |
| Stator slots | $S_s$ | 84 |
| Mechanical rotor speed | $\omega_{rm}$ | 9000 RPM |
| Stator material | $m_s$ | JFE 10JNEX900 |
| Rotor material | $m_r$ | JFE 10JNEX900 |
| Conductor material | $m_c$ | Copper |
| Permanent magnet type | $t_{pm}$ | Sm2Co17-R30S |
| Fundamental conductor density | $N_{s1}$ | 119.9077 cond/rad |
| A phase winding pattern (1 pole) | $N_{as}$ | [0,4,11,11,4,0] |

The prototype is constructed with JFE 10JNEX900 high silicon steel to reduce core loss. The laminations are shown in Fig. 7.1.

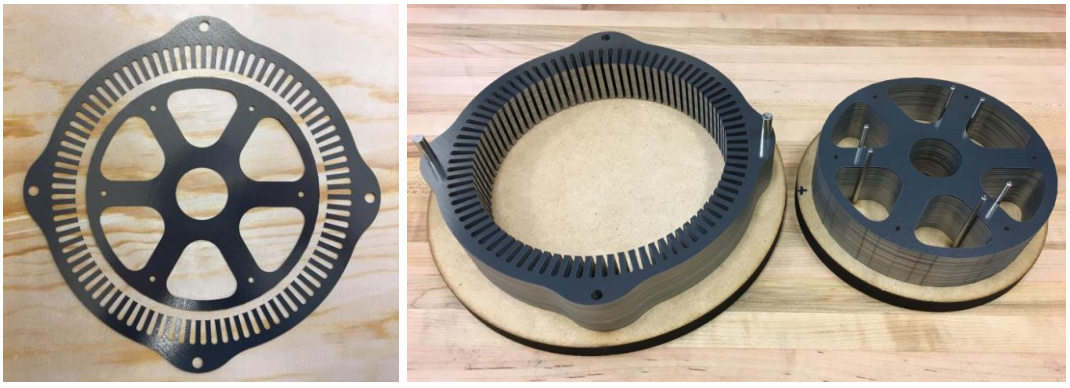

Fig. 7.1 PMSM Lamination and Lamination Stack

The PMSM stator fabrication procedures are similar to the procedures described in [35]. The stator as built is shown in Fig. 7.2. Two thermal couples are embedded in two different stator slots to measure the slot winding temperature. The slots that have the thermal couple embedded are labeled in Fig. 7.2(a) with ‘Slot 1’ and ‘Slot 2’. Another two thermal couples are embedded in the end winding to measure the end winding temperature. The locations where the thermal couple is placed in the end winding are labeled as ‘End 1’ and ‘End 2’ in Fig. 7.2(a).

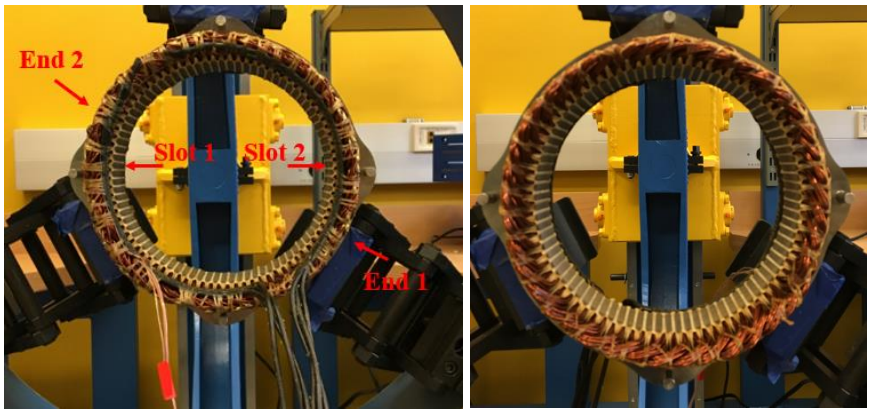


(a) (b)

Fig. 7.2 Stator Assembly: (a) Front Side (b) Back Side

The PMSM rotor fabrication procedures are different from the procedures described in [35] due to the different rotor configuration. The most significant difference is how the arc magnet is substituted with rectangular magnets to reduce manufacturing cost. The geometry modification due to the magnet rectangularization is shown in Fig. 7.3. The red contour is the original arc magnet from the design code. The arc magnet is approximated by two identical rectangular magnets PM1 and PM2. The rectangular magnet has a width of $w_m$. The height and length of the rectangular magnet are the same as the arc magnet which are $d_m$ and $l$, respectively. The width $w_m$ is calculated as

$$w_m = 2r_{rb}\tan\theta \tag{7.1}$$

where $\theta$ equals to $\pi\alpha_{pm}/(2P)$.

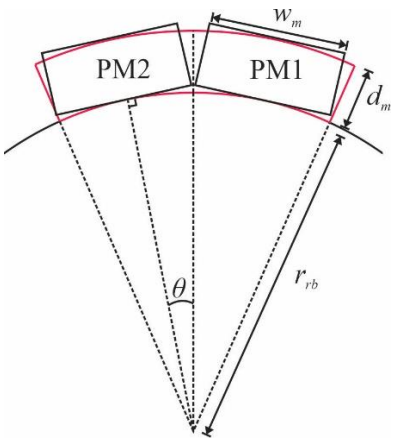


Fig. 7.3 Rotor Geometry Modification

In [35], the rotor lamination stack is potted to form a rigid rotor. In this work, two aluminum plates are clamped on both sides of the rotor lamination stack to hold them together. The assembled rotor is shown in Fig. 7.4.

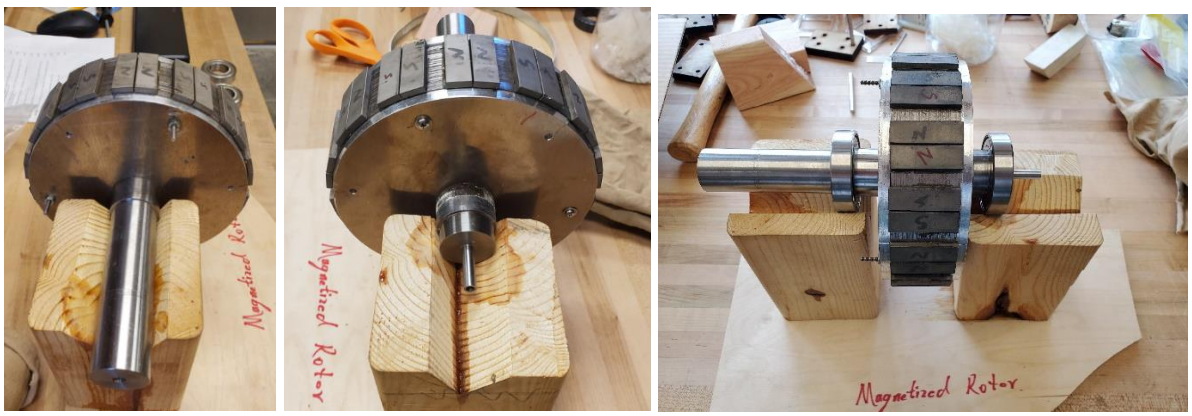


(a) (b) (c)

Fig. 7.4 Rotor Assembly (a) Without Bearing (Front) (b) Without Bearing (Back) (c) With Bearing

The stator and rotor are assembled with two end bells [35] to form a complete PMSM. The assembled PMSM is shown in Fig. 7.5.

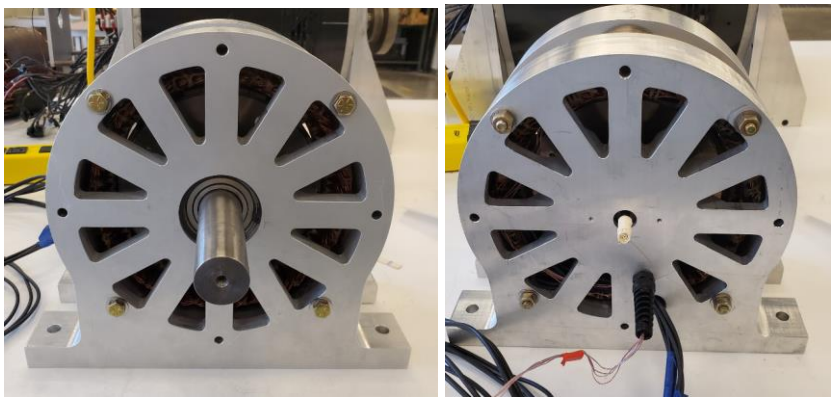

(a) (b)

Fig. 7.5 PMSM Assembly: (a) Front Side (b) Back Side

The lumped parameters of the PMSM as built are compared to the values predicted by the analytical model and the FEA. The prototype phase resistance is measured using 4-wire test at room temperature (23 $°C$ ). The a-, b-, and c- phase resistance are measured as 0.684 Ω, 0.685 Ω, and 0.685 Ω, respectively. The phase resistance predicted by the analytical model is 0.632 Ω at room temperature. The difference between the measured resistance and the predicted resistance can be partially explained by the lead wires that are not included in the analytical model. The soldering points between the winding coils also increase the phase resistance. During the winding construction, working the wire also increases conductor resistance. The uncertainty in end winding construction also contributes to the phase resistance difference.

The *d*-axis inductance $L_d$ from the analytical model is 1.6 mH. The $L_d$ is measured as 1.48 mH using the circuit shown in Fig. 7.6 and an LCR meter at 60 Hz with 2 A dc bias current. This is a 7.5% difference. For the circuit shown in Fig. 7.6, when a positive $v_{cb}$ is applied, the

rotor *q*-axis is aligned with stator *as*-axis where $\theta_r = 0$. The *q*-axis current is 0 and *d*-axis current is $2/\sqrt{3}i_{cs}$. The $L_d$ is half of the inductance measured across the terminals.

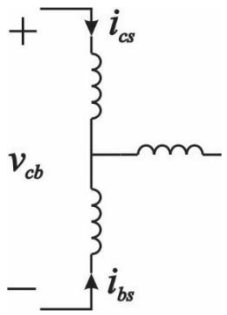


Fig. 7.6 *d*-axis Inductance Measurement Circuit

The *q*-axis inductance $L_q$ from the analytical model is 1.58 mH. The $L_q$ is measured as 1.44 mH using the circuit shown in Fig. 7.7 and the same LCR meter setup as measuring $L_d$. This is an 8.8% difference. To measure the $L_q$, the same rotor position as measuring *d*-axis inductance is held so $\theta_r = 0$. When a positive $v_{ab}$ is applied to the circuit shown in Fig 7.7, the resulted *d*-axis current is 0 and *q*-axis current is $i_{as}$ assuming the current is evenly distributed in *b*-phase and *c*-phase. The $L_q$ is 2/3 of the inductance measured across the terminals.

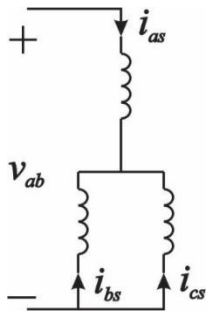


Fig. 7.7 *q*-axis Inductance Measurement Circuit

The flux linkage due to the permanent magnet $\lambda_m$ calculated from the analytical model is 102.5 mVs. A FEM is established herein to calculate the *a*-phase back EMF $v_{as,oc}$ at a rotor electrical speed of 175 rad/s. The peak value of the $v_{as,oc}$ fundamental component is divided by the electrical speed to yield $\lambda_m$ which is 100.0 mVs. The error between the FEM and analytical model is 2.5%. This error can be explained by the magnet rectangularization which is not considered in the analytical model. The PMSM as built is driven by a dynamometer at a rotor electrical speed of 175 rad/s to find the three phase back EMF. The result is shown in Fig. 7.8. The Fast Fourier Transform is applied to *a*-phase back EMF to extract the fundamental component. The peak value of the fundamental component is divided by the electrical speed to yield the $\lambda_m$ of the prototype which is 95.2 mVs. The error between the analytical result and the measured result is 7.7%. This error can be attributed to the inconsistency between the $B_r$ of the prototype permanent magnet and the $B_r$ used in the analytical model.

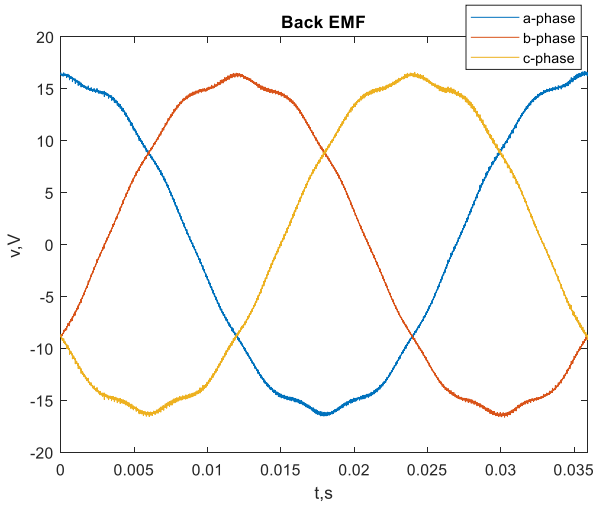


Fig. 7.8 Measured Prototype Back EMF

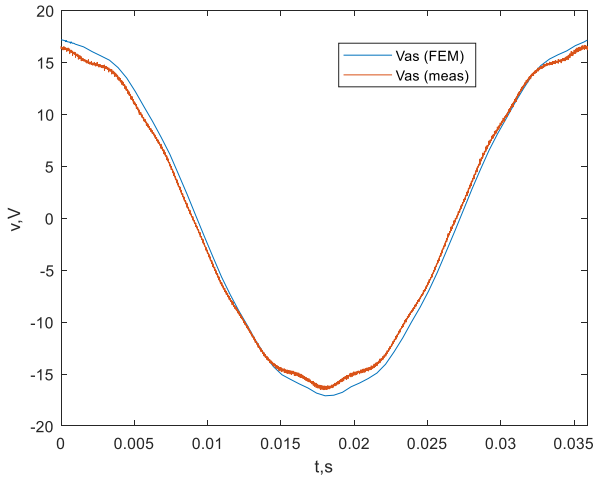


Fig. 7.9 Comparison between $v_{as,oc}$ from FEM and Measured $v_{as,oc}$

### 7.1.2 PMI as Built

The system design paradigm used a metamodel to determine the PMI mass and loss based on rated inductance, rated operating current, and current density. From the selected system design, the incremental inductance objective $L_{inc}$ for the input PMI is 2.74 mH and the rated operating current $i_{pk}$ is 10.08 A. For the output PMI, the $L_{inc}$ is 0.699 mH and the $i_{pk}$ is 13.33 A.

With $L_{inc}$ and $i_{pk}$ determined from the system design paradigm, the dedicated design approach used in Section 3.1.7 is applied to achieve detailed PMI designs. The least mass design is selected in this work. The dedicated design parameters for the least mass input PMI and output PMI are listed in Table 7.2 and Table 7.3, respectively. The parameters' definition can be found in Section 3.1.

Table 7.2 Input PMI as Built Design Parameters

| Parameter | Value | Parameter | Value |
|---|---|---|---|
| $g_c$ (mm) | 0.3 | $r_{wei}$ | 0.613 |
| $g_e$ (mm) | 2.3 | $r_{wci}$ | 0.601 |
| $d_s$ (mm) | 49.8 | $r_{wbi}$ | 0.585 |
| $w_s$ (mm) | 12.9 | $r_{wexe}$ | 0.832 |
| $r_{dws}$ | 0.894 | $N$ | 118 |
| $r_{wws}$ | 0.484 | $a_{cd}$ (mm$^2$) | 1.65 |
| $w_i$ (mm) | 6.3 | $l_{pm}$ (mm) | 2.3 |
| $d$ (mm) | 11 | $t_{pm}$ | 6 |

Table 7.3 Output PMI as Built Design Parameters

| Parameter | Value | Parameter | Value |
|---|---|---|---|
| $g_c$ (mm) | 0.33 | $r_{wei}$ | 1.05 |
| $g_e$ (mm) | 2.7 | $r_{wci}$ | 1.16 |
| $d_s$ (mm) | 29.9 | $r_{wbi}$ | 1.14 |
| $w_s$ (mm) | 12.4 | $r_{wexe}$ | 0.757 |
| $r_{dws}$ | 0.892 | $N$ | 52 |
| $r_{wws}$ | 0.473 | $a_{cd}$ (mm$^2$) | 2.08 |
| $w_i$ (mm) | 4 | $l_{pm}$ (mm) | 1.4 |
| $d$ (mm) | 26.8 | $t_{pm}$ | 5 |

The two PMI prototypes are shown in Fig. 7.10. The input PMI is built with Hiperco 50 electrical steel. The laminations are cut in house using the same laser cutter as in Section 7.1.1. An insulation coating is added afterwards to reduce eddy current loss. The output PMI is built with Ferrite MN80. There are two coils for each PMI that are wound around a 3D printed bobbin and

put into the E core slot. The number of turns of each coil is $N/2$. In this way, one coil is connected to the upper rail of the dc bus and another coil can be connected to the lower rail of the dc bus to suppress circuit common mode behavior while the total inductance of the PMI is kept the same. The circuit diagram is given in Fig. 7.15. The polypropylene plastic plates are applied to hold the laminations together and protect the fragile ferrite core.

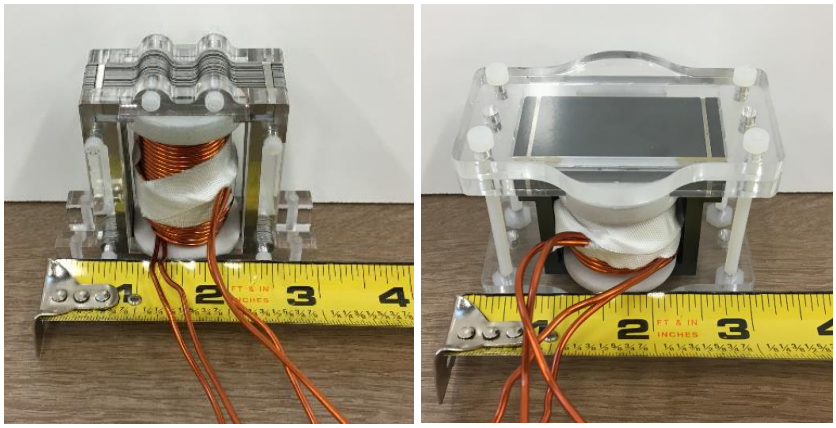

(a) (b)

Fig. 7.10 PMI Prototypes: (a) Input PMI (b) Output PMI

The PMI resistance, impedance characteristics, and hysteresis curves are measured. The resistance is measured using 4-wire test at room temperature (23 $°C$). The input PMI resistance and output PMI resistance are 88 mΩ and 51 mΩ, respectively. The predicted input PMI and output PMI resistance from detailed design model are 83 mΩ and 43 mΩ, respectively. The error is 6% and 16% for input PMI and output PMI, respectively. The error could be explained by the lead wire that is not considered in the detailed design model. The wire winding procedure can also increase resistance.

The impedance characteristic is measured using an LCR meter. The magnitude and angle of the impedance are measured. The input PMI impedance is shown in Fig. 7.11. The input PMI

appears inductive until 300 kHz. Since the input PMI mainly sees the switching frequency from passive rectifier which is 6.3 kHz when the PMSM operates at 9000 rpm, this should be adequate. The output PMI impedance is shown in Fig. 7.12 which is inductive until 700 kHz. The output PMI mainly sees the switching frequency from the dc-dc converter switch which is less than 100 kHz.

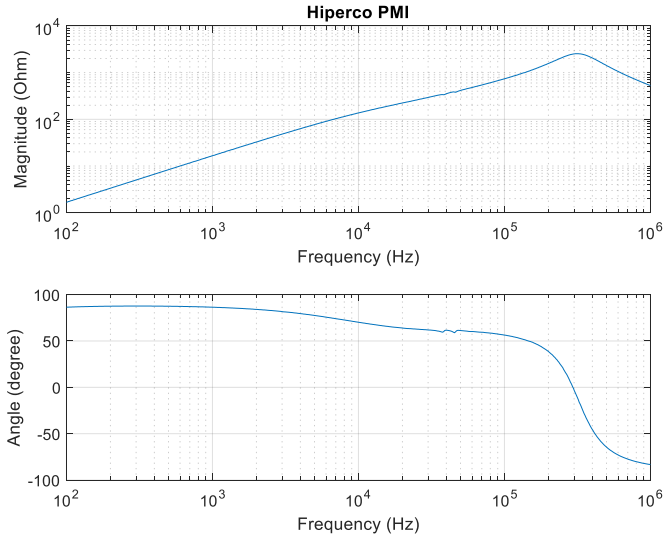


Fig. 7.11 Input PMI Impedance Magnitude and Angle

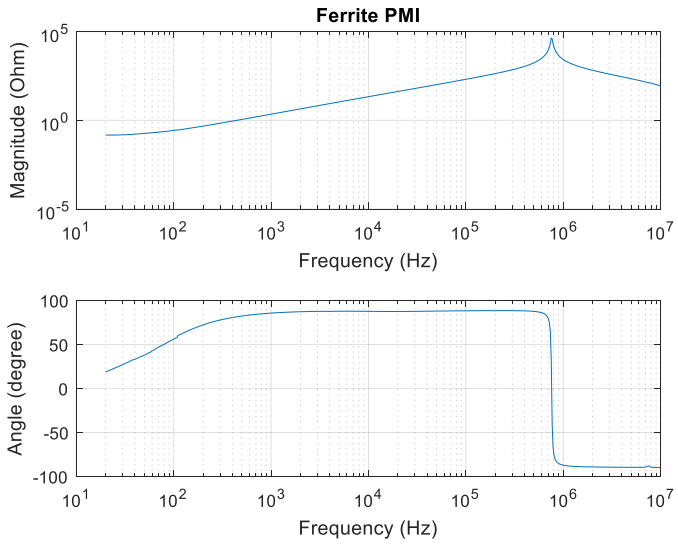


Fig. 7.12 Output PMI Impedance Magnitude and Angle

The hysteresis curve is measured to ensure the PMIs are not saturated at the rated current. A single phase transformer is used to supply a 60 Hz sinusoidal signal to the PMI. The PMI voltage and current are measured using an oscilloscope. The flux linkage is obtained by integrating the voltage less the dc resistive voltage drop. According to [7], the offset in the flux linkage waveform due to the constant PM flux is unknown. In this work, the average value of the flux linkage is used as the offset of the flux linkage waveform in Fig. 7.13 and Fig. 7.14. The input PMI hysteresis curve is shown in Fig. 7.13. It can be observed that the PMI is saturated at -5 A and 10 A. The asymmetry of the hysteresis curve is caused by the dc flux introduced by the permanent magnet. The incremental inductance measured at rated current (10A) is 2.66 mH by measuring the hysteresis curve slope at 10A. The predicted inductance from detailed design model is 2.74 mH. The error is 3%. The output PMI hysteresis curve is shown in Fig. 7.11. The output PMI is saturated at -3 A and 15 A. The incremental inductance measured at rated current (13.3A) is 0.52 mH. The predicted inductance from detailed design model is 0.699 mH which gives an error of 26%. One possible reason that causes the large error of the output PMI inductance is that the fabrication of

the ferrite core could cause a larger air gap compared to the detailed design model. The large air gap increases the inductor reluctance which reduces the inductance.

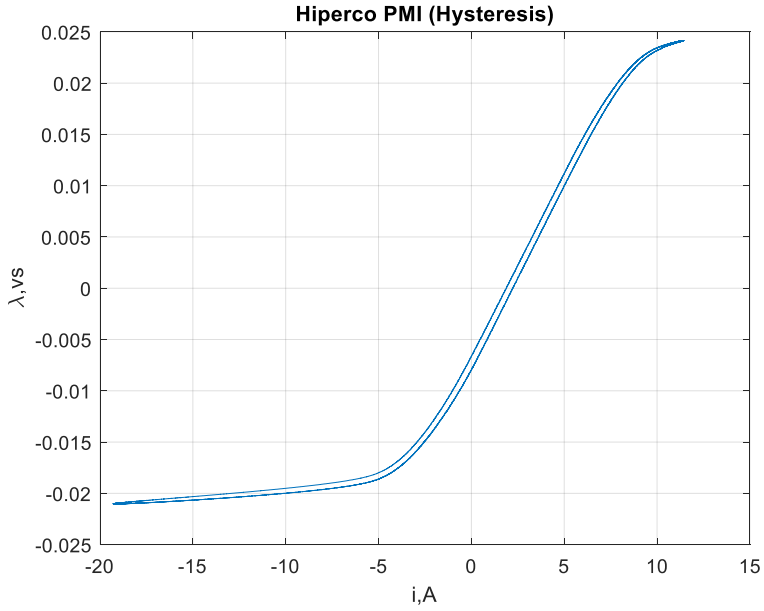


Fig. 7.13 Input PMI Hysteresis Curve

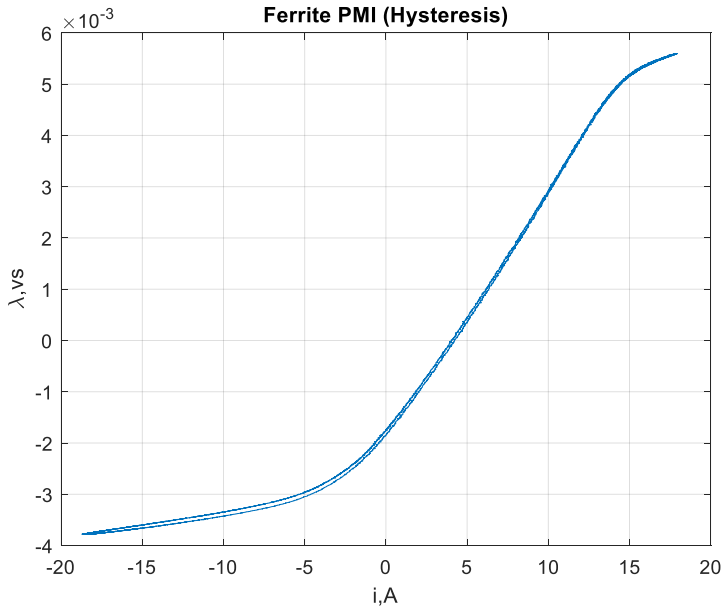


Fig. 7.14 Output PMI Hysteresis Curve

### 7.1.3 Passive Rectifier and DC-DC Converter as Built

The dc generation system contains a passive rectifier and a dc-dc converter. The passive rectifier is built with six Cree C4D20120A diodes [28]. The dc-dc converter as built is shown in Fig. 7.12. The switches $T_1$ and $T_2$ are Cree C2M0080120D MOSFETs [27]. The diodes $D_1$, $D_2$ and $D_s$ are Cree C4D20120A diodes. The rest of the circuit components specification are listed in Table 7.4. The $L_{in}$ and $L_{out}$ value are the PMI incremental inductances at rated current which are documented in Section 7.1.2. The $D_s$, $C_s$, and $r_s$ function as a snubber circuit which is used to protect the MOSFTs from high-frequency switching transients. The $C_s$ and $r_s$ are determined based on the method introduced in [23]. The gate driver of the MOSFET is CREE CRD-001 [46].

The finished passive rectifier and dc-dc converter as built are shown in Fig 7.13.

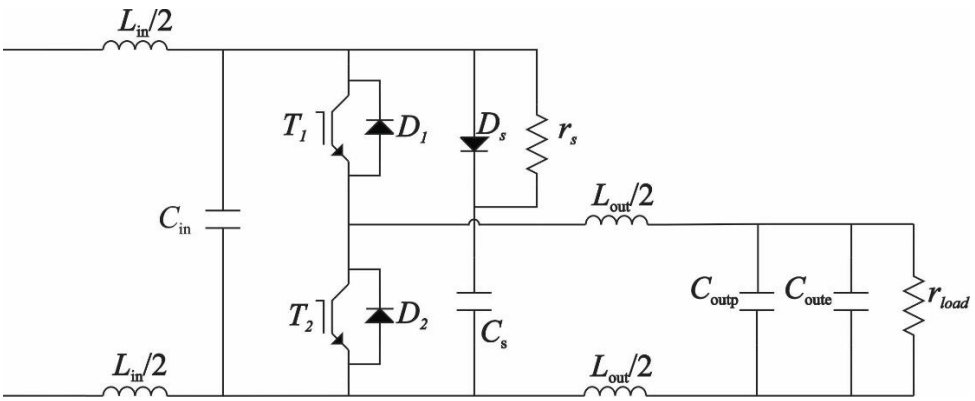


Fig. 7.15 DC-DC Converter

Table 7.4 DC-DC Converter Specifications

| Component | Value | Component | Value |
|---|---|---|---|
| $L_{in}$ | 2.66 mH | $L_{out}$ | 0.52 mH |
| $C_{in}$ | 15 μF | $C_{outp}$ | 5 μF |
| $C_s$ | 47 nF | $C_{oute}$ | 75 μF |
| $r_s$ | 10 Ω | | |

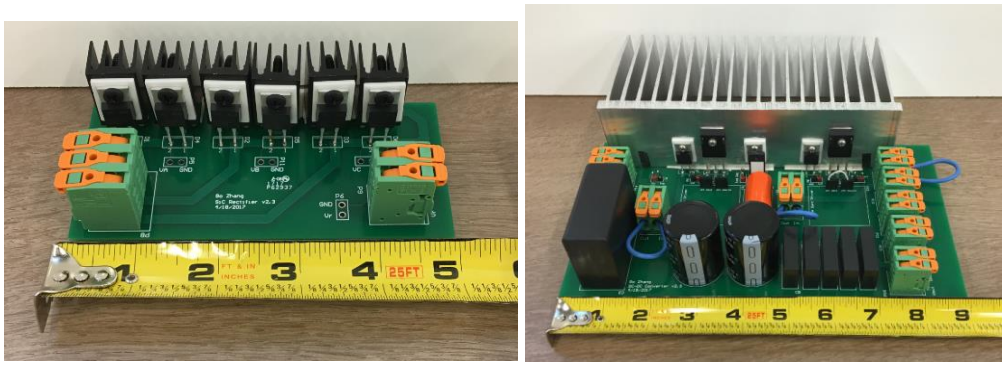

(a) (b)

Fig. 7.16 (a) SiC Passive Rectifier (b) SiC DC-DC Converter

## 7.2 System Steady State Test

After each system component is built and characterized, the dc generation system is put together to test its steady state performance.

### 7.2.1 System Test Setup

Due to the limitation of the lab equipment, the system is not tested at its rated operating point (9000 RPM, 10 kW). The system test specifications are listed in Table 7.5. It should be noted that the test is an open loop test. The duty cycle of the dc-dc converter is set by a signal generator.

Table 7.5 System Test Specifications

| Description | Symbol | Value |
|---|---|---|
| PMSM Speed | $\omega_{rm}$ | 3600 RPM |
| Load Resistance | $r_{load}$ | 26.67 Ω |
| MOSFET $T_1$ duty cycle | $d$ | 0.8 |
| Switching frequency | $f_{sw}$ | 25 kHz |

The system test setup is shown in Fig. 7.17. The rectifier and the dc-dc converter setup are shown in Fig. 7.18. The Dynesystems 20 hp dynamometer system is used as the prime mover of the dc generation system. A resistor is used as the system load. The Agilent 33120A signal generator is applied to feed a 25 kHz 0.8 duty cycle square wave to the MOSFET gate driver as the switching signal of the dc-dc converter. The Yokogawa DL850 oscilloscope is used to measure rectifier dc current $i_r$, rectifier dc voltage $v_r$, output inductor current $i_L$, output voltage $v_{out}$, PMSM *a*-phase to ground voltage $v_{ag}$, *b*-phase to ground voltage $v_{bg}$, *c*-phase to ground voltage $v_{cg}$, *a*-phase current $i_{as}$, *b*-phase current $i_{bs}$, PMSM torque $T_e$, and PMSM speed $\omega_{rm}$.

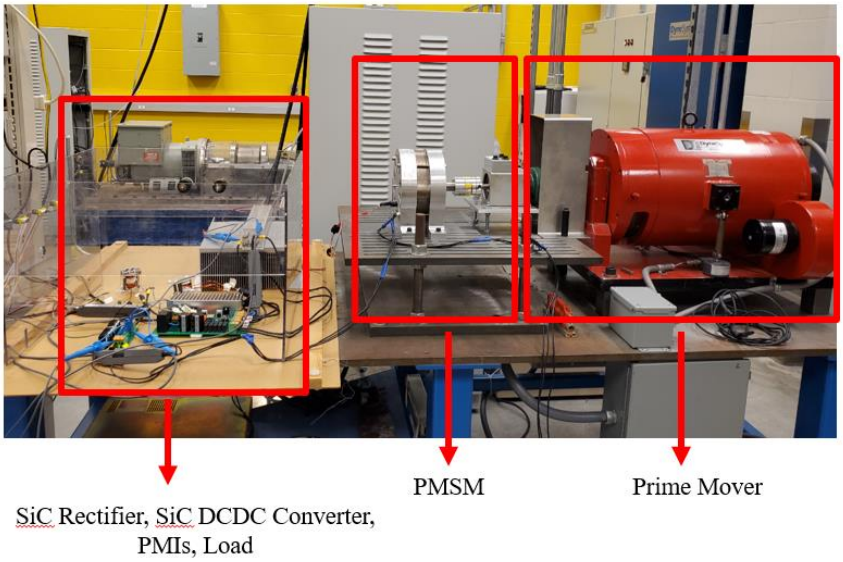


Fig. 7.17 System Steady State Test Setup

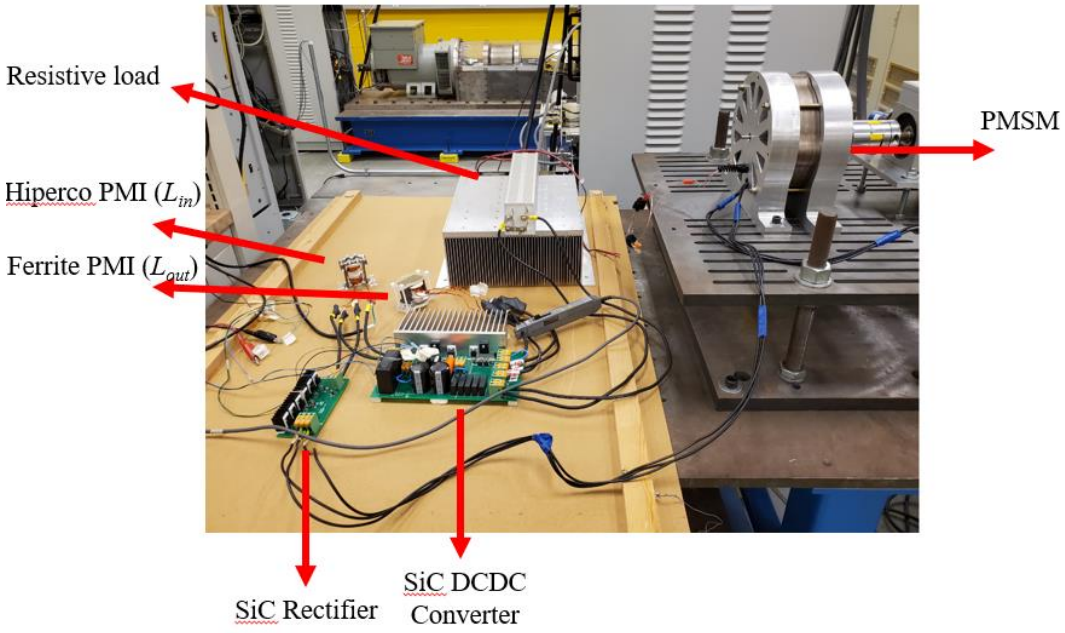


Fig. 7.18 Rectifier and DC-DC Converter Setup

### 7.2.2 Comparison Between Design Model Prediction, Waveform Level Model Prediction, and Measurement

To validate the system design model's accuracy, a system waveform level model (WLM) is developed. The $i_r$, $v_r$, $i_{as}$, $v_{ab}$, $i_L$ and $v_{out}$ predicted by the design model are compared to the WLM results and measurements. The system components characterized values are used in the design model prediction and WLM prediction instead of the design values obtained from the optimization algorithm. In this way, the error between the prediction results and measurements caused by the components fabrication can be eliminated. The comparison between the components design values and characterized values are listed in Table 7.6. The PMSM characterized values and PMI characterized values are from Section 7.1. The rated capacitance of the capacitors on the dc-dc converter board is used as the characterized capacitance in Table 7.6.

Table 7.6 Components Design Value vs. Characterized Value

| Parameters | Design Value | Characterized Value |
|---|---|---|
| PMSM Resistance | 0.632 Ω | 0.684 Ω |
| PMSM *q*-axis Inductance | 1.6 mH | 1.44 mH |
| PMSM *d*-axis Inductance | 1.58 mH | 1.48 mH |
| PMSM Flux linkage | 102.5 mVs | 95.2 mVs |
| Output Inductor | 0.7 mH | 0.52 mH |
| Input Inductor | 2.74 mH | 2.66 mH |
| Input Capacitor | 12.14 μF | 15 μF |
| Output Polypropylene Capacitor | 3.82 μF | 5 μF |
| Output Electrolytic Capacitor | 77.13 μF | 75 μF |

The inputs of the design model are given in Table 7.7 based on the measurements.

Table 7.7 Design Model Inputs

| Parameters | Symbol | Value |
|---|---|---|
| Rotor Mechanical Speed | $\omega_{rm}$ | 3598 RPM |
| System Output Power | $P_{out}$ | 3240.1 W |
| System Output Voltage | $v_{out}$ | 290.4 V |

The inputs of the WLM are given in Table 7.8 based on the design model prediction.

Table 7.8 Waveform Level Model Inputs

| Parameters | Symbol | Value |
|---|---|---|
| Rotor Mechanical Speed | $\omega_{rm}$ | 3598 RPM |
| MOSFET Effective Voltage Drop | $v_{fsw}$ | 1.99 V |
| Diode Effective Voltage Drop | $v_{fd}$ | 1.44 V |
| DC-DC Converter Duty Cycle | $d$ | 0.8 |
| Resistive Load | $r_{load}$ | 26.03 Ω |

The measured and predicted rectifier dc voltage $v_r$ are shown in Fig. 7.19. The difference between the WLM waveform and the measurement waveform is small. The design model predicts a larger voltage ripple than WLM. According to [24], the waveform reconstruction algorithm used in the design model can lead to a large dc voltage ripple if the derivative of dc current is large.

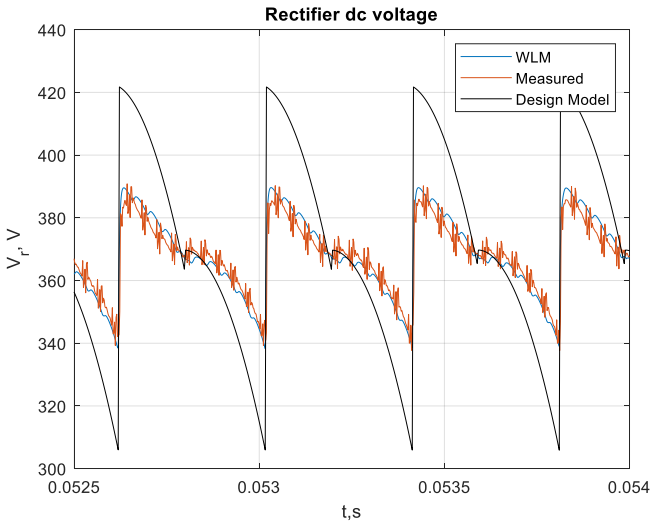


Fig. 7.19 Rectifier DC Voltage Comparison

The measured and predicted rectifier dc current $i_r$ are shown in Fig. 7.20. The difference between the WLM waveform and the measurement waveform is small. The large current ripple in the design model prediction is due to the large dc voltage ripple shown in Fig. 7.19. The voltage ripple from the input capacitor also contributes to the difference between the measured waveform and predicted waveform.

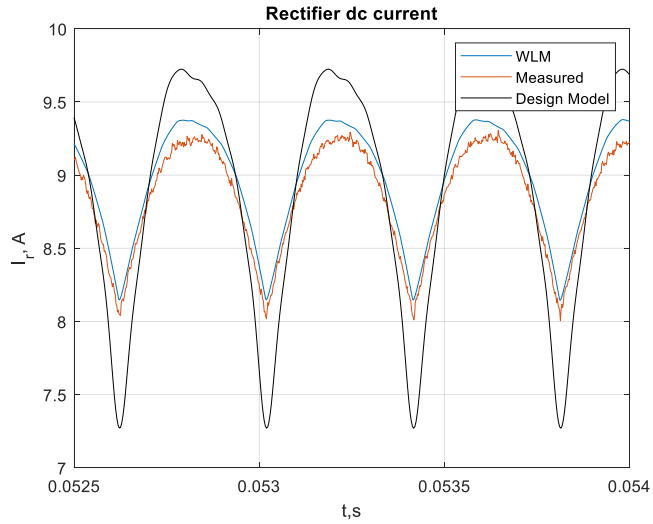


Fig. 7.20 Rectifier DC Current Comparison

Since the PMSM is Y-connected, the *c*-phase current is calculated as

$$i_{cs} = -i_{as} - i_{cs} \tag{7.2}$$

The PMSM phase currents measured are shown in Fig. 7.21.

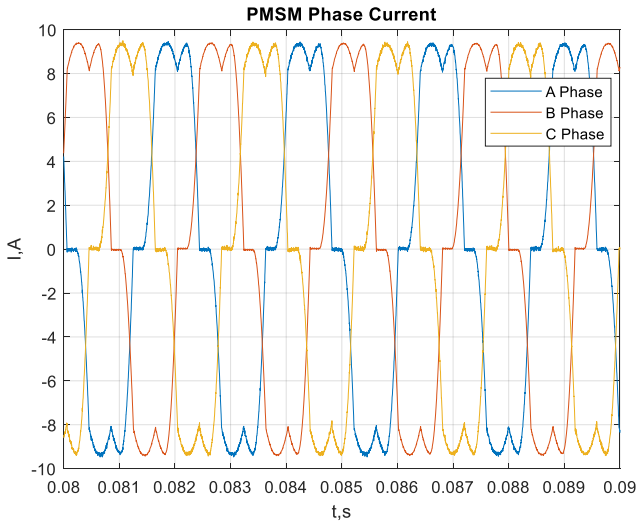


Fig. 7.21 PMSM Phase Currents

The measured and predicted *a*-phase current $i_{as}$ are shown in Fig. 7.22. The three waveforms have the same shape overall although the WLM waveform has the highest peak value compared to other two waveforms. This difference is caused by the rectifier representation in WLM which has a large rectifier loss compared to the design model and measurement. The inconsistency between the design model and measurement is due to the dc current waveform deviation shown in Fig. 7.20.

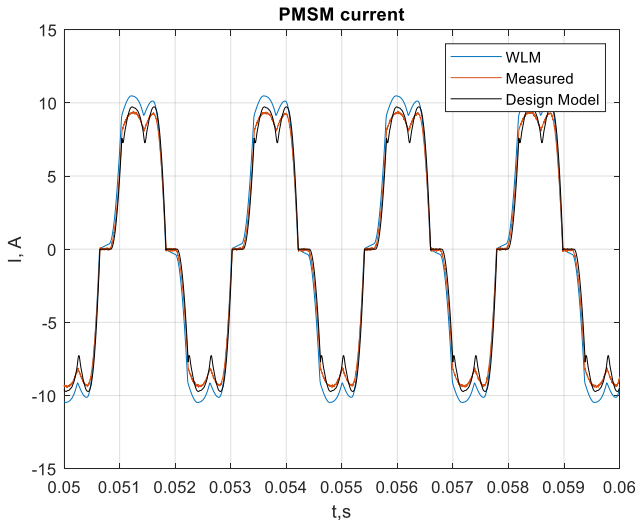


Fig. 7.22 PMSM *a*-phase Current Comparison

The PMSM measured line-line voltage $v_{ab}$, $v_{bc}$, and $v_{ca}$ are calculated from the measured line to ground voltages $v_{ag}$, $v_{bg}$, and $v_{cg}$. The line-line voltages are shown in Fig. 7.23.

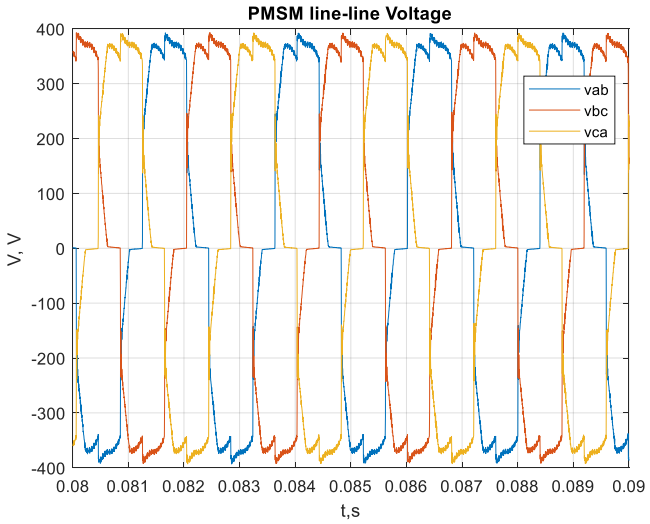


Fig. 7.23 PMSM Line-Line Voltage

The measured and predicted line-line voltage $v_{ab}$ are shown in Fig. 7.24. The difference between the WLM waveform and the measurement waveform is small. The inconsistency between the design model and measurement is due to the dc voltage deviation shown in Fig. 7.19.

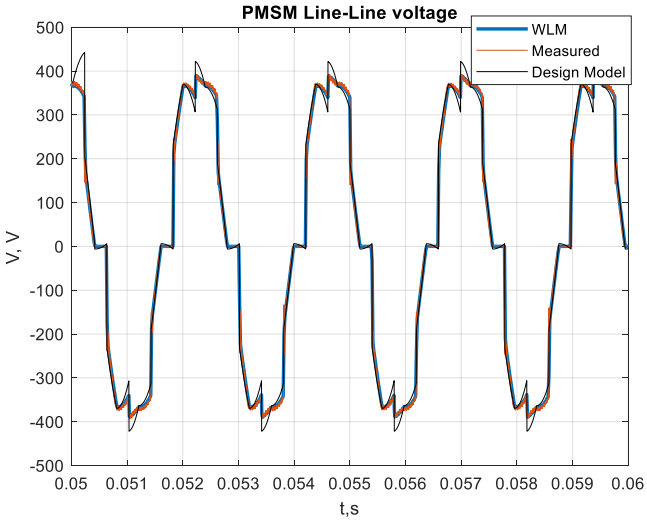


Fig. 7.24 PMSM Line-Line Voltage Comparison

The measured and predicted output inductor current $i_L$ is shown in Fig. 7.25 on two different time scales. The ripple due to the dc-dc converter switching is 43.5% of the average value from measurement. From the WLM, the ripple is 42.2% of the average value. The ripple predicted from the design model is 40.24%. The difference between the measurement, the WLM, and the design model is small.

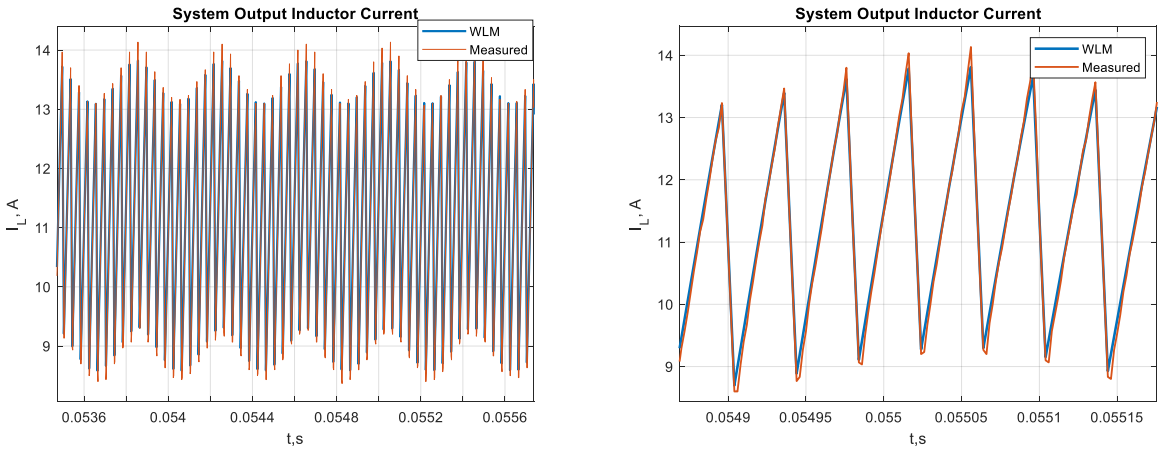


(a) (b)

Fig. 7.25 (a) Output Inductor Current Ripple Due to Rectifier (b) Ripple Due to Converter Switching

The measured and predicted output voltage $v_{out}$ is shown in Fig. 7.26 on two different time scales. The ripple due to the dc-dc converter switching is 0.7% of the average value from the measurement. From the WLM, the ripple is 0.1% of the average value. The ripple predicted from the design model is 0.8% of the average value. The difference between the design model and measurement is small. The smaller ripple obtained from the WLM is due to the rated capacitance applied for the electrolytic capacitor which neglects the frequency derating performance. Based on (3.63), the effective capacitance of the output electrolytic capacitor can be predicted. The effective capacitance of the 75 μF electrolytic capacitor at the converter switching frequency (25 kHz) is 8.77 μF. In Fig. 7.27, the output voltage waveform is obtained by using the effective capacitance at switching frequency in WLM. It is observed that the ripple due to the converter switching is close to the measurement. However, the ripple due to the rectifier is enlarged since the ripple due to the rectifier operation has a frequency of 2.5 kHz which is one tenth of the switching frequency. The effective capacitance at 2.5 kHz is larger than the effective capacitance

used in WLM according to (3.63). Thus in this case the WLM predicts a larger ripple due to the rectifier than is observed in the measurement.

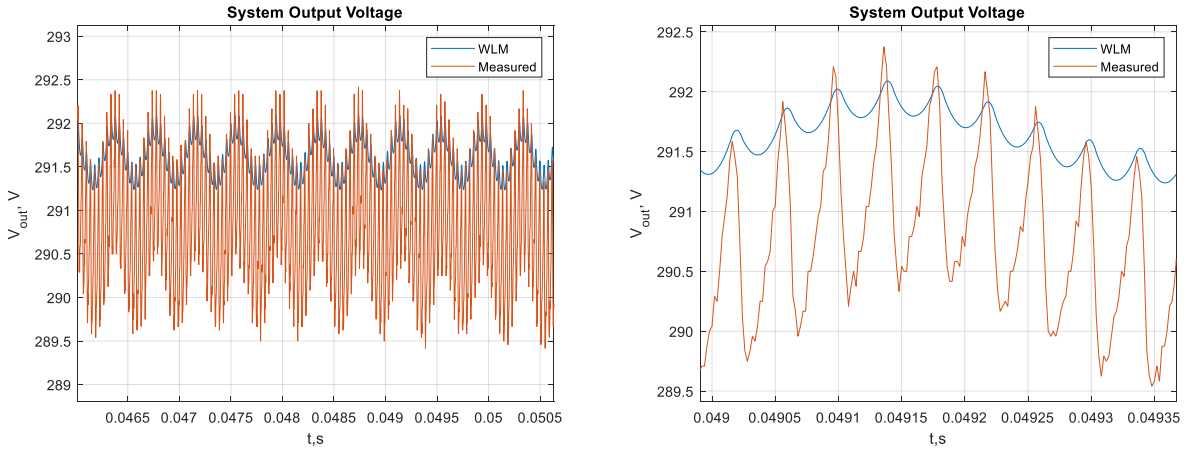


(a) (b)

Fig. 7.26 (a) Output Voltage Ripple Due to Rectifier (b) Ripple Due to Converter Switching

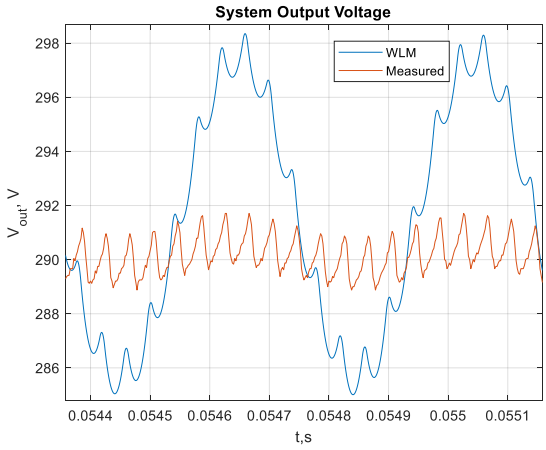


Fig. 7.27 Output Voltage Ripple Considering Electrolytic Capacitor Frequency Derating Property

One approach to finding power is to first find the *qd*-axis voltage and current. The stationary reference frame is applied herein. Based on [41], the *qd*-axis voltage is calculated as

$$\begin{bmatrix} v_{qs} \\ v_{ds} \end{bmatrix} = \frac{2}{3} \begin{bmatrix} \cos(0) & \cos\left(\frac{2\pi}{3}\right) \\ \sin(0) & \sin\left(\frac{2\pi}{3}\right) \end{bmatrix} \begin{bmatrix} v_{ab} \\ v_{cb} \end{bmatrix} \tag{7.3}$$

The *qd*-axis current is calculated as

$$\begin{bmatrix} i_{qs} \\ i_{ds} \end{bmatrix} = \frac{2}{3} \begin{bmatrix} \cos(0) & \cos\left(-\frac{2\pi}{3}\right) & \cos\left(\frac{2\pi}{3}\right) \\ \sin(0) & \sin\left(-\frac{2\pi}{3}\right) & \sin\left(\frac{2\pi}{3}\right) \end{bmatrix} \begin{bmatrix} i_{as} \\ i_{bs} \\ i_{cs} \end{bmatrix} \tag{7.4}$$

Since the zero sequence current $i_{0s}$ is zero, the PMSM electrical power $P_{elec}$ is calculated as

$$P_{elec} = \frac{3}{2}(v_{qs} i_{qs} + v_{ds} i_{ds}) \tag{7.5}$$

The PMSM mechanical power $P_{mech}$ is calculated as

$$P_{mech} = T_e \omega_{rm} \tag{7.6}$$

The efficiency of the PMSM $\eta_{PMSM}$ is calculated as

$$\eta_{PMSM} = P_{elec} / P_{mech} \tag{7.7}$$

The predicted and measured PMSM performance and dc-dc converter performance are listed in Table 7.9 and Table 7.10, respectively. In Table 7.9, the torque has a 3.4% error between the design model and measurement, which could be partially due to magnet and windage loss. Another reason could be that the design model didn't consider the MMF drop in the stator backiron and rotor backiron. Also, the switching losses in the machine are neglected in the design model.

The torque from the WLM is 3.2% higher than the design model which is explained by the large rectifier loss in the WLM. The rectifier loss from the WLM is 386 W while the rectifier loss from the design model is only 22 W. The large rectifier loss from WLM is due to the bilinear resistor rectifier model which uses a large resistance to represent the diode when it is on and a small resistance when it is off. The PMSM efficiency predicted by the WLM is 7.6% higher than the design model result. One reason is that the WLM does not include core loss. Another reason of the efficiency difference is that the *qd*-axis flux linkage calculation in WLM is over simplified which did not perform a detailed field analysis.

In Table 7.10, $d$ denotes the MOSFET duty cycle, $P_r$ denotes the rectifier dc side power, and $\eta_{conv}$ denotes the efficiency of the dc-dc converter which is calculated by $\eta_{conv} = P_{out} / P_r$. The error between the dc-dc converter measurement performance and prediction performance is small.

Table 7.9 PMSM Performance Comparison

| | Measurement | Design Model Prediction | WLM Prediction |
|---|---|---|---|
| $\bar{T}_e$ | 9.49 Nm | 9.82 Nm | 10.13 Nm |
| $\omega_{rm}$ | 3598 RPM | 3598 RPM | 3598 RPM |
| $\bar{P}_{mech}$ | 3576 W | 3700 W | 3816 W |
| $\bar{P}_{elec}$ | 3309 W | 3296 W | 3689 W |
| $\eta_{PMSM}$ | 92.5 % | 89.1 % | 96.7 % |

Table 7.10 DC-DC Converter Performance Comparison

| | Measurement | Design Model Prediction | WLM Prediction |
|---|---|---|---|
| $d$ | 0.795 | 0.800 | 0.800 |
| $\overline{v}_{out}$ | 290.4 V | 290.4 V | 291.6 V |
| $\overline{i}_L$ | 11.16 A | 11.16 A | 11.20 A |
| $\overline{v}_r$ | 368.07 V | 366.66 V | 368.09 V |
| $\overline{i}_r$ | 8.87 A | 8.93 A | 8.97 A |
| $\overline{P}_{out}$ | 3240.1 W | 3240.1 W | 3267.0 W |
| $\overline{P}_r$ | 3265.1 W | 3274.46 W | 3303.52 W |
| $\eta_{conv}$ | 99.2% | 99.0 % | 98.9 % |

# 8. DC GENERATION SYSTEM DESIGN CONSIDERING PMSM THERMAL PERFORMANCE

In Chapter 5, the PMSM lumped parameters $r_s$, $L_q$, $L_d$, and $\lambda_m^{'}$ are used to determine the system steady state operation. The lumped parameters depend on the PMSM's operating temperature. The stator resistance $r_s$ increases as the winding temperature increases. The permanent magnet's residual flux density and coercivity are affected by the rotor temperature which affects the $\lambda_m^{'}$. In this chapter, the PMSM stator thermal equivalent circuit (TEC) model developed in [35] is applied to achieve a dc generation system design paradigm that considers the PMSM thermal performance.

In Section 8.1, the TEC model [35] is introduced and the heat transfer coefficients are calibrated based on the PMSM prototype introduced in Chapter 7. Section 8.2 derived the modified system design paradigm. The comparison between system design with TEC and without TEC is implemented in Section 8.3 to quantify the PMSM thermal performance's impact to the system.

## 8.1 TEC and TEC Calibration

Since the PMSM as built in Chapter 7 has the same stator and end bell structure as the PMSM considered in [35], the TEC derived therein is applied in this work. The TEC network is shown in Fig. 8.1. In Fig. 8.1, cuboid element A represents the stator tooth. Elements B, C, H, and I represent the stator backiron. Elements J, K, L, and M represent the end bell. Element D, E, F, G, O, and N represent the stator winding. The elements are connected with each other by thermal resistance. Based on this simplified TEC network, the PMSM steady state slot winding temperature ($T_{slt}$) and

end winding temperature ($T_{end}$) are calculated. The rotor is treated as an adiabatic and isothermal body. The rotor temperature ($T_r$) is assumed to be the same as the stator inner face temperature.

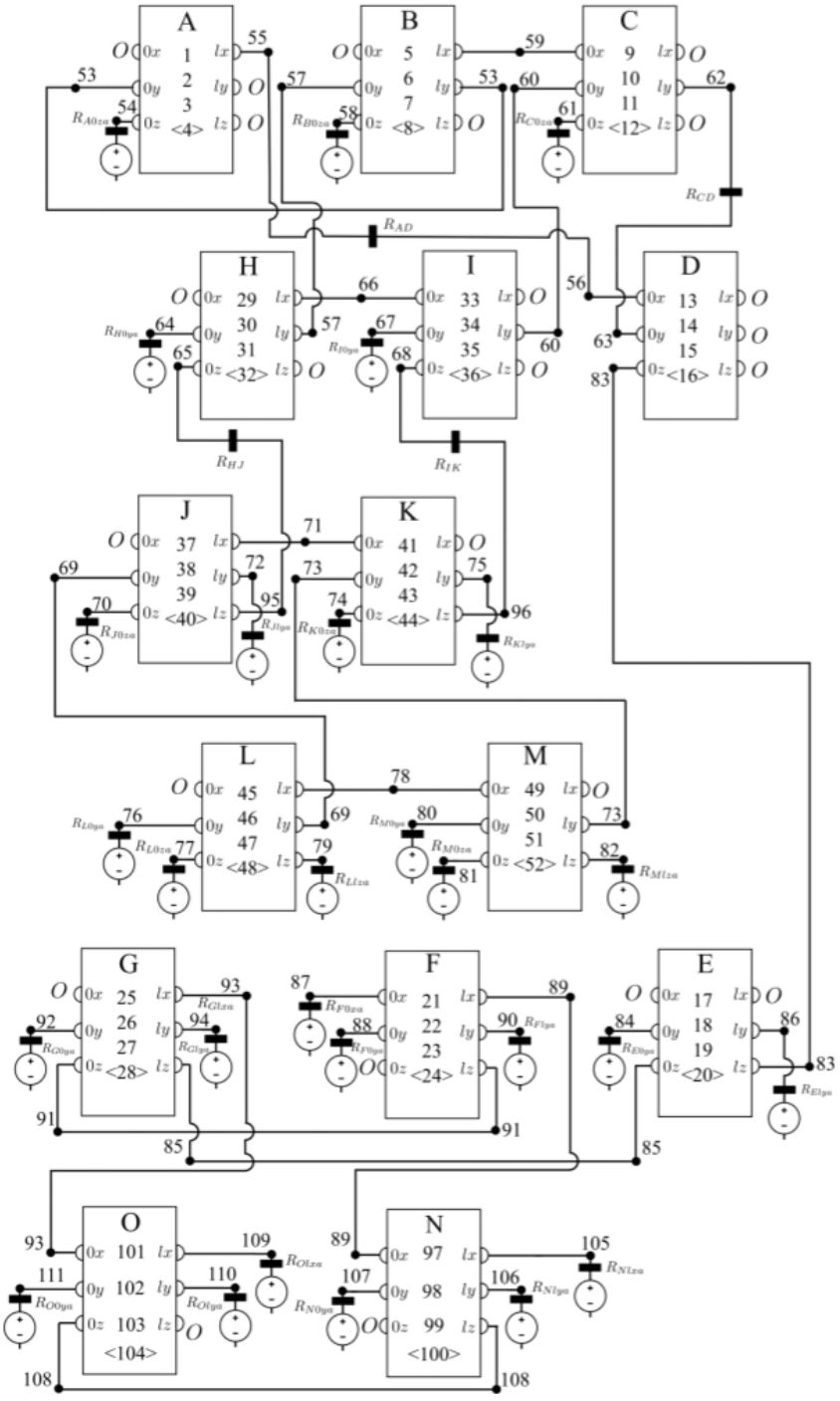


Fig. 8.1 TEC of the PMSM As Built [35]

In the TEC, there are five unknown parameters - the heat transfer coefficient between the stator steel and air ( $h_{sa}$ ), the end bell and air ( $h_{ea}$ ), the winding and air ( $h_{wa}$ ), the stator steel and the end bell ( $h_{se}$ ), and the effective winding to core gap distance ( $g_{wc}$ ). A thermal test is conducted to determine the unknowns. The PMSM phase windings are connected in series and fed by a dc power supply. The dc power supply voltage $v_{dc,meas}$ is 13.005 V and the dc power supply current $i_{dc,meas}$ is 5.21 A when the PMSM reaches to a thermal steady state. The total power consumed by the PMSM $P_{dc}$ is 67.76 W. The winding resistance at the thermal steady state is calculated by

$$r_{w,T} = \frac{v_{dc,meas}}{3i_{dc,meas}} \tag{8.1}$$

which yields 0.832 Ω. The winding resistance at room temperature (23 $^{\circ}C$ ) $r_{w,Tr}$ is 0.685 Ω. The mean temperature of the winding at thermal steady state is calculated as

$$T_{ave} = T_{room} + \frac{r_{w,T} - r_{w,Tr}}{r_{w,Tr}\alpha_c} \tag{8.2}$$

where $T_{room}$ is the room temperature, and $\alpha_c$ is the thermal coefficients of resistivity. The calculated $T_{ave}$ is 77.6 $^{\circ}C$ .

The slot winding and end winding temperatures are measured by the thermal couples embedded in two stator slots and two end winding locations which are shown in Fig. 7.2 (a). The end bell face temperature $T_{eb,m}$ and the stator outer backiron temperature $T_{sb,m}$ are measured using an infrared thermal camera. The measurements are shown in Table 8.1. The slot winding temperature $T_{sl,m}$ is determined by taking the average of the temperatures measured at Slot 1 and Slot 2 in Table 8.1 which yields 75.25 $^{\circ}C$ . The end winding temperature $T_{ew,m}$ is determined by

taking the average of the temperatures measured at End Winding 1 and End Winding 2 in Table 8.1 which yields $78.85\,^{\circ}C$ .

Table 8.1 Thermal Test Measurements

| Location | Temperature ($^{\circ}C$) |
|---|---|
| Slot 1 | 73.7 |
| Slot 2 | 76.8 |
| End Winding 1 | 77.9 |
| End Winding 2 | 79.8 |
| End Bell Face | 47.1 |
| Stator Outer Backiron | 74.3 |
| Ambient | 22.8 |

The calibration approach used in [35] is applied herein to determine the unknown heat transfer coefficients and $g_{wc}$ . The unknown variables are grouped as a vector which is given by

$$\boldsymbol{\theta}_{TEC} = [h_{sa} \quad h_{ea} \quad h_{wa} \quad h_{se} \quad g_{wc}] \tag{8.3}$$

The power loss of each winding element (D, E, F, G, O, and N in Fig. 8.1) is calculated as

$$P_x = \frac{P_{dc}}{4S_S}\frac{V_x}{V_{winding}} \tag{8.4}$$

where $x \in (\mathrm{D, E, F, G, O, N})$ , $V_x$ is the volume of element *x*, and $V_{winding}$ is the winding total volume. The power loss of the stator elements is zero since the winding is fed by dc source. The power loss calculated by (8.4) are inputs to the TEC model to predict the temperature distribution with a given set of $\boldsymbol{\theta}_{TEC}$ .

Next, a single objective optimization was performed to fit the unknown $\boldsymbol{\theta}_{TEC}$. The optimization variable space is given in Table 8.2. The error between the measured temperature and TEC model predicted temperature is given as

$$e_n = \frac{T_{n,m} - T_{n,c}}{T_{n,m}} \tag{8.5}$$

where $T_{n,m}$ is the measured temperature at location '*n*', '*n*' can be '*eb*', '*sb*', '*sl*', or '*ed*', and $T_{n,c}$ is the predicted temperature at location '*n*'. The expressions for $T_{n,c}$ can be found in [35]. There is one constraint in the optimization which is to insure the difference between the measured temperature and TEC predicted temperature is less than 1 $^{\circ}C$. The constraint is expressed as

$$c_1 = \text{lte}\left(\max\left|T_{n,m} - T_{n,c}\right|, 1\right) \tag{8.6}$$

The fitness function is expressed as

$$\mathbf{f}(\boldsymbol{\theta}_{TEC}) = \begin{cases} \varepsilon\left(c_1 - 1\right) & c_1 < 1 \\ \dfrac{4}{\sqrt{\sum_{n=eb,sb,sl,ed} e_n^2}} & c_1 = 1 \end{cases} \tag{8.7}$$

The additional geometry parameters required in the calibration approach are listed in Table 8.3. The fitted parameters are shown in Table 8.4. The fitting error $e_n$ is zero. The predicted stator resistance is 0.763 Ω at the thermal steady state and 0.632 Ω at room temperature. The percentage change of the predicted resistance is 20.73%. The percentage change of the measured resistance is 21.46%. The difference is small.

Table 8.2 Variable Space for TEC Parameter Fitting

| Gene | Parameter | Min. | Max. | Encoding | Units |
|---|---|---|---|---|---|
| 1 | $h_{sa}$ | $1.0\cdot10^{-4}$ | $1.0\cdot10^{1}$ | Log | W/(Km$^2$) |
| 2 | $h_{ea}$ | 1 | $1.0\cdot10^{3}$ | Log | W/(Km$^2$) |
| 3 | $h_{wa}$ | $1.0\cdot10^{-3}$ | $1.0\cdot10^{2}$ | Log | W/(Km$^2$) |
| 4 | $h_{se}$ | $1.0\cdot10^{2}$ | $1.0\cdot10^{5}$ | Log | W/(Km$^2$) |
| 5 | $g_{wc}$ | $1.0\cdot10^{-7}$ | $1.0\cdot10^{-3}$ | Log | m |

Table 8.3 Additional Parameters Required in TEC Calibration

| Description | Symbol | Value |
|---|---|---|
| End bell-stator contact fraction | $\alpha_{eb}$ | 0.5 |
| Depth of end bell | $d_{eb}$ | 44.45 mm |
| Width of end bell | $w_{eb}$ | 12.8 mm |
| Wire insulation thickness | $t_i$ | 0.027 mm |
| Slot liner thickness | $t_{sl}$ | 0.254 mm |

Table 8.4 TEC Calibration Results

| Parameter | Value |
|---|---|
| $h_{sa}$ | 0.1609 W/(Km$^2$) |
| $h_{ea}$ | 5.311 W/(Km$^2$) |
| $h_{wa}$ | 23.69 W/(Km$^2$) |
| $h_{se}$ | 193.88 W/(Km$^2$) |
| $g_{wc}$ | 0.935 mm |

## 8.2 System Design Paradigm Considering PMSM Thermal Performance

The PMSM lumped parameters $r_s$ , $L_q$, $L_d$ , and $\lambda_m^{'}$ are required to calculate the PMSM operating current and the dc bus voltage using the waveform reconstruction algorithm. It is necessary to include the temperature's impact to the lumped parameters to achieve an accurate steady state calculation.

The stator winding resistance $r_s$ is a function of $T_{slt}$ and $T_{end}$ since the conductor resistivity depends on the conductor temperature. The conductor resistivity $\rho_{c,w}$ is expressed as

$$\rho_{c,w} = \frac{1+\alpha_T (T_w - T_0)}{\sigma_0} \tag{8.8}$$

where '$w$' is either '$slt$' or '$end$', $\alpha_T$ is conductor temperature coefficient, $T_0$ is the nominal temperature, $T_w$ is the winding temperature at slot or end winding, and $\sigma_0$ is the nominal conductor conductivity.

The $\lambda_m^{'}$ is function of $T_r$ since the permanent magnet residual flux density $B_r$ and intrinsic coercivity $H_{ci}$ depends on $T_r$. The $B_r$ and $H_{ci}$ at $T_r$ are expressed as

$$B_{r,T_r} = B_{r,0}(1-\alpha_B (T_r - T_0)) \tag{8.9}$$

$$H_{ci,T_r} = H_{ci,0}(1-\alpha_H (T_r - T_0)) \tag{8.10}$$

where $\alpha_B$ and $\alpha_H$ are the flux density and intrinsic coercivity derating factors, $B_{r,T_r}$ and $H_{ci,T_r}$ are the nominal residual flux density and nominal intrinsic coercivity.

The system design paradigm is modified to include the PMSM temperature's impact to the system design. In [35], an iterative method is applied to find the PMSM steady state temperature

given the PMSM operating current. In this work, the PMSM operating current is calculated based on the PMSM lumped parameters which are temperature dependent. To avoid another iterative loop which will slow down the optimization algorithm convergence, the estimated slot winding temperature at each operating point $T_{slt,est,op}$, estimated end winding temperature at each operating point $T_{end,est}$, and estimated rotor temperature at each operating point $T_{r,est,op}$ are added to the design space to find the estimated PMSM lumped parameters. The PMSM operating current are determined based on the estimated PMSM lumped parameters. Then the PMSM steady state temperatures are calculated based on the iterative method introduced in [35]. The following constraints are added to ensure the calculated temperatures are lower than the estimated temperatures

$$c_{32,op} = \text{lte}(T_{slt,op}, T_{slt,est,op}) \tag{8.11}$$

$$c_{33,op} = \text{lte}(T_{end,op}, T_{end,est,op}) \tag{8.12}$$

$$c_{34,op} = \text{lte}(T_{r,op}, T_{r,est,op}) \tag{8.13}$$

where $T_{slt,op}$, $T_{end,op}$, and $T_{r,op}$ are the calculated temperatures at each operating point.

Since the higher estimated temperature leads to larger winding resistance and smaller residual flux density, the optimization algorithm will converge the estimated temperature to the calculated temperature. In this case, the estimated PMSM lumped parameters are the PMSM lumped parameters at steady state temperature.

Another constraint is added to limit the maximum winding temperature

$$c_{35} = \text{lte}(T_{w,pk}, T_{pk,lim}) \tag{8.14}$$

where $T_{w,pk}$ is the winding peak temperature at full load calculated from TEC, and $T_{pk,lim}$ is the maximum allowed winding temperature. With the new constraint, the constraint $c_{17}$ in Section 6.2 that limits the PMSM current density is removed.

The last constraint is to ensure the iterative method introduced in [35] converges

$$c_{36,op} = c_{TEC} \tag{8.15}$$

where $c_{TEC}$ is 1 if the method converges, and 0 if it does not.

The modified pseudo code for the system design paradigm is introduced in Table 8.5. In Table 8.5, the bolded procedures are the modified procedures compared to the pseudo code introduced in Table 6.2 which does not have a thermal model. In Step 1, the no load PMSM magnetic fields are analyzed at room temperature to insure the PMSM is not saturated. The $T_w$ and $T_r$ in (8.8)-(8.10) are set as room temperature for this analysis. In Step 3, the $T_w$ and $T_r$ in (8.8)-(8.10) are substituted with $T_{slt,est,op}$, $T_{end,est,op}$, and $T_{r,est,op}$ of the operating point $n_{op}$ to calculate the PMSM lumped parameters. The PMSM steady state current is determined based on the estimated lumped parameters. Then the iterative method introduced in [35] is applied to calculate the PMSM steady state temperature based on the PMSM steady state current. The constraints $c_{32,op} - c_{34,op}$ are evaluated to insure the estimated temperatures are higher than the calculated temperatures so the optimization algorithm will converge the estimated temperature to the calculated temperature. The constraints $c_{12,op} - c_{16,op}$ are evaluated to insure the PMSM is not saturated at operating point $n_{op}$.

Table 8.5 Modified Pseudo Code for Evaluating Fitness Function

1. Initialize constraint count to $N_C = 20 + 21N_{op}$.

   Assign PMSM material properties (Section 4.1.3). Calculate machine geometry (Section 4.1.1), cogging torque peak value (Section 4.1.9), winding parameters (Section 4.1.2), and PMSM mass $M_G$. Evaluate constraints $c_1 - c_8$, $c_{10}$, and $c_{11}$. Test constraints (Table 6.1).

   **Calculate lumped parameter model (Section 4.1.5) at room temperature. Evaluate constraint $c_{9,op}$. Perform PMSM magnetic field analysis at no current condition (Section 4.1.4 and 4.1.6). Evaluate constraints $c_{12,op}$ - $c_{16,op}$. Test constraints (Table 6.1).**

   Perform output capacitor modeling based on $v_{out}$ (Section 3.2 and Section 3.3).
2. Set $n_{op} = 1$
3. While $n_{op} < N_{op}$
   i. **Calculate lumped parameter model based on the estimated temperatures for operating point $n_{op}$. Evaluate constraint $c_{9,op}$.**
   ii. Perform system steady state analysis (Section 5.1). Calculate $P_{Lin}$, $P_{Lout}$, $P_{t,cd}$, $P_{t,sw}$, and $P_d$. Evaluate constraints $c_{18,op}$ and $c_{19,op}$. Test constraints (Table 6.1).
   iii. **Perform the iterative method introduced in [35] to find the PMSM steady state temperature and magnetic field distribution. Calculate PMSM core loss. Calculate PMSM resistive loss with estimated stator resistance. Evaluate constraints $c_{9,op}$, $c_{12,op}$ - $c_{16,op}$, $c_{32,op}$ - $c_{34,op}$, and $c_{36,op}$. Test constraints (Table 6.1).**
   iv. Perform input capacitor modeling based on $\bar{v}_r$ at full load operating point (Section 3.2). Calculate the input filter ripple (Section 4.3). Calculate $P_{rec}$. Evaluate constraints $c_{20,op} - c_{25,op}$. Test constraints (Table 6.1).
   v. Calculate capacitor RMS current (Section 5.1.4) and temperature rise (Section 3.2). Evaluate constraints $c_{26,op}$ - $c_{28,op}$. Test constraints (Table 6.1). Calculate $P_{op}$.
   vi. $n_{op} = n_{op} + 1$
4. Calculate $P_a$. Evaluate constraint $c_{35}$. Calculate $M_{Lin}$ and $M_{Lout}$ based on full load operating point current (Section 3.1.6). Calculate $M_H$ based on full load operating point semiconductor loss (Section 2.5). Evaluate constraint $c_{29}$. Test constraints (Table 6.1).
5. Perform the stability analysis and disturbance rejection analysis (Section 5.3). Evaluate constraints $c_{30}$ and $c_{31}$. Test constraints (Table 6.1).
6. Compute fitness function and return.

## 8.3 Case Study

The SiC based case study with a disturbance rejection requirement introduced in Section 6.5 is revisited herein to include the PMSM thermal model. The design space is modified to include the estimated temperatures which is shown in Table 8.6. The system specifications presented in Section 6.3 and Section 6.5 are retained. The design fitness function is evaluated according to the Table 8.5. The genetic algorithm population size and number of iterations are both set as 3000.The peak winding temperature limit $T_{pk,lim}$ is set as $180\,°C$ .

Table 8.6 Expanded Design Space

| Gene | Parameter | Min. | Max. | Encoding | Units |
|---|---|---|---|---|---|
| 1 | $P_P$ | 2 | 7 | Int | N/A |
| 2 | $r_{st}$ | 1.4 | 36.25 | Log | cm |
| 3 | $d_{rb}$ | 0.1 | 15 | Log | cm |
| 4 | $d_m$ | 0.1 | 5 | Log | cm |
| 5 | $g$ | 1 | 2.5 | Lin | mm |
| 6 | $d_{tb}$ | 0.1 | 5 | Log | cm |
| 7 | $\alpha_t$ | 0.1 | 0.9 | Lin | N/A |
| 8 | $d_{sb}^*$ | 0.1 | 5 | Log | cm |
| 9 | $\alpha_{pm}$ | 0.1 | 0.9 | Lin | N/A |
| 10 | $B_r^*$ | 0.5 | 1.3 | Lin | T |
| 11 | $l$ | 1 | 20 | Lin | cm |
| 12 | $N_{s1}^*$ | 1 | $1.0 \cdot 10^4$ | Log | cond/rad |
| 13 | $f_{sw}$ | $1.0 \cdot 10^3$ | $1.0 \cdot 10^6$ | Log | Hz |
| 14 | $L_{in}$ | $1.0 \cdot 10^{-6}$ | $1.0 \cdot 10^{-1}$ | Log | H |
| 15 | $J_{Lin}$ | $7.5 \cdot 10^4$ | $7.5 \cdot 10^6$ | Log | $A/m^2$ |
| 16 | $L_{out}$ | $1.0 \cdot 10^{-6}$ | $1.0 \cdot 10^{-1}$ | Log | H |
| 17 | $J_{Lout}$ | $7.5 \cdot 10^4$ | $7.5 \cdot 10^6$ | Log | $A/m^2$ |
| 18 | $C_{in}$ | $1.0 \cdot 10^{-6}$ | $1.0 \cdot 10^{-2}$ | Log | F |
| 19 | $C_{outp}$ | $1.0 \cdot 10^{-6}$ | $1.0 \cdot 10^{-2}$ | Log | F |
| 20 | $C_{oute}$ | $1.0 \cdot 10^{-6}$ | $1.0 \cdot 10^{-2}$ | Log | F |
| 21 | $T_{slt,est}$ | 20 | 180 | Lin | $°C$ |
| 22 | $T_{end,est}$ | 20 | 180 | Lin | $°C$ |
| 23 | $T_{r,est}$ | 20 | 340 | Lin | $°C$ |

The gene distribution of the revisited case study is shown in Fig. 8.2. The first 20 genes follow the same trend as the case study conducted in Section 6.5. The gene 21 to gene 23 are the estimated $T_{slt}$, estimated $T_{end}$, and estimated $T_r$, respectively. It is noted that as the mass decreases, the PMSM estimated temperatures increase which is expected since higher power loss is produced as mass decrease.

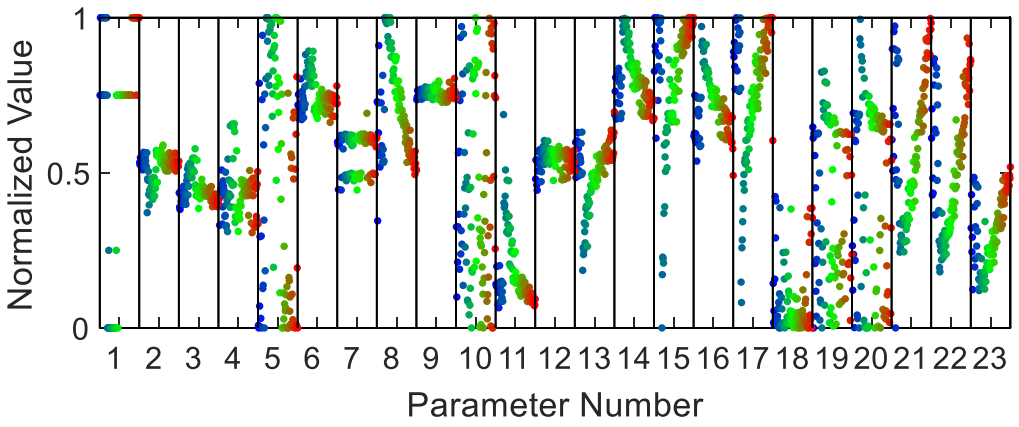


Fig. 8.2 Gene Distribution of the Revisited 'SiC w DR' Case Study

To validate the estimated temperatures are consistent with the TEC predicted temperatures, the temperature error is calculated as

$$T_{n,error} = \frac{T_{n,est} - T_n}{T_n} \tag{8.16}$$

where *n* can be '*slt*', '*end*', or '*r*'. The temperature error of slot winding, end wingding, and rotor are given in Fig. 8.3 – Fig. 8.5, respectively. It is noticed that most designs have a temperature error less than 2% for slot winding, end winding, and rotor. The designs that have large temperature errors could be due to the optimization convergence issue. Increasing the optimization generations should reduce the temperature error further.

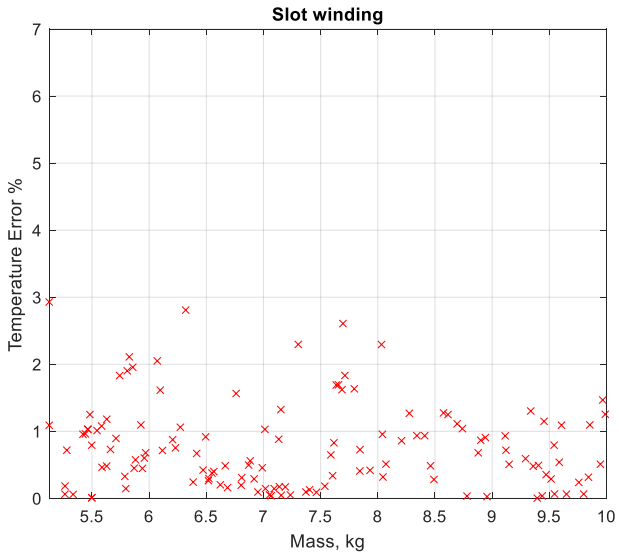


Fig. 8.3 Temperature Error of Slot Winding

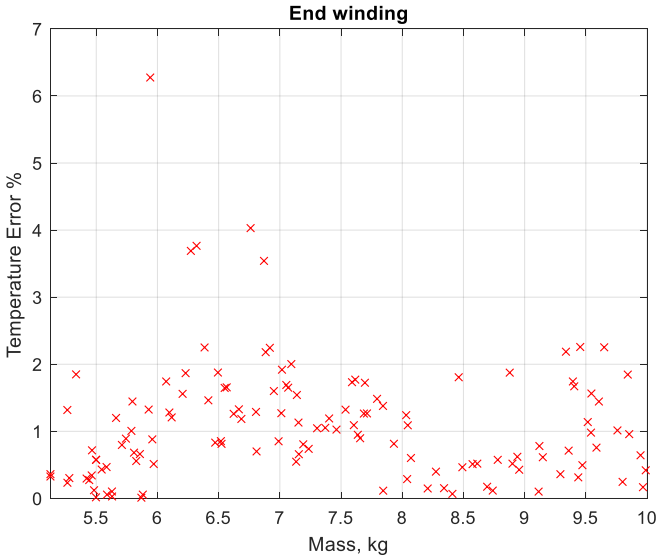


Fig. 8.4 Temperature Error of End Winding

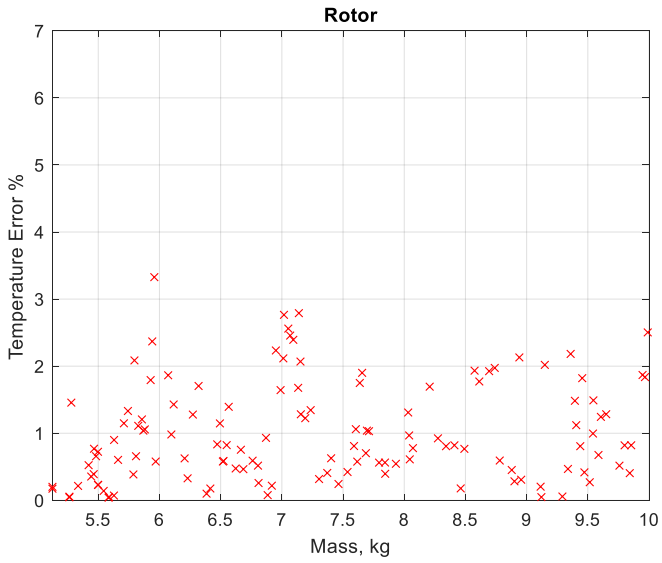


Fig. 8.5 Temperature Error of Rotor

In Fig. 8.6, 'SiC w DR (w TEC)' denotes the revisited case study pareto-optimal front, and 'SiC w DR (wo TEC)' denotes the pareto-optimal front from Section 6.5. By comparing the two pareto-optimal fronts, it is observed that the 'SiC w DR (w TEC)' designs are dominated by the 'SiC w DR (wo TEC)' designs, especially at the low mass region. However, the 'SiC w DR (w TEC)' designs are better than the 'SiC w DR (wo TEC)' designs since the 'SiC w DR (w TEC)' designs include thermal performance. The PMSM current density comparison between the two case studies is shown in Fig. 8.7. The PMSM current density of the revisited case study designs is limited at 7 A/mm$^2$ which is smaller than the current density limit used in the case study from Section 6.5 (7.5 A/mm$^2$).

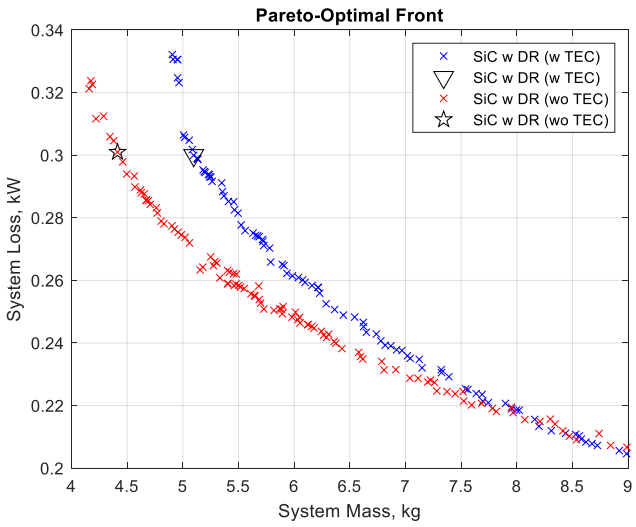


Fig. 8.6 Pareto Optimal Fronts Comparison between Studies with and without PMSM TEC

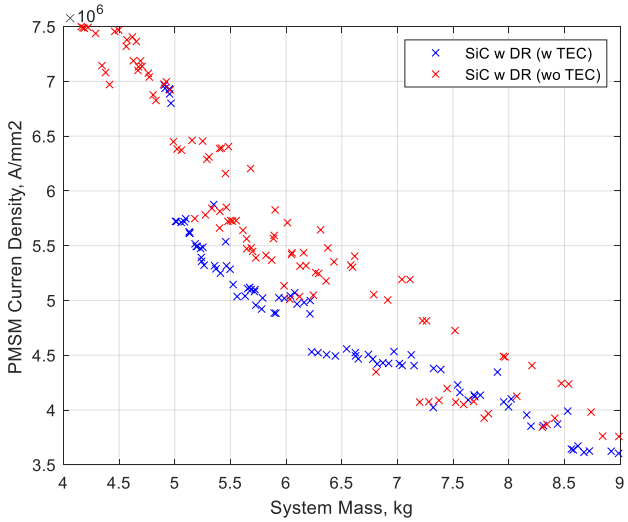


Fig. 8.7 PMSM Current Density Comparison between Studies with and without PMSM TEC

Two example designs are selected from Fig. 8.6 for investigation. Design ‘SiC w DR (w TEC)’ and design ‘SiC w DR (wo TEC)’ are selected from two pareto optimal fronts, respectively. The design parameters of the two designs are listed in Table 8.7. The system loss of the two designs are close to 300W. The system mass of design ‘SiC w DR (w TEC)’ is 14.4% higher than the system mass of design ‘SiC w DR (wo TEC)’. The substantial mass increasement comes from the

PMSM mass. The PMSM mass of design ‘SiC w DR (w TEC)’ is 16.5% higher than the PMSM mass of design ‘SiC w DR (wo TEC)’. The components of the PMSM mass are listed in Table 8.7 for both designs. The conductor mass of the design ‘SiC w DR (w TEC)’ is 42% higher than the design ‘SiC w DR (wo TEC)’ which is expected since the design ‘SiC w DR (w TEC)’ current density is much lower than the design ‘SiC w DR (wo TEC)’. The stator steel mass of the design ‘SiC w DR (w TEC)’ is 15.7% higher than the design ‘SiC w DR (wo TEC)’ since a larger stator is required to hold larger windings. The rotor steel mass of the design ‘SiC w DR (w TEC)’ is 7.6% higher than the design ‘SiC w DR (wo TEC)’. The permanent magnet mass of the design ‘SiC w DR (w TEC)’ is 30% lower than the design ‘SiC w DR (wo TEC)’ which is caused by the smaller active length. The permanent magnet mass drop of the design with thermal model is interesting since the magnet material cost tends to be the highest among the machine construction materials. Another interesting point is that the PMSM that considers thermal model has a larger radius, smaller active length, and smaller air gap compared to the PMSM that doesn’t consider thermal performance which makes it more optimal from the torque density perspective.

Table 8.7 Example Designs

| Parameter | SiC w/o DR (w TEC) | SiC w DR (wo TEC) |
|---|---|---|
| $M$ (kg) | 5.10 | 4.46 |
| $P$ (W) | 299.9 | 300.9 |
| $M_C$ (kg) | 0.8101 | 0.7796 |
| $P_C$ (W) | 81.68 | 82.75 |
| $M_G$ (kg) | 4.288 | 3.681 |
| $P_G$ (W) | 218.3 | 218.2 |
| $P_p$ | 7 | 7 |
| $r_{st}$ (cm) | 8.317 | 6.662 |
| $d_{rb}$ (mm) | 8.326 | 5.613 |
| $d_m$ (mm) | 3.404 | 3.515 |
| $g$ (mm) | 1.251 | 2.241 |
| $d_{tb}$ (mm) | 16.49 | 11.46 |
| $\alpha_t$ | 59.28% | 50.06% |
| $d_{sb}$ (mm) | 8.283 | 5.41 |
| $\alpha_{pm}$ | 72.5% | 73.13% |
| $B_r$ (T) | 1.142 | 1.233 |
| $l$ (cm) | 2.593 | 4.576 |
| $N_{s1}$ | 134.4 | 106.3 |
| $f_{sw}$ (kHz) | 63.776 | 67.799 |
| $L_{in}$ (mH) | 3.14 | 2.94 |
| $J_{Lin}$ (A/mm$^2$) | 7.46 | 7.5 |
| $L_{out}$ (mH) | 1.309 | 1.173 |
| $J_{Lout}$ (A/mm$^2$) | 7.42 | 7.5 |
| $C_{in}$ (μF) | 2 | 2 |
| $C_{outp}$ ( μF) | 15 | 4 |
| $C_{oute}$ ( μF) | 159.9 | 170.5 |

Table 8.8 Example Designs PMSM Mass Comparison

| Component | SiC w DR (w TEC) | SiC w DR (wo TEC) |
|---|---|---|
| Stator steel mass | 1.903 kg | 1.645 kg |
| Rotor steel mass | 0.705 kg | 0.655 kg |
| Conductor mass | 1.412 kg | 0.997 kg |
| Magnet mass | 0.268 kg | 0.384 kg |
| PMSM mass | 4.288 kg | 3.681 kg |

In this chapter, the PMSM thermal model is included in the system design paradigm. The system power density is greatly impact by the inclusion of the thermal model. In the next chapter, the summary of this work is introduced, along with the suggestions for future work.

# 9. SUMMARY AND FUTURE WORK

In this work, a methodology to design a dc generation system is set forth. The generator and the converter are designed simultaneously to achieve an optimal system design. In order to do this, various system component models are developed. Among the different component models, the PMSM model is of particular interest since the model considers the temporal current harmonics and spatial winding harmonics which greatly increases the PMSM model's fidelity. The system steady state analysis, stability analysis, and disturbance rejection analysis are performed. The disturbance rejection analysis is evaluated in frequency domain instead of time domain to accommodate to the optimization based design methodology. To demonstrate the design methodology, a case study is conducted and the results are presented. The SiC semiconductor based case study is compared to the Si semiconductor based case study to quantify the advantage of WBG device as it is a promising solution to improve the power density and efficiency. To validate the proposed design paradigm, a SiC based generation system is constructed. The system steady state measurements match well with the design model prediction. In the last part of the dissertation, a TEC based PMSM thermal model is included in the design paradigm. To help the optimization convergence, extra design variables are added to estimate the PMSM temperature in slot winding, end winding, and rotor. The updated case study shows that including PMSM thermal performance has a large impact to the system power density.

The design methodology is explained thoroughly in this dissertation. However, there is more work to be carried out in the future. It would be appropriate to include the PMI ac losses into the PMI metamodel to have a better system loss prediction. A constant power load should be considered in the future instead of the resistive load applied in the dissertation. For hardware validation, it is desirable to test the prototype system at the rated operating point. The prototype

system’s disturbance rejection capability should also be tested in the future. Last but not least, it is interesting to apply the design paradigm to other dc generation system topologies such as an active rectifier based dc generation system.

# APPENDIX A. PMSM MATERIAL PROPERTIES

Table A.1 JFE 10JNEX900 Material Properties

| Parameter | Value | Comment |
|---|---|---|
| $\rho$ | 6989 kg/m$^3$ | Mass density |
| $B_{lim}$ | 1.21 T | Recommended limit on B to avoid saturation |
| $\mu_r$ | 24550.5347 | Relative permeability |
| $\alpha_\mu$ | [0.19621 1.0684·10$^{-2}$ 1.3418·10$^{-3}$ 1·10$^{-3}$] 1/T | Permeability function parameter |
| $\beta_\mu$ | [12.0278 51.069 0.769722 6.40075] 1/T | Permeability function parameter |
| $\gamma_\mu$ | [1.6159 1.1483 5.3435 1.1299] T | Permeability function parameter |
| $\alpha$ | [2.4866 1 1.4614] | Modified Steinmetz Equation Parameter |
| $\beta$ | [5 1.7064 1.6173] | Modified Steinmetz Equation Parameter |
| $k_h$ | [1·10$^{-4}$ 94.8487 1.93165] J/m$^3$ | Modified Steinmetz Equation Parameter |
| $k_e$ | 2.3658·10$^{-3}$ Js/m$^3$ | Modified Steinmetz Equation Parameter |

Table A.2 Copper Material Properties

| Parameter | Value | Comment |
|---|---|---|
| $\rho$ | 8890 kg/m$^3$ | Mass density |
| $\sigma_0$ | $5.959 \cdot 10^{-7}$ S/m | Conductivity |
| $\alpha_T$ | $3.93 \cdot 10^{-3}$ K$^{-1}$ | Temperature coefficients of resistivity |
| $T_0$ | $20\,°C$ | Nominal temperature where conductivity is characterized |

Table A.3 PMSM Permanent Magnet Catalog

| Base | Material | $B_r$ (T) | $H_{cb}$ (kA/m) | $H_{cj}$ (kA/m) | $T_C$ ($°C$) | $\rho$ (kg/m$^3$) | $\chi$ | $\alpha_B$ (K$^{-1}$) | $\alpha_H$ (K$^{-1}$) |
|---|---|---|---|---|---|---|---|---|---|
| SmCo5 | R22 | 0.94 | -730 | -2400 | 250 | 8.4 | 0.0247 | 0.00045 | 0.00025 |
| SmCo5 | R25 | 1 | -775 | -2400 | 250 | 8.4 | 0.0268 | 0.0005 | 0.0024 |
| Sm2Co17 | R24HE | 1.02 | -765 | -2000 | 350 | 8.4 | 0.0611 | 0.00035 | 0.00212 |
| Sm2Co17 | R26 | 1.04 | -765 | -2000 | 350 | 8.3 | 0.0819 | 0.00035 | 0.00247 |
| Sm2Co17 | R26HE | 1.07 | -800 | -2000 | 350 | 8.4 | 0.0644 | 0.00035 | 0.0024 |
| Sm2Co17 | R28 | 1.1 | -800 | -2000 | 350 | 8.3 | 0.0942 | 0.00035 | 0.0024 |
| Sm2Co17 | R30 | 1.12 | -820 | -1600 | 250 | 8.3 | 0.0869 | 0.00035 | 0.0025 |
| Sm2Co17 | R30S | 1.12 | -845 | -2150 | 350 | 8.3 | 0.0548 | 0.00035 | 0.0025 |
| Sm2Co17 | R32 | 1.15 | -835 | -1350 | 250 | 8.3 | 0.0960 | 0.00035 | 0.0025 |
| Sm2Co17 | R33E | 1.16 | -867 | -2100 | 350 | 8.3 | 0.0647 | 0.00035 | 0.0025 |
| Sm2Co17 | R33E | 1.17 | -860 | -2100 | 350 | 8.3 | 0.0862 | 0.00035 | 0.0025 |

# REFERENCES


1. G. Sulligoi, A. Tessarolo, V. Benucci, A. M. Trapani, M. Baret and F. Luise, "Design, implementation and testing of a shipboard medium-voltage DC generation system based on a ultra-high speed 12-phase alternator," *2011 IEEE Electric Ship Technologies Symposium*, Alexandria, VA, 2011, pp. 388-395.

2. N. Amiri, S. Ebrahimi, Y. Huang, J. Jatskevich and H. W. Dommel, "Saturable voltage-behind-reactance model of six-phase synchronous machine in hybrid AC and DC generation system," *2016 IEEE Canadian Conference on Electrical and Computer Engineering (CCECE)*, Vancouver, BC, 2016, pp. 1-4.

3. Y. Jia and K. Rajashekara, "An Induction Generator-Based AC/DC Hybrid Electric Power Generation System for More Electric Aircraft," in *IEEE Transactions on Industry Applications*, vol. 53, no. 3, pp. 2485-2494, May-June 2017.

4. G. D. Wang, R. J. Wai and Y. Liao, "Design of backstepping power control for grid-side converter of voltage source converter-based high-voltage dc wind power generation system," in *IET Renewable Power Generation*, vol. 7, no. 2, pp. 118-133, March 2013.

5. O. Laldin, S. D. Sudhoff and S. Pekarek, "Analysis and Design of Hybrid Machines for DC Generation," in *IEEE Transactions on Energy Conversion*, vol. 30, no. 3, pp. 1192-1199, Sept. 2015.

6. C. Sourkounis, A. Broy and B. Ni, "Influence of dc-link converter on operational performance of the power conversion train of wind energy converters with PMSM," *7th Mediterranean Conference and Exhibition on Power Generation, Transmission, Distribution and Energy Conversion (MedPower 2010)*, Agia Napa, 2010, pp. 1-7.

7. G. M. Shane, "Permanent magnet inductor design for reduced mass inductive components, " Ph.D., Purdue University, United States-Indiana, 2012.

8. A. Nasr, S. Hlioui, M. Gabsi, M. Mairie and D. Lalevee, "Design Optimization of a Hybrid-Excited Flux-Switching Machine for Aircraft safe DC Power Generation using a Diode Bridge Rectifier," in *IEEE Transactions on Industrial Electronics*, vol. PP, no. 99, pp. 1-1.

9. P. R. O'Regan, R. Wang and S. D. Pekarek, "Design of synchronous machines for DC power generation," *2015 IEEE International Electric Machines & Drives Conference (IEMDC)*, Coeur d'Alene, ID, 2015, pp. 1665-1670.

10. V. Arcidiacono, A. Monti and G. Sulligoi, "An innovative generation control system for improving design and stability of shipboard medium-voltage DC Integrated Power System," *2009 IEEE Electric Ship Technologies Symposium*, Baltimore, MD, 2009, pp. 152-156.

11. D. Dong, Y. Pan, R. Lai, X. Wu and K. Weeber, "Active Fault-Current Foldback Control in Thyristor Rectifier for DC Shipboard Electrical System," in *IEEE Journal of Emerging and Selected Topics in Power Electronics*, vol. 5, no. 1, pp. 203-212, March 2017.

12. C. Vlachos, D. Williams and J. B. Gomm, "Genetic approach to decentralised PI controller tuning for multivariable processes," in *IEE Proceedings - Control Theory and Applications*, vol. 146, no. 1, pp. 58-64, Jan 1999.

13. S. Lee, "Optimal decentralised design for output-feedback power system stabilisers," in *IEE Proceedings - Generation, Transmission and Distribution*, vol. 152, no. 4, pp. 449-459, 8 July 2005.

14. A. A. S. Mohamed, A. Berzoy and O. A. Mohammed, "Design and Hardware Implementation of FL-MPPT Control of PV Systems Based on GA and Small-Signal Analysis," in *IEEE Transactions on Sustainable Energy*, vol. 8, no. 1, pp. 279-290, Jan. 2017.

15. H. Suryanarayana, " Design paradigm for power electronics based DC distribution systems, " Ph.D., Purdue University, United States-Indiana, 2016.

16. F. Wang, Z. Zhang, T. Ericsen, R. Raju, R. Burgos and D. Boroyevich, "Advances in Power Conversion and Drives for Shipboard Systems," in Proceedings of the IEEE, vol. 103, no. 12, pp. 2285-2311, Dec. 2015.

17. L. Wang, Q. Zhu, W. Yu and A. Q. Huang, "A Medium-Voltage Medium-Frequency Isolated DC–DC Converter Based on 15-kV SiC MOSFETs," in *IEEE Journal of Emerging and Selected Topics in Power Electronics*, vol. 5, no. 1, pp. 100-109, March 2017.

18. S. Guo, P. Liu, R. Yu, L. Zhang and A. Q. Huang, "Analysis and loss comparison of megahertz high voltage isolated DC/DC converters utilizing integrated SiC MOSFET module," *2016 IEEE 4th Workshop on Wide Bandgap Power Devices and Applications (WiPDA)*, Fayetteville, AR, 2016, pp. 291-296.

19. P. Ning, F. (. Wang and K. D. T. Ngo, "Forced-Air Cooling System Design Under Weight Constraint for High-Temperature SiC Converter," in *IEEE Transactions on Power Electronics*, vol. 29, no. 4, pp. 1998-2007, April 2014.

20. R. J. Kaplar, J. C. Neely, D. L. Huber and L. J. Rashkin, "Generation-After-Next Power Electronics: Ultrawide-bandgap devices, high-temperature packaging, and magnetic nanocomposite materials," in *IEEE Power Electronics Magazine*, vol. 4, no. 1, pp. 36-42, March 2017.

21. M. Schupbach. (2008, Sept.). High power density silicon carbide power electronic converters. [Online]. Available: http://www.sandia.gov/ess/docs/pr_conferences/2008/schupbach_apei.pdf.

22. R. Nune, A. Anurag, S. Anand and Y. S. Chauhan, "Comparative analysis of power density in Si MOSFET and GaN HEMT based flyback converters," *2016 10th International Conference on Compatibility, Power Electronics and Power Engineering (CPE-POWERENG)*, Bydgoszcz, 2016, pp. 347-352.

23. N.Mohan, T.M.Undeland, and W.P.Robbins, "Power Electronics: Converters, Applications and Design", 3rd ed. New York, NY, USA: Wiley, 2002.

24. S. D. Sudhoff, "Waveform reconstruction from the average-value model of line-commutated converter-synchronous machine systems," in *IEEE Transactions on Energy Conversion*, vol. 8, no. 3, pp. 404-410, Sep 1993.

25. Micorsemi, Inc, "APT13GP120B Power MOS 7 IGBT Datasheet." Available: microsemi.com.

26. Powerex Power Semiconductor Solutions. "CS241250 Datasheet." Availabel: pwrx.com.

27. Cree, Inc, "C2M0080120D Datasheet." Available: cree.com/power.

28. Cree, Inc, "C4D20120A Datasheet." Available: cree.com/power.

29. S. D. Sudhoff, G. M. Shane, and H. Suryanarayana, "Magnetic-equivalent-circuit-based scaling laws for low-frequency magnetic devices," *IEEE Trans. Energy Convers*., vol. 28, no. 3, pp. 746–755, Sep. 2013.

30. Magnetic Equivalent Circuit Toolbox 3.2, School of Electrical and Computer Engineering, Purdue University, West Lafayette, IN, [Online]. Available:https://engineering.purdue.edu/ECE/Research/Areas/PEDS/ MEC_toolbox.

31. S. D. Sudhoff, "Power Magnetic Devices: A Multiobjective Design Approach", IEEE Press/Wiley, 2014.

32. Genetic Optimization System Engineering Tool (GOSET) For Use with MATLAB, Manual Version 2.6, School of Electrical and Computer Engineering, Purdue University, West Lafayette, IN, with United States Naval Academy, Annapolis, MD, 2014. Available:https://engineering.purdue.edu/ECE/Research/Areas/PEDS/go_system_engineering_toolbox.

33. Vishay Intertechnology, Inc, "MKP1848C DC-Link Datasheet." Available: vishay.com.

34. United Chemi-Con, Inc, "U91/U92 Series High Ripple Snap Mount Capacitors." Available: chemi-con.com.

35. A. Kasha, "Multi-Objective Design Optimization of A Surface-Mounted Heterogeneous-Pole Permanent-Magnet Machine," Ph.D., Purdue University, United States-Indiana, 2016.

36. J. Alsawalhi, "An Asymmetric Salient Permanent Magnet Synchronous Machine for Wide Constant Power Speed Range Applications," Ph.D., Purdue University, United States-Indiana, 2014.

37. S. D. Sudhoff and R. Sahu, "Metamodeling of Rotating Electric Machinery," in *IEEE Transactions on Energy Conversion*, vol. PP, no. 99, pp. 1-1.

38. H. Dhulipati, S. Mukundan, K. L. V. Iyer and N. C. Kar, "Skewing of stator windings for reduction of spatial harmonics in concentrated wound PMSM," *2017 IEEE 30th Canadian Conference on Electrical and Computer Engineering (CCECE)*, Windsor, ON, 2017, pp. 1-4.

39. G. Choi and T. Jahns, "Analysis and Design Recommendations to Mitigate Demagnetization Vulnerability in Surface PM Synchronous Machines," in *IEEE Transactions on Industry Applications*, vol. PP, no. 99, pp. 1-1.

40. P. C. Krause; O. Wasynczuk; S. D. Sudhoff; S. Pekarek, "Distributed Windings in ac Machinery," in *Analysis of Electric Machinery and Drive Systems* , 1, Wiley-IEEE Press, 2013.

41. P. C. Krause; O. Wasynczuk; S. D. Sudhoff; S. Pekarek, "Reference-Frame Theory," in *Analysis of Electric Machinery and Drive Systems* , 1, Wiley-IEEE Press, 2013.

42. "User's Guide - Maxwell 2D," ANSYS Maxwell, Mar 2012, rev. 6. [Online].Available: http://ansoft-maxwell.narod.ru/en/CompleteMaxwell2D_V15.pdf.

43. G. M. Shane and S. D. Sudhoff, "Refinements in Anhysteretic Characterization and Permeability Modeling," IEEE Transactions on Magnetics, vol. 46, no. 11, pp. 3834-3843, Nov. 2010.

44. Li Zhu, S. Z. Jiang, Z. Q. Zhu and C. C. Chan, "Comparison of alternate analytical models for predicting cogging torque in surface-mounted permanent magnet machines," *2008 IEEE Vehicle Power and Propulsion Conference*, Harbin, 2008, pp. 1-6.

45. P. C. Krause; O. Wasynczuk; S. D. Sudhoff; S. Pekarek, " Semi-Controlled Bridge Converters," in *Analysis of Electric Machinery and Drive Systems* , 1, Wiley-IEEE Press, 2013.

46. Cree, Inc, "CRD-001 Datasheet." Available: cree.com/power.

# VITA

Bo Zhang received his B.S from Shanghai University in 2013, and his PhD degree from Purdue University in 2019. His interest include electric machine design and fabrication, and power electronics.